Chem Soc Rev

REVIEW ARTICLE

View Article Online
View Journal

Cite this: DOI: 10.1039/d4cs00328d

Colorimetric sensing for translational applications: from colorants to mechanisms

Zhicheng Jin, †[a] Wonjun Yim, †‡[b] Maurice Retout, [a] Emily Housel, [a] Wenbin Zhong, [c] Jiajing Zhou, [a] Michael S. Strano [d] and Jesse V. Jokerst *[abe]

Colorimetric sensing offers instant reporting *via* visible signals. *Versus* labor-intensive and instrument-dependent detection methods, colorimetric sensors present advantages including short acquisition time, high throughput screening, low cost, portability, and a user-friendly approach. These advantages have driven substantial growth in colorimetric sensors, particularly in point-of-care (POC) diagnostics. Rapid progress in nanotechnology, materials science, microfluidics technology, biomarker discovery, digital technology, and signal pattern analysis has led to a variety of colorimetric reagents and detection mechanisms, which are fundamental to advance colorimetric sensing applications. This review first summarizes the basic components (*e.g.*, color reagents, recognition interactions, and sampling procedures) in the design of a colorimetric sensing system. It then presents the rationale design and typical examples of POC devices, *e.g.*, lateral flow devices, microfluidic paper-based analytical devices, and wearable sensing devices. Two highlighted colorimetric formats are discussed: combinational and activatable systems based on the sensor-array and lock-and-key mechanisms, respectively. Case discussions in colorimetric assays are organized by the analyte identities. Finally, the review presents challenges and perspectives for the design and development of colorimetric detection schemes as well as applications. The goal of this review is to provide a foundational resource for developing colorimetric systems and underscoring the colorants and mechanisms that facilitate the continuing evolution of POC sensors.

Received 9th April 2024

DOI: 10.1039/d4cs00328d

rsc.li/chem-soc-rev

1. Introduction

Colorimetric sensors are a type of perceivable signal transduction sensing platform, enabling visual measurement.[1–3] They have been crucial diagnostic tools for centuries: the color change in urine, eyes, skin, and blood can all indicate various diseases including urinary tract infections, glucose levels, jaundice, vitiligo, melanoma, rosacea, and sickle cell anemia. Such traditional colorimetric diagnosis methods are limited by their sensitivity and specificity and are vulnerable to subjective interpretations. This has led to amazing advances in laboratory-based analysis as well as the emergence of advanced colorimetric detection techniques. Advanced colorimetry measures an analyte either qualitatively or quantitatively through using colorimetric reagents. The typical design includes a recognition element for selective interactions with target analytes and a transducer for reporting the interaction.[4] This design can be also rationally integrated into compact and durable systems with an intuitive user interface, *e.g.*, a point-of-care (POC) device for automatic sample preparation and readout control, thus eliminating the need for specialized technical training.[5] Modern colorimetric detection methods are rapid, sensitive, portable, and affordable, thus making the sensing process available for various scenarios including clinical laboratories,[6] industrial environments,[7] agricultural areas,[8] residential spaces,[9] and public transit systems.[10]

The substantial growth in the colorimetric sensors is partially mirrored in the global biosensors market, which is expected to achieve a 7.5% compound annual growth rate from 2021–2026 reaching 3.2 billion USD by 2026.[11] This growth is propelled by several factors such as the rise of nanotechnology-based biosensors, their increasing use in diabetes monitoring, the demand for home-based devices due to SARS-CoV-2 and hepatitis C virus, and governmental initiatives towards POC diagnostics, which collectively reduce the pressure in public

[a] Aiiso Yufeng Li Family Department of Chemical and Nano Engineering, University of California, San Diego, La Jolla, CA 92093, USA. E-mail: jjokerst@ucsd.edu
[b] Materials Science and Engineering Program, University of California, San Diego, La Jolla, CA 92093, USA
[c] School of Chemistry, Chemical Engineering and Biotechnology, Nanyang Technological University, 21 Nanyang Link, Singapore 637371, Singapore
[d] Department of Chemical Engineering, Massachusetts Institute of Technology, Cambridge, MA 02139, USA
[e] Department of Radiology, University of California, San Diego, La Jolla, CA 92093, USA
† These authors contributed equally.
‡ Present address: Department of Chemical Engineering, Massachusetts Institute of Technology, Cambridge, MA 02139, USA.

healthcare facilities.[11] For instance, the widely employed pregnancy strip utilizes colorimetric assays to detect the presence of human chorionic gonadotropin (hCG) in urine at home, and the COVID-19 antigen rapid test strip employs immunochromatographic assays to report SARS-CoV-2 antigens in nasal swab specimens for end-users. Therefore, translational POC colorimetric tests are increasingly important in improving overall quality of life.

The development of colorimetric sensors prioritizes enhancing key aspects such as colorant, signaling mechanism, selectivity, response time, limit of detection, multiplexing, automated signal analysis, and cost-effectiveness.[12] For example, optimizing the colorimetric reagents (*e.g.*, inorganic nanoparticles and organic chromophores) is critical for improving sensing performance. Modifying chromophore structures to increase molar absorption coefficients or incorporate specific binding pockets can improve sensitivity, selectivity, and stability.[13] Moreover, colorants involving inorganic nanoparticles (NPs) with size- and shape-dependent optical properties offer intense color, photobleaching resistance, high sensitivity, easy functionalization, and multiplexing ability, thus enabling rapid and efficient detection of diverse targets.[14,15] The NP-based colorimetric mechanisms could involve immobilization, aggregation,[16] redispersion,[17] etching,[18] formation,[19] and re-shaping growth.[20] Therefore, the large library of colorimetric reagents and diverse signaling mechanisms have generated emerging techniques and commercial colorimetric products. However, a limited number of reviews cover the fundamental aspects of colorimetric sensors, *e.g.*, Suslick *et al.* and Yoon *et al.* focused on dye molecules in colorimetric sensing up until 2019,[13,21] while Rotello *et al.* and Chen *et al.* highlighted the use of gold nanoparticles (AuNPs) as sensing colorants up until 2015.[14,22] Here, we present a comprehensive review focusing on advancements in various colorants and signaling formats within colorimetric sensors. This review also summarizes the role of commercial colorimetric products in shaping sensor evolution, addresses associated challenges, and provides potential solutions for emerging techniques. Our aim is to promote the development of next-generation colorimetric sensors and other *in vitro* diagnostic techniques with translational applications.

Zhicheng Jin

Zhicheng Jin is currently completing his postdoc research in the Jokerst Bioimaging Lab in the Aiiso Yufeng Li Family Department of Chemical and Nano Engineering at UC San Diego. He received his PhD in 2020 from Florida State University under the guidance of Prof. Hedi Mattoussi. His current research interests are the development of functional coacervates and polymers for biosensing and nanomedicine. He has received the 2020 SPIE Ocean Insight Young Investigator Award.

Wonjun Yim

Wonjun Yim completed his PhD in materials science in 2023 at UC San Diego under the supervision of Prof. Jesse V. Jokerst. He then joined Prof. Michael S. Strano's group as a postdoctoral fellow at Massachusetts Institute of Technology. His research focuses on developing novel nanomaterials for biomedical applications. He has received the Thomas Gareth Award 2022 and Schmidt Science Fellow 2024.

Maurice Retout

Maurice Retout completed his PhD in 2020 at the Université libre de Bruxelles in Belgium where he studied the synthesis and functionalization of plasmonic nanomaterials for the design of in vitro sensors. He then joined the Jokerst Bioimaging Lab at UC San Diego, where he explored the use of plasmonic nanoplatforms as contrast agents for photoacoustic imaging. In 2024, he came back to Belgium as an independent investigator in nanomedicine, developing photoacoustic imaging contrast agent for cancer diagnosis.

Jiajing Zhou

Jiajing Zhou is a Professor in the Department of Biomass and Leather Engineering at Sichuan University, China. Dr Zhou completed his PhD in bioengineering in 2016 at Nanyang Technological University, Singapore. From 2018 to 2020, Dr Zhou conducted postdoctoral research under the guidance of Prof. Frank Caruso at the University of Melbourne, and from 2020 to 2022, he continued his postdoctoral studies with Prof. Jesse V. Jokerst at UC San Diego. His current research interests are the development of functional nanohybrids for biomedical applications and 3D printing technologies.

This review will begin with an introduction to fundamental sensor components followed by translational products, signaling mechanisms, and perspectives on colorimetric sensing technology. Section 1 introduces the concept and development of colorimetric sensors. Sections 2 and 3 cover the basic design of a colorimetric system including colorimetric reagents, recognition interactions, and sampling. Section 4 presents POC devices including the rational design and typical example of lateral flow assays (LFA), microfluidic paper-based analytical devices (μPAD), and wearable sensors. In Sections 5 and 6, we categorized the colorimetric format into two systems – combinational and activatable – based on the olfactory-mimetic sensor-array and lock-and-key mechanism, respectively. The discussion is organized based on the analyte identities. In this review, we particularly emphasize the use of plasmonic NPs as colorants and then discuss mechanisms and potential translation in biomedicine. In Sections 7 and 8, we discuss the challenges and future perspectives in the development and clinical translation of colorimetric assays. We focus on perceived color-based detection assays, excluding fluorescence color-based methods and enzyme-linked immunosorbent assays (ELISA). We hope that this review serves as a foundational resource in the field of colorimetric assay development, underscoring the colorants and mechanisms that facilitate the continuing evolution of POC sensors.

2. Colorimetric reagents

At the core of colorimetric sensing lies the selection of colorants based on their chemical and photophysical properties. Colorimetric reagents signal the target analyte or interaction events through naked eye observation. Inorganic nanocrystals such as plasmonic NPs and metallic nanoclusters have emerged as alternative and excellent color agents.[14,15] They offer cost-effective production, high molar absorption coefficients, exceptional sensitivity, and multifunctionality.[22] Organic materials, such as natural pigments, synthetic dyes, and polymers also form a significant portion of traditional colorants.[23–25] These organic materials offer design flexibility, solubility, biocompatibility, and a wide range of colors. The color signal produced in this process exhibits a direct proportionality to the presence or concentration of the analyte, thus enabling both qualitative and quantitative analyses. Here, we will present inorganic, organic, and hybrid colorants and briefly discuss their color-changing mechanisms. Major discussion will be based on using inorganic NPs as color agents. Discussion on detailed applications is provided in Sections 5 and 6.

2.1 Inorganic nanoparticles

Plasmonic nanoparticles serve as exceptional colorants due to their localized surface plasmon resonance (LSPR) band and high molar absorption coefficients. LSPR arises from coherent oscillations of conduction electron when interacting with incident electromagnetic fields.[26,27] When the light frequency matches the collective motion of conduction electron could, these NPs strongly absorb and scatter the incident light and transmit perceivable colors. Tailoring the optical properties can be achieved by adjusting core composition, size, shape, and interparticle spacing, thus yielding a spectrum of vivid visual colors (Fig. 1). For example, close proximity of plasmonic nanoparticles leads to surface plasmon coupling, as the conduction electrons on each particle surface collectively oscillate, causing dramatic visible color changes during aggregation.[16,28] In addition, immobilization (in LFAs), redispersion,[17] etching (or dissolution),[18] formation,[19] and re-shape growth (or Ostwald ripening)[20] induce color changes in NP dispersion that

Michael S. Strano

Michael S. Strano is currently the Carbon P. Dubbs Professor in the Chemical Engineering Department at the Massachusetts Institute of Technology. He received is BS from Polytechnic University in Brooklyn, NY and PhD from the University of Delaware, both in Chemical Engineering. He was a post-doctoral research fellow at Rice University in the departments of Chemistry and Physics under the guidance of Nobel Laureate Richard E. Smalley. His research focuses on biomolecule/nanoparticle interactions and the surface chemistry of low dimensional systems, nano-electronics, nanoparticle separations, and applications of vibrational spectroscopy to nanotechnology. Michael is the recipient of the 2019 Professional Progress Award from the American Institute of Chemical Engineers, and elected to the National Academy of Engineering in 2017.

Jesse V. Jokerst

Jesse V. Jokerst is a Professor in the Aiiso Yufeng Li Family Department of Chemical and Nano Engineering at UC San Diego. Dr Jokerst completed a PhD in Chemistry at the University of Texas at Austin in 2009. Jesse was a postdoc at Stanford Radiology from 2009–2013 and was an instructor in that same department from 2013–2015. Jesse started at UCSD in July of 2015, and he has received the NIH K99/R00 Pathway to Independence Award, the NIH New Innovator Award, the NSF CAREER Award, and Stanford Radiology Alumni of the Year Award.

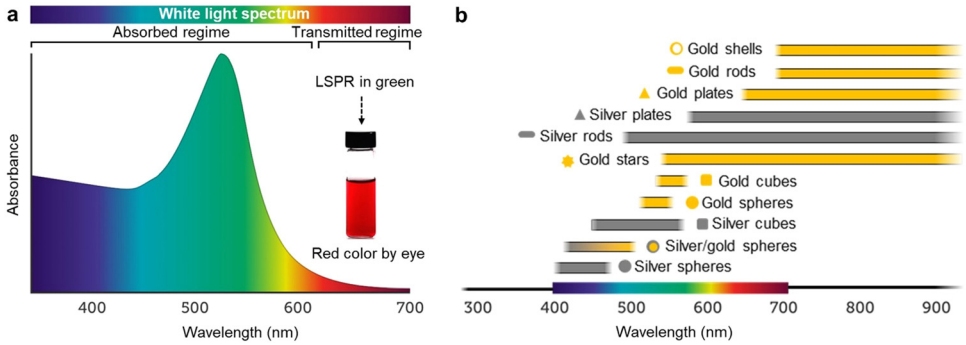

Fig. 1 Absorption properties of gold and silver nanoparticles. (a) The location of the LSPR in the spectrum determines the color. White light interacting with plasmonic AuNPs selectively absorbs blue and green regimes, thus allowing red light to transmit through. The AuNP dispersion appears red to the naked eye. (b) A list of gold and silver NPs with tunable shapes and compositions, together with their typical locations of surface plasmon resonance bands in the visible regime.

can be controlled by the presence or activity of target analytes. These effects are fundamental to various plasmonic sensors. In this subsection, we will present gold, silver, and their hybrid nanocrystals as colorants, along with color changing mechanisms.

2.1.1 Gold nanostructures. AuNPs can be synthesized through several methods, including the water-phase reduction by Turkevich method,[29] the oil-phase hot injection in oleylamine,[30] and the seed-mediated growth with hydroxylamine,[31,32] thus allowing for the production of highly stable NPs of various sizes on a large scale. AuNPs of diameters ranging from 4 to 100 nm exhibit a unique SPR band resulting in a magenta color. They have a high molar absorption coefficient (ε) on the order of nearly 10^8 M^{-1} cm^{-1} resulting in intense coloration (Table 1). These NPs also exhibit strong near-field interactions with nearby dye emitters and Raman-active molecules.[33] The photophysical properties of AuNPs and dispersion color can be readily tuned by varying the size, shape, and the surrounding environment (Fig. 2a–c). Additionally, AuNPs possess a high surface-to-volume ratio and exhibit excellent biocompatibility when appropriately coated. This enables their easy functionalization with various synthetic ligands or biomolecules for selective binding and detection of target analytes.[14] The mechanisms of color change using AuNPs in response to binding interactions often involve direct coloration in LFA (*i.e.*, 40-nm size), dispersity modulation (*i.e.*, aggregation and redispersion), and reduced NP formation.

Anisotropic gold nanorods (AuNRs) are synthesized *via* seeded growth in the presence of a halide-containing cationic surfactant, such as CTAB. This method was initially introduced by Murphy[36,37] and El-Sayed.[38] Achieving biocompatibility for AuNRs requires stepwise surface engineering, *e.g.*, utilizing polystyrene sulfonate (PSS) as an intermediate step to fully remove CTAB before final coating. The stability and functionality of these AuNRs are exceptional after coating with entropic ligands.[39,40] AuNRs exhibit an additional strong longitudinal SPR peak in the NIR region of the optical spectrum with significantly high molar absorption coefficients of approximately 10^9 M^{-1} cm^{-1} (Table 2). The wavelength of this longitudinal SPR peak is tunable over a range of more than 400 nm depending on the aspect ratio.[41] As the aspect ratio increases, the peak shifts towards the infrared spectrum, resulting in a wide array of colors ranging from green and blue to red (Fig. 2b). The strong longitudinal absorption of AuNRs, coupled with the ability of NIR irradiation to penetrate deep into tissues, make these materials suitable for photoacoustic imaging, SERS imaging, and thermal-based therapeutic agents for *in vivo* applications. Nonetheless, a colorimetric assay using plasmonic coupling of AuNR is imperceptible to the naked eye due to spectral shifts in the (near) infrared spectrum. The weak color change also holds true from aggregation of other anisotropic nanostructures such as branched gold nanostars (Fig. 2c),[35] gold bipyramids,[42] gold nanoshells,[43] and cubic Prussian blue NPs.[44] Therefore, the mechanisms of color change using anisotropic gold nanostructures in response to binding interactions typically use direct immobilization, etching, or re-shape growth (Fig. 3).

2.1.2 Silver nanostructures. Silver nanospheres (AgNPs) can be synthesized by reducing silver nitrate with reducing agents in the presence of capping agents.[47] AgNPs from 10 to

Table 1 The molar absorption coefficients (ε) of spherical AuNPs with different sizes

Diameter (nm)	Ligands	SPR (nm)	ε (M^{-1} cm^{-1})	Diameter (nm)	Ligands	SPR (nm)	ε (M^{-1} cm^{-1})
3.76 ± 0.65	Decanethiol		$\sim 3.61 \times 10^6$	25.67 ± 5.62	Citrate		$\sim 2.93 \times 10^9$
4.61 ± 0.48	Citrate		$\sim 8.56 \times 10^6$	30		526	$\sim 3.36 \times 10^9$
5		515–520	$\sim 1.10 \times 10^7$	34.46 ± 4.34	Citrate		$\sim 6.06 \times 10^9$
8.55 ± 0.79	Citrate		$\sim 5.14 \times 10^7$	40		530	$\sim 8.42 \times 10^9$
8.76 ± 1.11	Oleylamine		$\sim 8.79 \times 10^7$	50		535	$\sim 1.72 \times 10^{10}$
10		515–520	$\sim 1.01 \times 10^8$	60		540	$\sim 3.07 \times 10^{10}$
15		520	$\sim 3.67 \times 10^8$	80		553	$\sim 7.70 \times 10^{10}$
20		524	$\sim 9.21 \times 10^8$	100		572	$\sim 1.57 \times 10^{11}$
20.60 ± 1.62	Citrate		$\sim 8.78 \times 10^8$				

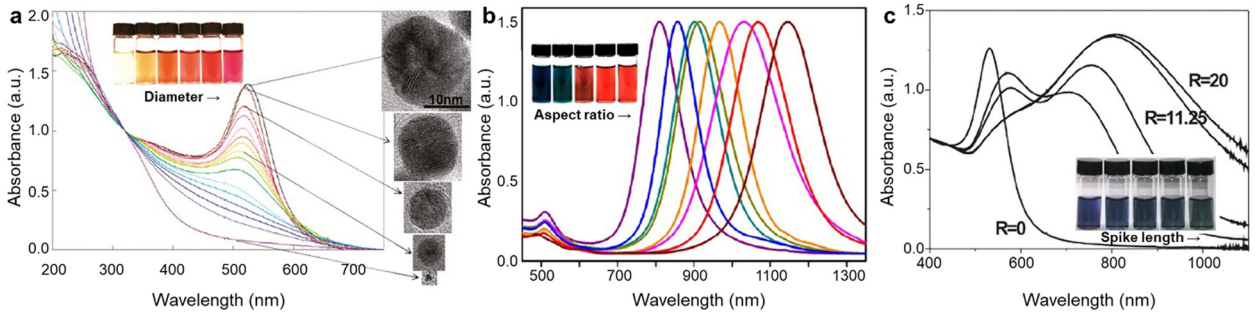

Fig. 2 The absorption profiles and colors of plasmonic gold depend on the size and shape. (a) Gold spheres of increasing sizes from 1–13 nm show an enhanced optical density of the SPR band at ~520 nm, resulting in colors ranging from brown to red.[34] (b) The color of gold nanorod (AuNR) dispersion changes from blue to red with an increasing aspect ratio of NRs, where the longitudinal SPR red-shifts to the NIR regime. (c) Gold nanostar (AuNS) dispersion shifts from blue to green with increasing spike length.[35] (a) Reproduced with permission from ref. 34. Copyright 2010 American Chemical Society. (c) Reproduced with permission from ref. 35. Copyright 2010 American Chemical Society.

Table 2 The molar absorption coefficients (ε) of gold nanorods with different dimensions

Length (nm)	Width (nm)	LSPR (nm)	ε (M^{-1} cm^{-1})	Length (nm)	Width (nm)	LSPR (nm)	ε (M^{-1} cm^{-1})
34	10	750	$\sim 1.34 \times 10^{7}$	75	20	780	$\sim 6.72 \times 10^{9}$
39	10	780	$\sim 3.77 \times 10^{7}$	84	20	808	$\sim 4.57 \times 10^{9}$
43	10	808	$\sim 8.71 \times 10^{7}$	95	20	850	$\sim 3.49 \times 10^{9}$
51	10	850	$\sim 2.35 \times 10^{8}$	120	20	1050	$\sim 7.55 \times 10^{9}$
45	19	640	$\sim 2.79 \times 10^{9}$	68	40	600	$\sim 8.30 \times 10^{9}$
51	20	700	$\sim 1.31 \times 10^{9}$	84	40	650	$\sim 1.55 \times 10^{10}$
66	20	750	$\sim 1.61 \times 10^{9}$	96	40	700	$\sim 3.37 \times 10^{10}$

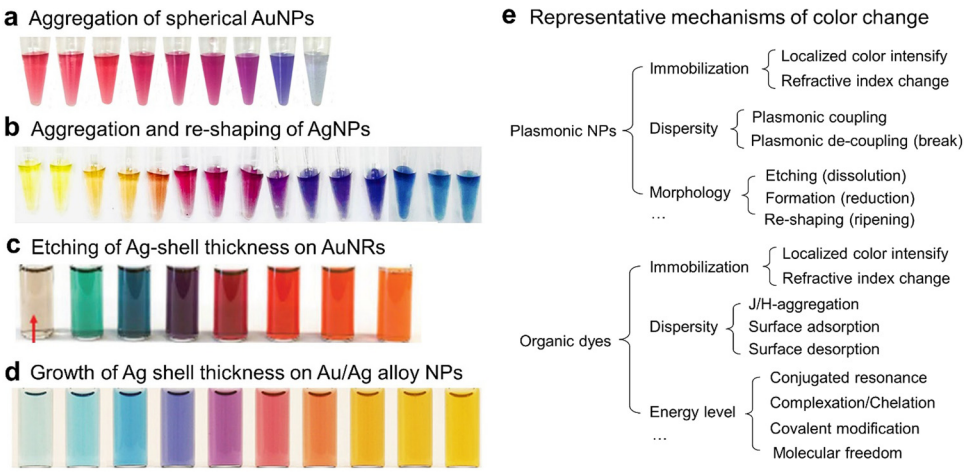

Fig. 3 Representative mechanisms of color changes based on inorganic NPs include: (a) aggregation of AuNPs.[16] (b) Aggregation and re-shaping of AgNPs.[20] (c) Etching of Ag-coated AuNRs.[45] (d) Growth of Ag shell on the Au/Ag alloy NPs.[46] (e) General mechanisms of colorimetric sensing using various colorants. (a) Reproduced with permission from ref. 16. Copyright 2022 Wiley. (b) Reprinted with permission from ref. 20. Copyright 2022 American Chemical Society. (c) Reproduced from ref. 45 (2020) with permission from the Royal Society of Chemistry. (d) Reproduced from ref. 46 in accordance with CC BY-NC-ND 4.0. Copyright 2021 American Chemical Society.

100 nm display a shape and distinctive SPR band within the 400–500 nm range, resulting in an intense yellow color. AgNPs have a high molar absorption coefficient (ε) of approximately 10^{9} M^{-1} cm^{-1}.[48] The optical profiles of AgNPs depend on size, shape, and the surrounding environment (Fig. 4a–c). While AgNPs possess multiple color changes over the visible range (Fig. 3b), they are also reactive, susceptible to oxidation, and can be etched by strong coordinating ligands such as thiolates. The resulting release of Ag complexes could potentially induce toxicity and exhibit antibacterial effects.[49] Therefore, appropriate surface coatings are essential for the biocompatibility of AgNPs. The mechanisms governing color changes in AgNPs typically involve interparticle aggregation, redispersion, and reshape growth (Fig. 3).[17–20]

2.1.3 Alloy nanostructures. Considering human color vision physiology, research has identified an optimal transition zone around 500–550 nm, from cyan to green, for detecting discernible color changes with the naked eye: Small shifts of 2–3 nm within

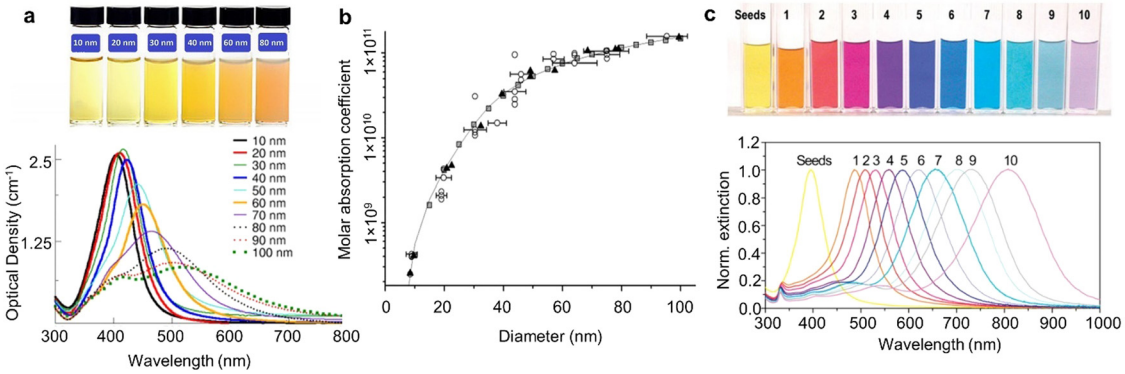

Fig. 4 The absorption profiles and colors of plasmonic silver depend on the size and shape. (a) AgNPs of increasing sizes show a red-shift on the SPR band and color change from light yellow to brown.[48] (b) Molar absorption coefficient of AgNPs of various sizes.[48] (c) Silver nanoprisms of increasing edge-length show red-shift of the SPR and a wide range of color changes.[50] (a) and (b) Reproduced with permission from ref. 48 (2014) with permission from the Royal Society of Chemistry. (c) Reproduced with permission from ref. 50. Copyright 2008 Wiley.

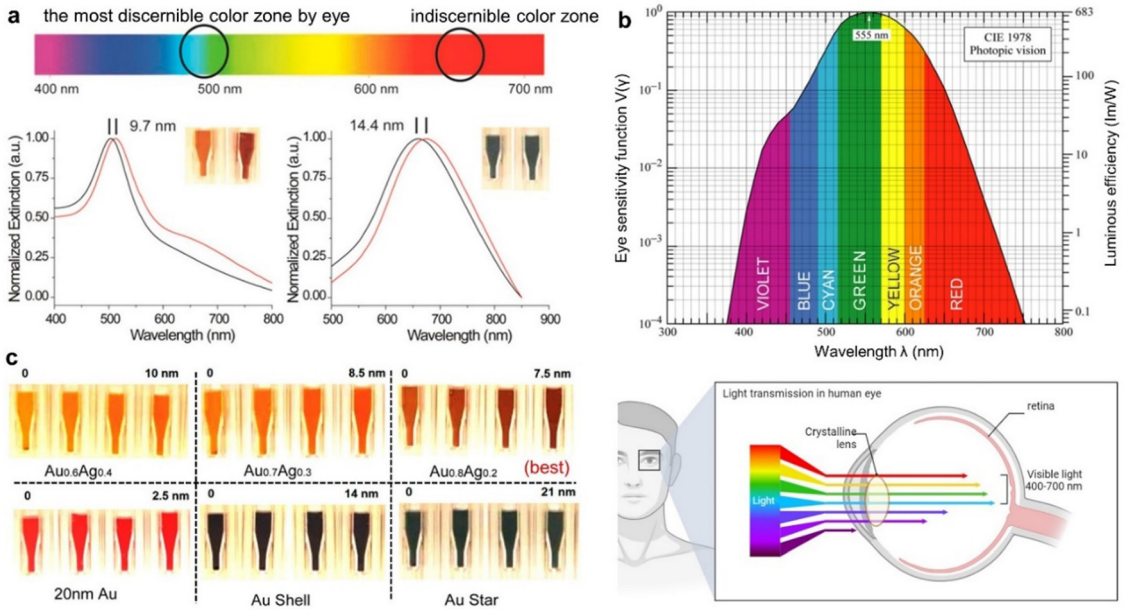

Fig. 5 Colorimetric sensing from the human vision perspective. (a) Corresponding color changes with spectral shifts in the color spectrum.[51] (b) Correlation of eye sensitivity function, $V(\lambda)$, and luminous efficacy of optical power, where $V(\lambda)$ is maximum around 555 nm (after 1978 CIE data).[53] (c) Color changes of various synthesized plasmonic nanoparticles in a solution with increasing refractive indices from left to right: 1.33, 1.36, 1.39, and 1.42.[51] The SPR peak shift is shown on the top. (a) and (c) Reproduced with permission from ref. 51. Copyright 2018 American Chemical Society. (b) Reproduced with permission from ref. 53. Copyright 1978 Wiley.

this range are perceptible (Fig. 5a and b).[51] Tuning the SPR to 500 nm can be readily achieved by adjusting the core compositions in Au/Ag alloy NPs, which can be synthesized through the simultaneous reduction of a mixture of $HAuCl_4$ and $AgNO_3$ in a trisodium citrate solution.[52] For example, alloyed $Au_{0.8}Ag_{0.2}$ NPs exhibit a distinct SPR wavelength at the 500 nm, resulting in the most pronounced color change with minimal SPR shift (Fig. 5c). The sensitivity of a colorimetric sensor based on the blue/red-shift of SPR (due to aggregation, redispersion, or refractive index changes) using these alloy NPs could be significantly enhanced (*i.e.*, 12-fold) when compared to that of AuNPs, Au nanoshells, Au nanostars, AgNPs, and other alloy NPs with varying ratios.[51]

2.2 Organic chromophores

The applications of organic chromophores as color agents are briefly covered in this review; however, they have wide use in colorimetric sensors. Organic chromophores can change colors in response to different physical conditions or chemical reactions. The specific recognition activates the probes with organic chromophores by changing the separation distance,[54,55] structural resonance,[56] complexation state,[57] energy levels, conformation of the chromophore,[58] as well as modifications to its electronic structure or bonding,[59] which alter its absorption and emission properties, resulting in a color shift. These colorimetric chromophores can be broadly categorized into five

Table 3 Representative dyes in colorimetric sensing applications

Dye type	Analyte	Representative Examples	Ref.
Brønsted acid/base	Protons	Litmus, phenolphthalein, bromothymol blue, thymol blue, methyl red	60
Lewis acid	Metal ions, volatile organic compounds	Metalloporphyrins, porphyrins, porphyrinoids	57 and 61
Lewis base	Metal ions	Eriochrome black T, murexide, calcein, hematoxylinm, xylenol orange	57 and 62
Redox indicator	Superoxide ions, hydroxyl radicals, ROS, RNS, thiols, oxidase	Bodipy, eriogreen, methylene blue, phenosafranine, indigo carmine, TMB	57 and 63–65
AIE luminogen	Aggregation behavior	TPE, PyTPE, HPS, BTPETD, TPE-EPA-DCM, TTF, BTD-Se-TPE	66 and 67

classes (Table 3):[13] (i) Brønsted acidic or basic dyes (*e.g.*, pH indicators), (ii) Lewis acid/base dyes (*e.g.*, metal-ion chromogens), (iii) redox dyes, (iv) large dipole dyes (*e.g.*, zwitterionic vapochromic or solvatochromic dyes), and (v) chromogenic aggregative dyes.

2.2.1 Brønsted acid/base dyes. The colors of some Brønsted acids or bases are pH-dependent, including but not limited to litmus (7-hydroxyphenoxazone), phenolphthalein, bromothymol blue, thymol blue, and methyl red.[60]

2.2.2 Lewis acid dyes. Metalloporphyrins are common Lewis acid dyes for colorimetric detecting metal ions, anions, and volatile organic compounds.[57,61] This is attributed to (i) their NH moieties that facilitate anion binding through cooperative hydrogen bonding, (ii) the presence of multiple pyrrolic N atoms for selective chelation of metal ions, (iii) the flexible designability to adjust ion selectivity and sensitivity through varying macrocycle size and peripheral substitution, and (iv) their capacity to undergo significant color changes, including wavelength and intensity shifts in strong π–π* absorbances when binding with ligands. In nature, hemoglobin has a heme group with a porphyrin ring and an iron ion at the center, which can bind with oxygen for oxygen transport. The color of hemoglobin depends on the iron ion: Fe^{2+} gives it a red color, while Fe^{3+} makes it deep red or green (Fig. 6a). A pale or yellowish color of the skin and mucous membranes could indicate iron-deficiency anemia due to a lack of iron in the blood. Hemocyanin is structurally similar to hemoglobin (*e.g.*, in horseshoe crabs, octopus, squid) but contains copper instead of iron, giving it a blue color when oxygenated.

2.2.3 Lewis base dyes. Ionochromic dyes are common Lewis bases that enable strong coordination with metal ions and induce a rapid color change. For instance, Eriochrome Black T can detect Ca^{2+}, Mg^{2+}, and Al^{3+}. Murexide is employed to identify Ca^{2+}, Ni^{2+}, and Eu^{3+} (Fig. 6b and c). Calcein is specifically utilized to detect Ca^{2+}, while Cu^{2+} detection is achieved with hematoxylin and xylenol orange serves the purpose of detecting Ga^{3+}, In^{3+}, and Sc^{3+}.[57,62]

2.2.4 Redox indicator dyes. A variety of organic dyes can undergo color changes in redox reactions, such as bodipy, *o*-dianisidine, diphenylamine, eriogreen, fenamic acid, methylene blue (MB), methylene green, phenosafranine, indigo carmine, Nile blue, 2,2′-bipyridine, neutral red, dicationic tetraarylbutadiene,[63] and tetramethylbenzidine (TMB).[57] MB is a commonly utilized indicator to visualize electron transfer reactions (Fig. 6d) such as photoreductive activities in alkaline

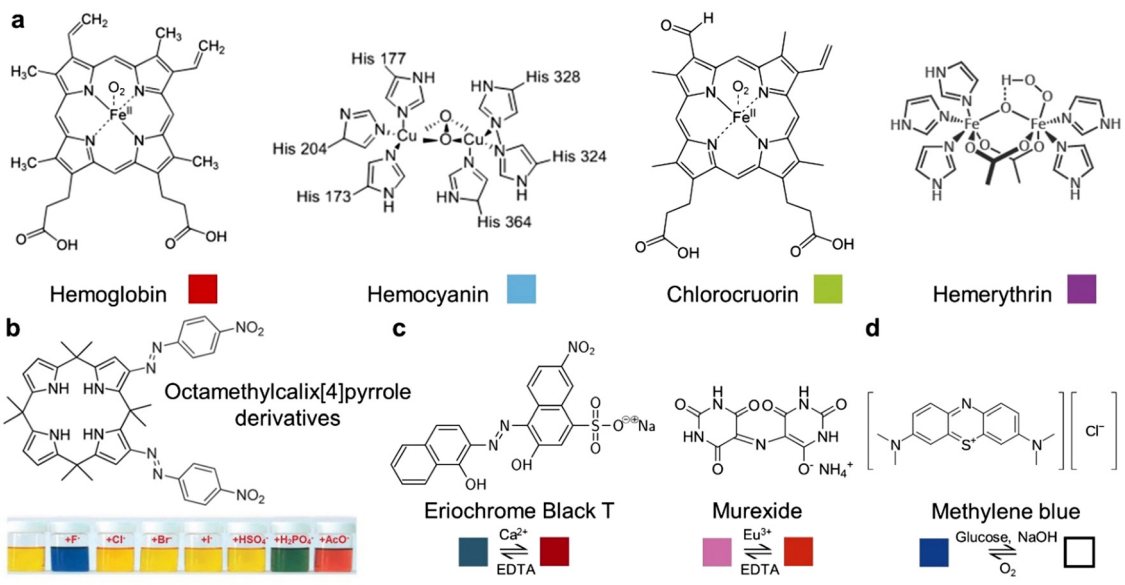

Fig. 6 Organic chromophore colorants. (a) Oxygenated blood from different species shows various color due to different metallocomplexes with ions. (b) The calix[4]pyrrole-based colorimetric chemosensors for anions.[68] (c) Ionochromic dyes. (d) MB is a redox indicator dye in alkaline conditions. (b) Reproduced with permission from ref. 68 (2010) with permission from the Royal Society of Chemistry.

conditions.[64,65] TMB is frequently employed as a substrate for the detection of oxidase presence or glucose detection.

2.2.5 Chromogenic aggregative indicators. Aggregation-induced emission luminogens (AIEgens) display enhanced fluorescence when molecular motion is restricted, often leading to minor visual color changes. This can occur through confinement (*e.g.*, pocket, liquid condensate, aggregate) or extreme physical conditions (low temp.). The AIEgens are tunable with emission colors from blue (*e.g.*, TPE, PyTPE) to green (*e.g.*, HPS, BTPETD), and even red or near-infrared (*e.g.*, TPE-EPA-DCM, TTF, BTD-Se-TPE).[66,67] These molecules are garnering increasing interest in bioimaging; however, they will not be detailed in this review due to the focused colorimetric topic.

Many other dyes not in the above categories are also widely used. Indocyanine green (ICG) accumulates in certain cancers, aiding in tumor coloration for surgical operation. ICG and Cyanine7.5 derivatives with a nucleophilic group could change color from green to brown at high pH through reversible backbone-cyclization, useful for pH sensing. CRANAD-2, a curcumin derivative, changes from colorless to purple with beta-sheet protein aggregates due to increased solubility *via* hydrophobic interactions.

2.3 Other hybrid colorants

Hybrid organic/inorganic chromophores have the potential to advance analyte sensing due to their tunable optical profiles, improved sensitivity and selectivity. Examples include melanin NPs, Prussian blue NPs (for redox analytes), conducting polymers (*e.g.*, polyaniline, polypyrrole), chromophoric covalent–organic frameworks (COFs), and metal–organic frameworks (MOFs).[59,69–73]

Melanin is a naturally-occurring biopolymer associated with various skin and eye conditions and serves as an indicator for melanoma. Polydopamine (PDA) NPs exhibit melanin-like optical properties and biocompatibility.[74] Their optical spectra are affected by size, solvents and molecular adhesion due to the high refractive index and catechol groups. Shim *et al.* designed PDA NP thin film exhibited significant change in reflection spectrum in response to different alcoholic solvents.[75] Jokerst *et al.* developed hollow PDA nanocapsules (PNCs) loaded with various dyes, taking advantage of the catechol-mediated adhesive nature.[76] The dye-loaded PNCs showed 10-fold enhanced photoacoustic signal compared to free Nile Blue dye, enabling direct detection of heparin in whole human blood (Fig. 7a). The multiple interactions between heparin and dye released from PNC also caused color shift due to heparin-dye aggregation, providing visual heparin detection.

COFs are porous and structurally precise polymer networks with versatile chemical functionality and tunable porosity. Tuning the porosity of COFs enables them to host specific ions or molecules, making them great candidates as sensing agents. Wang *et al.* developed a triformylphloroglucinol diaminoanthraquinone (TPDQ)-COF that selectively senses Fe^{2+}/Fe^{3+} ions *via* a color change from colorless to yellow.[79] The absorption spectrum change is due to ligand-to-metal charge transfer within the TPDQ-COF framework, and the ion selectivity is achieved by matching the ionic radius and the binding energy with the COF pore. Solvatochromism is an alternative mechanism in COF-based colorimetric sensors, where solvent polarity triggers a reversible color change due to differences in the solute's ground and excited state energies, thus leading to intramolecular electronic transitions.

Bein and Auras *et al.* reported a tetrakis(4-aminophenyl)-pyrene-based COFs as a solvatochromic sensor for a reversible color change from orange to dark red when exposed to humidity or solvent vapours (Fig. 7b).[77] The solvatochromic effect in

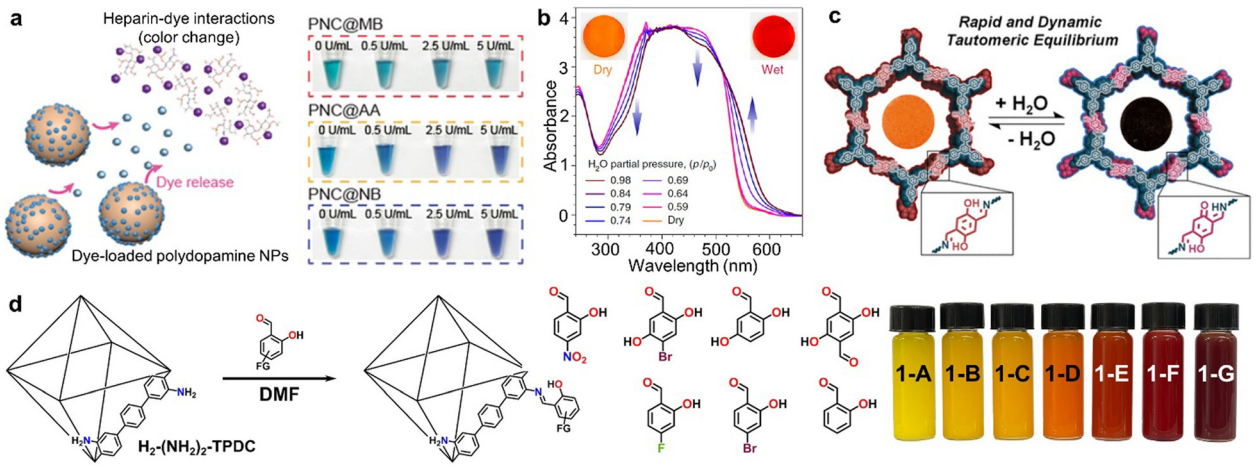

Fig. 7 Hybrid colorants for colorimetric sensing. (a) Dye releasing in negatively charged polydopamine nanocapsules (PNCs) for heparin sensing, MB, AA and NB represent methylene blue, Azure A and Nile blue dye respectively.[76] (b) UV-Vis absorption spectra and white light picture of the pyrene-thieno[3,2-*b*]thiophene (Py–TT) based COF film recorded at different relative pressures of H_2O in N_2.[77] (c) COFs for humidity sensing enabled by diiminol tautomerization, the representative color change was shown in the middle of COF structure.[78] (d) Color-tunable MOFs made by postsynthetic modification of the chromophoric linkers of an amino-functionalized UiO-68 MOF.[59] (a) Reproduced from ref. 76 in accordance with CC BY-NC-ND 4.0. Copyright 2021 American Chemical Society. (b) Reproduced from ref. 77 in accordance with CC BY 4.0. Copyright 2018 Nature. (c) Reproduced with permission from ref. 78. Copyright 2020 American Chemical Society. (d) Reproduced from ref. 59 in accordance with CC BY 4.0. Copyright 2023 American Chemical Society.

this COF is controlled by the aldehyde used during assembly, with the most pronounced effect observed for tetraphenylpyrene and thieno[3,2-b]thiophene causing a 20–30 nm shift in absorption spectra. While the solvatochromic response with donor–acceptor contrast is notable, it results in a minor absorption shift due to the stabilization of an excited state with charge-transfer character. Marder *et al.* designed a COF with 2,5-dihydroxyterephthaldehyde: It had dynamic iminol-to-ketoenamine tautomerism in response to water, thus resulting in a new absorption peak at 600 nm (Fig. 7c).[78] This COF-based colorimetric humidity device remained functional for two months for water vapor detection.

Metal–organic frameworks (MOFs) are periodic arrays of molecules that can spatially organize a wide variety of organic chromophores to form color-tunable hybrid materials for molecular sensing. Rosi *et al.* precisely controlled the color in the UiO-68 MOFs of 3,3″-diamino-1,1′:4′,1″-terphenyl-4′,4″-dicarboxylate and Zr using a library of aromatic aldehyde modifiers *via* post-synthetic modification (PSM).[59] The PSM imine condensation extends the π-conjugation and produces new chromophores, thus resulting in a series of MOFs with expanded absorption across the visible spectrum due to altered band gaps. This yields colors ranging from light yellow to dark brown (Fig. 7d).

3. Other elements of colorimetric sensors

3.1 Sampling

Testing samples fall into three main categories: human, food, and environment. Human health diagnosis involves examining various clinical specimens like whole blood, plasma, serum, sweat, urine, mucus, stool, saliva, exhaled breath condensate, and nasal swabs.[16,80] Food samples are utilized to evaluate conditions like putrefaction, with matrices including juices, cereals, milk, meat, and vegetables.[81] Environmental sampling targets pollution assessment, typically involving samples from water, soil, plants, and airborne particulate matter.[82] Sampling for colorimetric sensing often includes removing or altering color interference to measure the target color. This can be achieved through methods such as filtration,[83] chemical reagents (*e.g.*, reducing, oxidizing, and chelating agents),[84] light polarization[85] as well as calibration using reference standards to compensate for interference.

Clinical samples are used to identify a variety of human health including infection, cholesterol, nutrient deficiency, cancer, anemia, and more. In addition, the common example of clinical analysis is based on urinalysis which might screen liver or kidney issues, diabetes, and urinary tract infections.[86] Collection methods and target analytes depend on the sample types and purpose. For example, invasive blood tests determine the health condition of diverse organs including kidneys, liver, heart, and others based on the levels of enzymes, proteins, thyroids, metabolites, and other biomarkers.[87,88] Likewise, the number of platelets, white and red blood cells may diagnose blood cancer, infection, immune system disorder, and nutritional deficiency[89] Invasive biopsies analyze the cellular composition and structural integrity of various tissues, such as skin, muscle, and organs, aiding in the diagnosis of conditions ranging from cancer to inflammatory diseases. Collecting saliva or exhaled breath condensate (EBC) is non-invasive and requires no clinicians to draw specimens. Saliva is composed of complex components such as urea, glucose, cholesterol, amino acids, lectin, peroxidase, amylase, ions, and more than 700 microorganisms which are used to diagnose oral diseases.[90] EBC is the liquid phase of the exhaled air sampled by cooling and condensation of the exhaled aerosol.[91] EBC could contain DNA, RNA, protein, metabolites, and volatile organic compounds (VOC) which may diagnose biomarkers associated with lung cancers and other respiratory disorders such as asthma, cystic fibrosis, and coronavirus diseases.[92] Urinalysis is another non-invasive test to screen the health conditions of liver and kidney, and diagnose diabetes, urinary tract infections, and bladder tumors.[86] Other clinical samples such as tear fluid is used to examine eye diseases, and sweat has been used for monitoring level of glucose, pH, and metabolites.[93,94] Table 4 summarized the commercially available clinical testing kits at home.

Food safety is a global concern, and quality monitoring (*e.g.*, spoilage, poisoning, *etc.*) involves checking for microbial agents (*e.g.*, decarboxylases, lipases, *etc.*), toxic/heavy ions, pesticides, veterinary drugs, and preservatives (*e.g.*, formaldehyde, bisulfite, sulfur dioxide), along with genetically modified food genes.[95,96] In addition, environmental pollutants are used to diagnose environmental health which can potentially cause health problems to human such as respiratory diseases, heart diseases, and some types of cancers.[97] Water is essential for all biological life, and aquatic toxicity testing are routinely used worldwide. A number of standardized toxicity test protocols assess chemicals in water, sewage, discharge, pesticides, wastewater, industrial effluents, the response, and survival rate of aquatic organisms upon exposure of effluents.[98] Air quality assessment monitors pollutants in air such as nitrogen oxides, particulate matter (*e.g.*, PM 2.5), ozone, lead, sulfur dioxide, and carbon dioxides.[99] Soil sampling diagnoses microbial activity, nitrogen, biomass, and others which are necessary to maintain agricultural ecosystem.[100]

The sampling device must be designed to collect the desired samples selectively and effectively. Factors to consider include sample volume, types (*i.e.*, liquid, gas, and solid), and any potential interfering substances in the sample. For example, syringes or pipettes are used to collect liquid samples such as polluted water. Sterile tubes and cups are commonly used to obtain biofluids including urine, saliva, and other body fluids. Swabs can collect samples from anterior nares, mid-turbinate, nasopharyngeal, and oropharyngeal regions. Filters with different pore sizes can be used to collect particulate matter from air or water samples which can be analyzed using colorimetric sensors. Solid-phase microextraction fibers are used to collect VOCs from air or other gaseous samples.[101] Microfluidic chips are POC diagnostic devices that can separate cells based on different densities as well as analyze small volumes of liquid samples such as blood or saliva.[102] Breath condensate collectors require R-tubes, cooling sleeves, and diametric masks. The frequency of

Table 4 Commercially available at-home clinical testing

Clinical test	Sample type	Collection tool	Diagnosis	Commercial product
Urinalysis	Urine	Strip	Leukocytes, nitrite, pH, urobilinogen, protein, ketone, bilirubin, vitamins	life2O, Palinoia, AZO, Diagnox health, healthy.io
		Test kit	Human chorionic gonadotropin (hCG) for pregnancy test	FIRST RESPONSE, Clearblue, Clinical guide
Blood test	Blood	Finger-prick blood sample	eGFR creatinine, BUN, albumin levels for kidney health	Verisana, LetsGetChecked, Labcorp OnDemand,
			Helicobacter pylori (*H. pylori*) infection	Evuioas, OUROZO
			Blood glucose for diabetes	Metene, Mckesson, iHealth, CareSens, AUVON, JJCare Caretouch
			Estradiol, Progesterone, Luteinizing hormone, dehydroepiandrosterone (DHEA), Cortisol Free T3, T4 for hormone test	Everlywell, Quest
Respiratory viral test	Respiratory droplets	Nasal swab	Viral infections: SARS-CoV-2, influenza virus A and B, respiratory syncytial virus (RSV) A and B.	Applidx, GoodRx, iHealth, Labcorp OnDemand
Saliva test	Saliva	Oral swab, Tube	Viral infection: SARS-CoV-2, human immunodeficiency virus (HIV), cortisol	P23 Labs, ORAQUICK, LetsGetChecked
Sweat test	Sweat	Patch, tube	Hydration, electrolytes levels	LEVELEN
Drug test	Urine, Saliva	Cup, Oral swab	Alcohol, codeine, fentanyl, heroin, hydrocodone, cocaine, ketamine, oxycodone, morphine, marijuana	Prime Screen Identity Diagnostics, TOCCA Screen

sample collection and sample storage conditions can vary depending on the purpose of diagnosis and downstream applications.[103–106]

3.2 Recognition components

Colorimetric sensors must comprise one or multiple recognition sites (or receptors) for interacting with the target analyte. We discuss three typical types of interactions involved: stimuli-driven interactions, analyte-driven non-covalent interactions, and covalent bonding.

3.2.1 Stimuli-driven interactions. Environmental stimuli such as pH, light, magnetic field, and temperature can be reported colorimetrically through a modulation of NP dispersity.[107] For example, surface charge governs a major part of colloidal stability of the NPs according to the Derjaguin–Landau–Vervey–Overbeek (DLVO) theory and the Schulze–Hardy rule.[108,109] NPs with strongly positive or negative charge are colloidally stable due to their electrostatic double layer. Acidic or basic conditions could alter NP dispersity due to either (de)protonation of surface ligands or changes in Debye length and double-layer potential, which in turn induce plasmon coupling and color changes.[108] Klajn *et al.* summarized fundamental guidance on the N-shape aggregation of NP (superion) during counterion titration, which deviates from the sigmoidal S-shape observed in traditional anion-cation titrations.[110] Grzybowski *et al.* demonstrated that AuNPs covered by a self-assembled monolayer of 2-fluoro-4-mercaptophenol ($pK_a \sim 8.3$) were dispersed at pH of 12.5 while aggregated at low pH of 7 due to protonation of phenol groups; this in turn induces color change from red to purple (Fig. 8a).[111]

Temperature can cause self-assembly of AuNPs by changing viscosity of the solvent. Yin *et al.* showed bis(*p*-sulfonatophenyl)-phenylphosphine (BSPP)-coated AuNPs were self-assembled through van der Waals attractions at a low temperature. This occurred as the solvent containing 2 wt% agarose, formed a hydrogel below 40 °C, leading to an increase in viscosity of the system that brought close contact between AuNPs@BSPP. Upon reaching 70 °C, the aggregated AuNPs reversibly dispersed due to a decrease in viscosity (Fig. 8b).[112] Likewise, thermo-responsive polymers can lead to NP self-assembly.[115] NPs with intrinsic magnetic properties such as iron can respond to magnetic fields. Duan *et al.* demonstrated that iron oxide NPs (IONPs, Fe_3O_4) align with the direction of applied magnetic fields (Fig. 8c). Upon further coating these aligned nanoparticles with polydopamine, they undergo a color change and acquire multifunctional properties.[113] In addition to magnetic field, UV light can induce inter-particle interactions. Lu *et al.* showed a heterodimer composed of Ag and Fe_3O_4 nanoparticles coated with poly *n*-isopropylacrylamide (PNIPAM) self-assemble in response to UV light.[114] When nanoparticles are exposed to sunlight, the absorbed light energy is converted to heat energy, causing an increase in temperature. The generated heat energy collapsed the PNIPAM chain, reducing steric barrier among the heterodimers; this in turn induces particle aggregation (Fig. 8d). Once sunlight illumination is removed, the aggregated heterodimers reversibly dispersed at the temperature below their low critical solution temperature.

3.2.2 Analyte-driven non-covalent interactions. Colorimetric sensors employ a diverse type of non-covalent interactions including electrostatic interactions, hydrogen bonding, dipole–dipole interactions, π–π stackings, hydrophobic interactions, metal chelation, biotin-avidin interactions, aptamer-receptor, antibody-receptor, DNA hybridization, and coiled-coiled peptide interactions, *etc.*[116–118] Non-covalent interactions are utilized to the utmost by biological systems: The higher-ordered structures of proteins, DNA, and RNA involve interactions with more than one non-covalent bonds, ensuring specificity and selectivity.[17,117,119] Non-covalent interactions can occur over longer distances, *e.g.*, electrostatic and hydrophobic interactions can span tens of nanometers.[117] The strength of non-covalent interactions are 10–100 times weaker than covalent bindings (Table 5). While inherently weaker, these non-covalent interactions are additive and thus still strong enough to drive the self-assembly of NPs for colorimetric

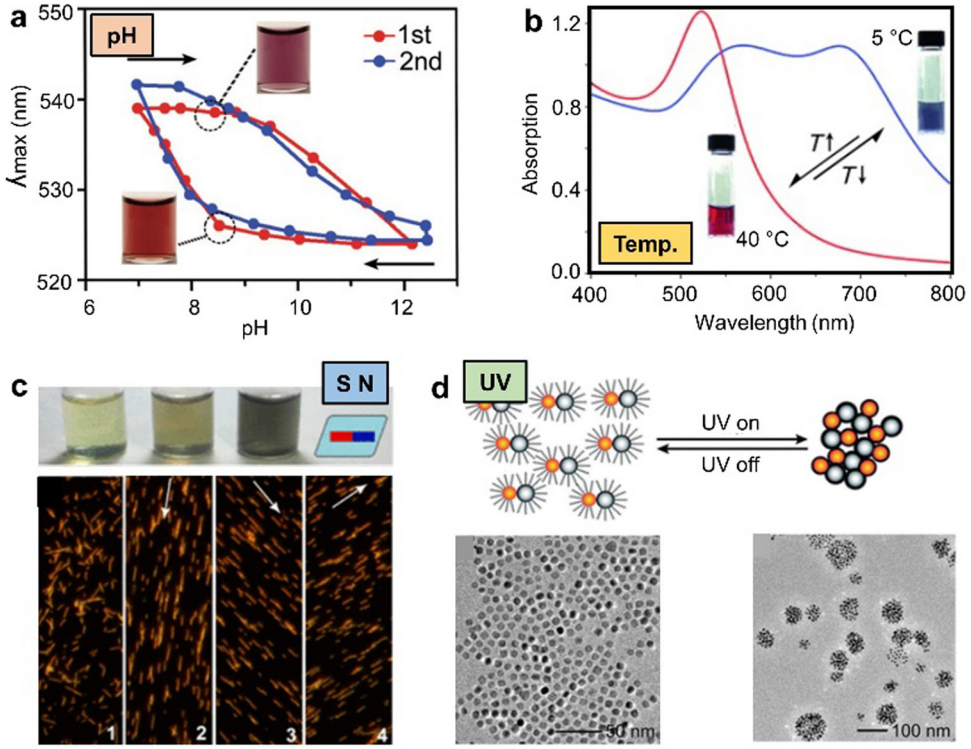

Fig. 8 Stimuli-driven aggregation/dissociation of nanoparticles. Environmental stimulus such as (a) pH,[111] (b) temperature,[112] (c) magnetic field,[113] and (d) UV light can induce assembly or disassembly of nanoparticles and thus a color change.[114] (a) Reproduced with permission from ref. 111 (2010). Copyright 2010 American Chemical Society. (b) Reproduced with permission from ref. 112. Copyright 2012 Wiley. (c) Reproduced with permission from ref. 113. Copyright 2015 American Chemical Society. (d) Reproduced with permission from ref. 114 (2013) with permission from the Royal Society of Chemistry.

Table 5 Types of non-covalent interactions and their strengths[117]

Non-covalent interactions	Schematic illustration	Strength (kJ mol^{-1})
Electrostatic interaction		5–100
Hydrogen bond		5–150
Dipole–dipole interaction		5–50
π–π stacking		0–50
Hydrophobic interaction		0–50

diagnostics. For example, polyphenol-based nanostructures readily form a robust supramolecular network involving π–π stackings and hydrogen binding due to their unique chemical structure. This characteristic enables them to interact with diverse inorganic or organic molecules for biosensing.[120,121] Biotin-avidin interaction is the strongest non-covalent interaction between a protein and ligand: The dissociation constant (K_d) of biotin-avidin is 10^{-15} M.[122] These biotin-avidin bindings are rapid, stable, and relatively specific, thus making them highly promising for colorimetric diagnosis of diverse analytes.[123,124] Monoclonal and recombinant antibodies are ideal biorecognition elements that provide sensors with high specificity and sensitivity and have been used in varieties of immuno-sensing assays.[125] Lastly, DNA hybridization where two complementary single-stranded DNA molecules form a double-stranded molecule, and aptamer-receptor binding have been extensively studied for sensing applications due to its high selectivity.[126]

3.2.3 Covalent bonding. Covalent crosslinking of NPs is popular for colorimetric diagnostics including Au–S bondings,[127] click cycloaddition,[128] 3-cyanovinylcarbazole,[129] and boronate ester bonding, *etc.*[130] The Au–S binding is a well-known "covalent bond" where thiol groups (soft Lewis base) readily adsorb onto the reduced gold surface (soft Lewis acid) based on the Hard and Soft Acid and Base (HSAB) theory. Using this robust mechanism, peptides containing head and tail thiol have been studied for aggregation or dissociation of AuNPs.[131] Boronate esters exhibit dynamic covalent functionalities with catechol groups capable of assembling AuNPs for diagnostics. Kay *et al.* demonstrated that 1,2-dihydroxybenzene (*i.e.*, catechol) covalently linked with boronate esters monolayers on AuNPs, resulting in particle aggregation (Fig. 9a).[130] Enzymes or other stimuli can activate covalent bonding for sensing applications. For example, Gao *et al.* showed that peptide-modified AuNPs aggregated in the presence of legumain, a target enzyme, through click cycloaddition.[128] The proteolysis of legumain triggered click cycloaddition between

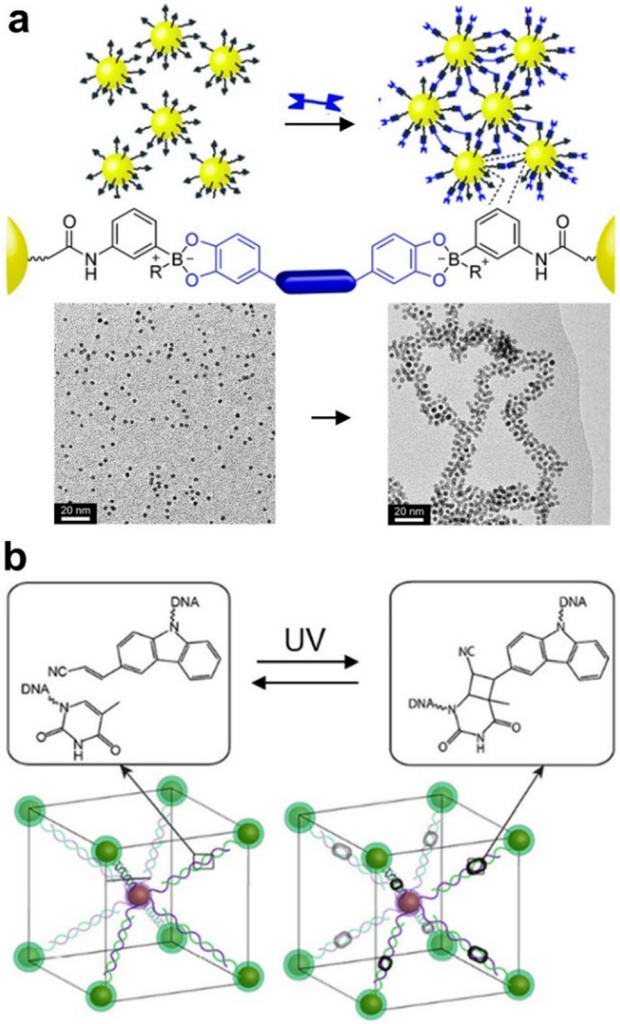

Fig. 9 Nanoparticle assembly driven by covalent bonding. (a) Boronate ester.[130] (b) 3-Cyanovinylcarbazole formed covalent binding which induces assembly or disassembly of nanoparticles.[129] (a) Reproduced with permission from ref. 130 (2016) with permission from the Royal Society of Chemistry. (b) Reproduced from ref. 129 in accordance with CC BY 4.0. Copyright 2019 American Chemical Society.

1,2-thiolamino group and cyano group on the peptide ligands, leading to an aggregation of AuNPs due to the formation of covalent bonds. Beyond enzyme-based approach, light can also induce covalent binding for the assembly of AuNPs. Kanaras *et al.* demonstrated that DNA-coated AuNPs functionalized with cyanovinylcarbazole can reversibly form a covalent bonding upon irradiation with UV light at 315 nm (Fig. 9b). UV light induced the formation of cyclobutene bonds between the cyanvinyl moieties on the DNAs, leading to the crosslinking of AuNPs. The forthcoming Sections 5 and 6 delineate the applications of individual recognition and interaction processes along with their respective mechanistic details.

3.3 System readout

Colorimetric assays should be simply interpreted by the naked eye. In addition, a variety of complementary techniques including smartphone analysis,[132] spectrophotometry,[108] standard color charts (or RGB values),[133] and statistic pattern analysis (by smartphone, artificial intelligence, or machine learning; see Section 5) have been used to obtain more quantitative readouts. Positive and negative controls play crucial roles in minimizing variables in biosensors. Positive controls exhibit a color change upon sample detection. In contrast, negative controls do not show any color change because they lack the target analytes. The defined readout time may vary depending on the sensors' sensitivity and selectivity toward target analytes and the types of analytes.[16,134] Given that colorimetric sensing is closely correlated with optical properties, spectrophotometry serves as a fundamental method for quantifying optical signal readouts. Optical signals can be defined as wavelength shift, intensity change, or color pattern evolution over time. In principle, the limit of detection (LoD) is characterized as the lowest analyte concentration that could be differentiated from the limit of blank (LoB) with a sufficient degree of confidence or statistical significance ($p < 0.05$). The LoB defines the highest signal generated from a sample without analytes. LoB can be calculated using the mean ($\text{mean}_{\text{blank}}$) and standard deviation (SD_{blank}) of a blank sample with following equation:[135]

$$\text{LoB} = \text{mean}_{\text{blank}} + 1.645\ (\text{SD}_{\text{blank}})$$

The LoD is then measured based on the LoB value with the standard deviation of the lowest concentration samples ($\text{SD}_{\text{lowest conc.}}$) with following equation:[135]

$$\text{LoD} = \text{LoB} + 1.645\ (\text{SD}_{\text{lowest conc.}})$$

It is important to report LoD value concomitant with comprehensive disclosure of assay conditions, encompassing parameters such as readout time, temperature, matrix composition, among others.

4. Point-of-care (POC) devices for translational applications

POC diagnostics, performed near the patient, offer a strategy for real-time, rapid, and precise detection at the patient's point of need. Colorimetric POC devices rely on color changes to detect specific substances in bodily fluids like blood, urine, sweat, or saliva and are valuable tools in healthcare settings. They provide swift and accurate diagnostic results right at the POC, enabling timely treatment and health condition management. Although the wearable colorimetric device market is still in its early stages, it is poised for rapid expansion. According to a report by GlobeNewswire, the global wearable sensor market is projected to reach $5.68 billion by 2030, with a compound annual growth rate of 15.20% from 2022 to 2030.[136] These POC devices come in various forms, including commercially available LFAs, microfluidic paper-based analytical devices (μPADs), and wearable sensor devices, all characterized by their unique mechanisms and advantages (Table 6).

4.1 Lateral flow assays (LFAs)

LFAs are among the most commonly used POC colorimetric sensors for out-of-laboratory diagnostics.[137,138] The discernible

Table 6 Summary of POC sensor techniques

	LFAs	μPADs	Wearable sensors
Examples	Pregnancy tests, COVID-19 rapid antigen tests, *etc.*	N/A	Fitbit, Apple Watch, *etc.*
Mechanisms	Colorant immobilization	Colorimetric reactions, magnetic detection, fluorescence, or electrochemical assays	Optical, acoustic, or electrochemical sensors
Strength	Rapid results, naked eye detection, simple operation, no equipment needed	Low-cost, massive printing fabrication, flexible portability, spatial-resolved multi-analysis	Continuous, real-time monitoring, non-invasive, personalized healthcare, quantitative results, wireless communication
Limitation	Limited sensitivity, false positives/negatives, qualitative not quantitative, no sample recycling, short shelf life, may require low temp storage	Not optically transparent, no sample recycling, limited uniformity and reproducibility in paper manufacturing, coffee ring effect on sample distribution	Expensive, short battery life, limited to analyzing physical activities, concerns about data privacy and security
Scenarios	Home-based testing, POC diagnosis of infectious diseases in clinics or remote areas	Environmental, foodborne disease monitoring, public health testing	Continuous health monitoring, fitness tracking

colors of LFAs manifest in both spatial localization and intensity of the nanoparticle expression. LFAs employ an engineered test strip to detect the presence or absence of a target analyte, thereby yielding qualitative results (*i.e.*, yes or no). The first designed LFA was a rapid test for insulin in human blood plasma which became a breakthrough technology over 60 years ago.[139] Dating back to the 1970s with the pregnancy test strip, and more recently the COVID rapid tests, LFAs are well known and widely used in end-user testing due to their simplicity and affordability. Today, LFAs, with various types and custom designs, serve diverse roles in medical, veterinary diagnostics, drug testing, food safety, and environmental contaminant detection.[137,140]

4.1.1 Mechanism of action. A typical LFA consists of a test strip that contains a sample pad, a conjugate pad with colorimetric reagents, a membrane base with immobilized capture molecules for a test line and control line, and an absorbent wicking pad (Fig. 10a). When a sample is applied to the sample pad (Fig. 10b and c), it mixes with the conjugate and flows through the test strip *via* capillary force, where it interacts with the capture molecules along the membrane, causing a visible color change.[141] Parolo *et al.* offer a thorough description of each element with design considerations and a tutorial for developing and troubleshooting LFAs.[137] The ''reporter nanoparticle'' is the particle causing the colorimetric change, and sometimes referred to as the label or marker. AuNPs of 40-nm (Section 2.1) are often used as the reporter in LFAs due to their easy functionalization, SPR properties, and high molar absorption coefficient producing a strong visual signal. Other reporters such as silver nanoparticles of different shapes, quantum dots, latex beads and fluorescent dyes are also used in LFAs (Fig. 10d).[142] The ''target analyte'' is the substance in the sample that the LFA is designed to detect, and the ''affinity ligand'' is engineered to conjugate and bind to both the reporter nanoparticle and the target analyte. These can consist of a wide range of elements specific to recognition of the target analyte, such as aptamers or antibodies (Section 3.2).[143] The ''membrane base'' includes the ''test line'' for target analyte presence and the ''control line'' for sample flow confirmation.

Generally, there are two types of LFAs: sandwich and competition arrangements.[141] In sandwich LFAs, both the reporter nanoparticle and the membrane base test line feature an affinity ligand. When the target analyte is present in the sample, it binds to both the reporter nanoparticle and the test line, forming a ''sandwich'' structure with the analyte in the middle. However, at very high analyte concentrations, hook effects may occur, where a single target analyte can saturate most or all of the binding sites on the reporter and the test line, preventing the formation of the sandwich structure. They are also more likely to produce false positive results.[137] In a competition LFA, the test line on the membrane base contains the target analyte. When the sample contains the target analyte, it binds to the reporter nanoparticle, preventing it from binding to the test line, resulting in a positive result due to the absence of a visual signal. Conversely, when the sample lacks the target analyte, the reporter nanoparticle binds to the test line, leading to a negative result indicated by a visible signal. This arrangement is generally used for smaller analytes (<1 kDa) that do not have space to bind to the affinity ligand more than once.[137]

When designing an LFA there are several important considerations. The affinity ligand must have a strong affinity and fast binding kinetics to the target analyte. The design of this receptor is often the most important aspect.[137] The timing of the reaction and stability of the reagents and products must also be considered.[137] For the reporter nanoparticle to serve as an optimal visual label, the main objective is to maximize the contrast with the membrane base and background. AuNPs have a red appearance, which can pose challenges when analyzing blood samples, often necessitating the use of sample filtration. In contrast, silver NPs typically appear yellow, and this may not provide a strong contrast against a light background. The type and sizing of the particle impact the optical properties of absorbance and strength of the signal.

4.1.2 Strengths, limitations and developments. Simple colorimetric tests remain critical for rapid testing and controlling the spread of infectious diseases, even as newer technologies enhance LFAs as point-of-care diagnostics. For example, the 2014–2015 Ebola epidemic in West Africa was eliminated

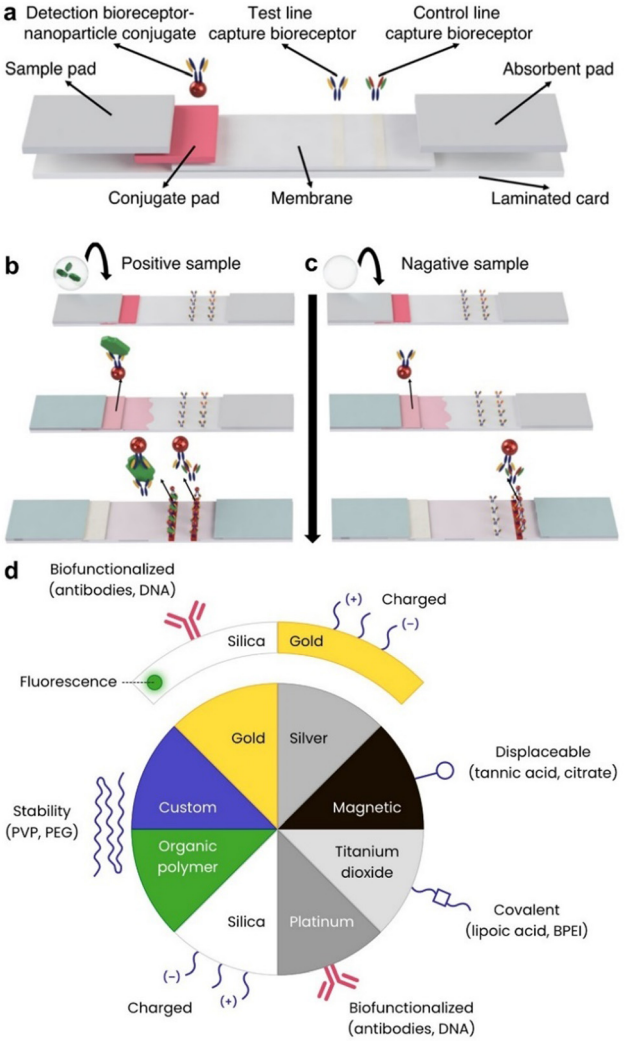

Fig. 10 Lateral flow assays (LFA) mechanism. (a) Typical LFA layout comprising: a sample pad for sample application, a conjugate pad with reporter nanoparticle conjugates for binding, a membrane base housing test and control lines, and an absorbent pad for capillary sample movement.[137] Positive (b) and negative (c) sample LFA schematics.[137] Positive reading indicated by two reporter nanoparticles on the test and control lines. Negative reading indicated by one nanoparticle on the control line only. (d) Common reporter nanoparticles used in LFAs and bonding types.[141] (a)–(c) Adapted with permission from ref. 137. Copyright 2020 Nature. (d) Adapted with permission from ref. 141. Copyright nanoComposix.

through a simple, rapid, and cost-effective LFA test strip: The LFA replaced the slow and expensive RT-PCR tests, providing a quick diagnosis without the need for temperature-controlled blood storage.[139] Constantly evolving areas for LFAs include improving the limit of detection and enhancing analyte specificity, the detection of multiple analytes or multiplexing, and the production of quantitative results.[144] Modern LFAs incorporate several strategies, including the use of optimal reporter nanoparticles for labeling and conjugation,[145] signal amplification, and the integration of traditional LFAs with other detection methods, specialized reading devices, and machine learning.[139,146]

Modern LFA configurations have accomplished spatial multiplexing by incorporating more than one test zone on the strip and engineering the affinity ligands for specificity to each target analyte.[138] This has been designed for testing multiple controlled substances in urine samples and is becoming more common for testing various viral or bacterial pathogens.[139] For example, the first commercially available multiplexed LFA system was demonstrated in 2015 for testing of *Streptococcus pneumoniae* and *Legionella pneumophila* in urine samples. Newer label types such as quantum dots have been demonstrated for simultaneous detection of influenza subtypes, protein toxins, tumor markers and other analytes.[145] A list of examples of multiplexed LFA tests for infectious diseases is summarized in other report.[139]

Alternatively, recombinase polymerase amplification (RPA) has been combined with a typical LFA layout to address the issues of rapid multiplexing for virus detection, reducing the LoD, and increasing specificity.[138] RPA can be used for rapid amplification of double-stranded DNA, single-stranded DNA, methylated DNA, cDNA generated through reverse transcription of RNA or miRNA.[147] Ivanov *et al.* demonstrated a RPA multiplex assay and considerations for housing different test zones on one test strip.[138,148] The group developed an approach using three single-strand DNA (ssDNA) modules. Each synthesized amplicon label selectively recognizes one of three potato RNA viruses (PVY, PVS, and PLRV), with the other end featuring a universal fluorescein label. The first module includes oligonucleotide probes with a forward primer for RPA, C9 spacers, and a ssDNA barcode for the test zone. Target RNA viruses are amplified in RPA with reverse transcription. The second module contains anti-barcodes in separate test zones. AuNPs conjugated with antibodies to anti-fluorescein serve as reporter nanoparticles. The third module, anti-primer ssDNA, is crucial for blocking nonspecific reactions and preventing false positives involving the forward primer. The multiplexed assay detected at least 4 ng of PVY per g of plant leaves and 0.04 ng/g for PVS and PLRV within 30 minutes.[138]

A recent active area for LFA development aims to improve sensitivity and generate quantitative results. For example, gold nanoshells gain more interest in enhancing the LFA sensitivity compared to the traditionally used 40-nm AuNPs, as each nanoshell exhibits 30 times stronger immobilized coloration. In addition, the LFA development involves combining traditional arrangements with other analytical methods, as well as utilizing specialized readers and machine learning to enhance the signal and provide a more accurate readout. While this review focused on colorimetric testing without the need for specialized training and laboratory equipment, the advent of newer hand-held devices opens avenues for deploying various analytical methods in the field with minimal required training.[142,149,150] On the other hand, Citterio *et al.* developed a combination of an LFA arrangement with inkjet printing of the capture or test lines, with customizable threshold concentrations, to provide a "text" semi-quantitative readout, corresponding to a trace, low, medium and high concentration (Fig. 11).

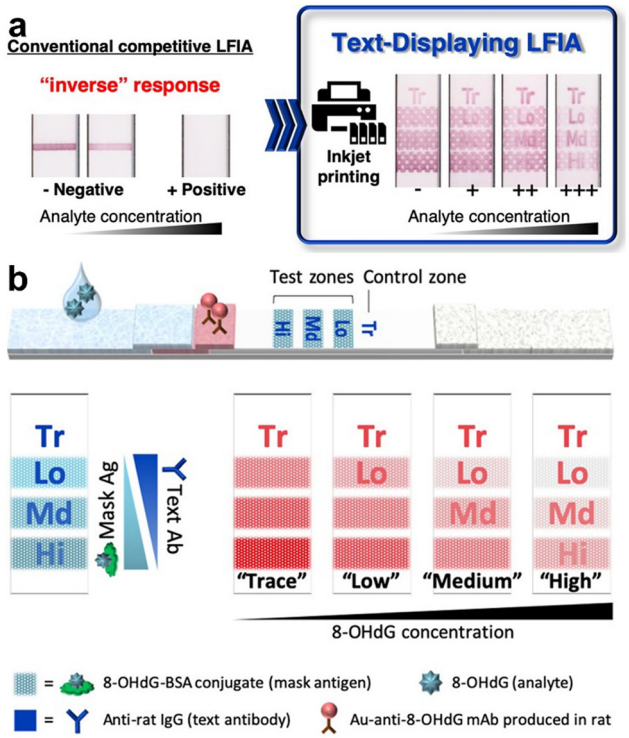

Fig. 11 Semi-quantitative LFA. (a) A traditional readout (left) for a competition type LFA, and a semi-quantitative text readout (right) enabled by inkjet printing using customizable threshold concentrations.[151] (b) Semiquantitative text-displaying LFA strip featuring multiple test zones (Hi, Md, Lo) and a control zone (Tr) for detecting 8-OHdG, with an accompanying schematic of the readout system.[151] Reproduced with permission from ref. 151. Copyright 2020 American Chemical Society.

4.2 Microfluidic paper-based analytical devices (μPADs)

4.2.1 Mechanism of Action. Microfluidic paper-based analytical devices (μPADs) are created *via* patterning paper sheets into multiple hydrophilic microchannels bounded by hydrophobic walls.[152,153] μPADs hold significant promise in spatial multiplexing POC diagnostics. Their appeal also lies in low cost, portability, high throughput, and minimal sample volume requirements. In particular, colorimetric μPADs are esteemed for their simplicity and straightforward visual interpretation. The color transduction mechanisms in μPADs depends on the analytes and embedded enzymatic assays, redox indicators, and NP aggregation.[154] The first reaction integrated with μPADs was a coupled enzymatic assay and used peroxidase or oxidase enzymes along with redox indicators.[155] Below we briefly introduce colorimetric μPADs for sensing analytes such as ions, small molecules, and biopolymers.

4.2.2 Applications. The development of on-site μPADs for ion detection, such as Hg^{2+} and I^-, is of considerable health and environmental interest. Chen *et al.* developed a competitive mechanism μPADs by coating the paper with a tetrahedral DNA nanostructure with an aptamer.[156] The aptamer has a high affinity for Hg^{2+}. In the absence of Hg^{2+}, the biotinylated aptamer binds to streptavidin-labeled HRP, resulting in a color change with TMB-H_2O_2. In the presence of Hg^{2+}, the aptamer prefers Hg^{2+}, reducing HRP binding sites and the color signal. This approach offers linear, smartphone-based color monitoring for rapid and sensitive Hg^{2+} analysis. Iodine (I^-) is critical for neurological activity and thyroid gland function.[157] POC monitoring I^- levels is essential for health management and dietary intake. Xianyu *et al.* developed an etching mechanism based μPADs by immobilizing gold nanostars onto daily substrates, such as clothing fabric and kitchen paper, using an immersing technique.[158] The plasmonic gold nanostars enable a color change in response to iodide surface etching. This μPAD offers qualitative I^- detection with the naked eye and quantitative measurement through smartphone-based RGB value calculation. The paper strip can also be used for sensing other analytes through iodine-mediated reactions. For instance, it can detect the concentration of ascorbic acid in juice, as ascorbic acid reacts with iodate to form iodide (Fig. 12a).

On-site μPADs for measuring glucose is important for achieving personalized diabetic management.[164] A bienzymatic μPAD was constructed by combining glucose oxidase (GOx) and horseradish peroxidase (HRP) with 2,4,6-tribromo-3-hydroxy benzoic acid for the visual detection of glucose levels in saliva samples. Upon scanning with an office scanner, quantitative analysis revealed a detection limit of 0.37 mg dL^{-1}.[162] The use of peroxidase for quantitative glucose determination could be substituted with an artificial nanozyme.[163] Sonkusale *et al.* fabricated enzyme-free μPADs for glucose colorimetric readout.[165] Glucose oxidase-mimicking AuNPs oxidize glucose, producing hydrogen peroxide that etches AgNPs, causing a color change. Smartphone app monitoring offers a linear detection range of 0.5 to 10 mmol L^{-1}, which falls into the clinically relevant range. Additional color mechanisms for glucose detection are referenced in Section 6.2.

Colorimetric μPADs for DNA analysis use complementary pairing and plasmonic coupling mechanisms. Henry *et al.* constructed multiplex DNA/RNA μPADs using a wax-printing technique. They integrated silver nanoparticles functionalized with conformationally constrained pyrrolidinyl peptide nucleic acids (acpcPNA).[159] The acpcPNA selectively binds to specific DNA sequences with high affinity, causing nanoparticle aggregation and color change. This setup allows for the detection of bacterial and viral infections with detection limits of 1.53 nM for MERS-CoV, 1.27 nM for MTB, and 1.03 nM for HPV (Fig. 12b). The same group also developed a multifunctional μPAD using chromogenic nitrocefin as a competitor in reaction with β-lactamase to detect the active ingredient in β-lactams antibiotics (Fig. 12c).[160] The retained yellow color indicates legitimate drugs, while a red color indicates falsified drugs. Additionally, a pH indicator was integrated into the μPAD to identify common falsified ingredients, demonstrating the potential of this approach as a global falsified drug monitoring tool.

4.2.3 Strengths, limitations and developments. Spatially multiplexed μPADs allow the simultaneous detection of various analytes on a single test by integrating multiple functionalities through combined horizontal and vertical fluid flows. Pyun *et al.* created a three dimensional μPAD by printing a detection zone with HRP and respective oxidase and a reservoir on paper, and further superimposed a parylene C-coated plasma separation

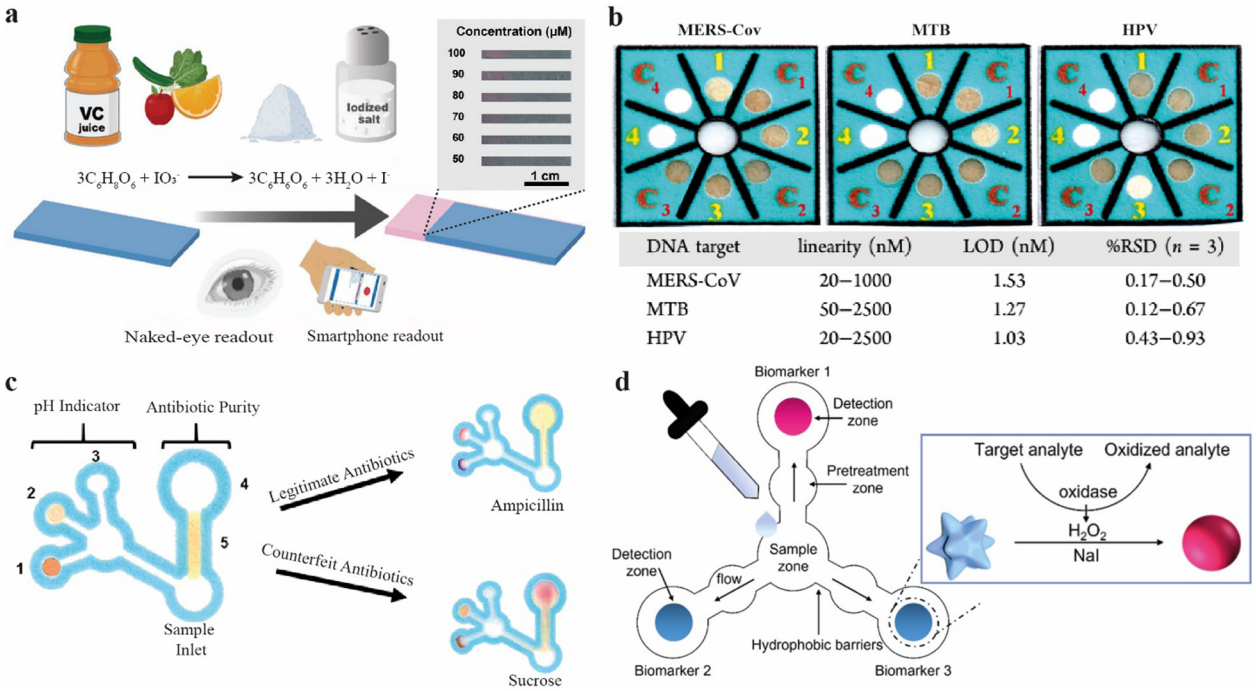

Fig. 12 Microfluidic paper-based analytical devices (μPADs) with colorimetric reporter. (a) POC μPADs for detections of iodate and ascorbic acid, representative color change in presence of different concentration of ascorbic acid was shown.[158] (b) Paper-based colorimetric DNA sensor for detecting viral or bacterial oligonucleotide, the color change, concentration linearity and LOD for detecting MERS-Cov, MTB and HPV were presented.[159] (c) Paper-based enzymatic competition device for differentiating legitimate and counterfeit antibiotics.[160] (d) Simultaneous detection of three salivary biomarkers using monolithic paper-based device.[161] (a) Reproduced with permission from ref. 158. Copyright 2023 Wiley. (b) Reproduced from ref. 159 in accordance with CC BY-NC 4.0. Copyright 2017 American Chemical Society. (c) Reproduced from ref. 160 in accordance with CC BY-NC 4.0. Copyright 2018 American Chemical Society. (d) Reproduced from ref. 161 in accordance with CC BY 4.0. Copyright 2021 MDPI.

membrane on top. This approach enabled the simultaneous detection of multiple metabolic disease markers, including glucose, cholesterol, and triglycerides, using whole blood without separation.[166] Pompa *et al.* developed a μPAD system using blue colloidal branched Au nanostructures and respective oxidases [*i.e.*, cholesterol oxidase (ChOx), GOx, and lactate oxidase (LOx)] to achieve multiplexed sensing of glucose, cholesterol, and lactate in saliva (Fig. 12d).[161] The system utilizes H_2O_2-mediated reshaping of gold nanostructures in the presence of halogen, which results in a blue-to-pink color change. Response readout can be achieved within 10 minutes, demonstrating the potential of this prototype kit for point-of-care testing. Despite of the advantages of massive printing fabrication and spatial-resolved multi-analysis, the primary drawback of μPADs stems from the inherent variability of paper, leading to the introduction of indeterminate errors in any application utilizing these devices.[167] Overall, μPADs have established a strong foundation over the past decade, with versatile recognition methods supporting multiplex functions. In the future, μPADs are expected to adapt advanced fabrication methods and serve as portable platforms for high-throughput screening and diagnosis.

4.3 Wearable sensing devices

Wearable sensing devices are real-time, non-invasive POC tools for monitoring biophysical parameters (*e.g.*, temperature and humidity), biochemical markers (*e.g.*, metabolites, electrolytes, and hormones), and kinematic data (*e.g.*, movement and heart rate).[168,169] Numerous wearable devices, such as wristwatches, headsets, belts, and fitness bands, often suffer from rigidity and dependence on complex analysis tools and external power sources. Colorimetric modality offers an alternative solution by converting physiological or biochemical information into visible color changes, making wearable sensing simpler for individuals. Moreover, the easy and cost-effective integration of colorants onto adhesive substrates enhances the effectiveness of health monitoring.

4.3.1 Applications. Wearable temperature sensors are invaluable during pandemics for fever detection alarms and health management. A wristband from the Wang group is an affordable and sensitive fever screening solution: It is made with a thermoresponsive polymer, P(NIPAM-*co*-AM), which exhibits a significant transmittance drop, from about 70.5% to 17.5%, as the temperature increases from 37.2 to 37.4 °C. This transmittance change is coupled with visible change from transparent to opaque white.[170] By varying the NIPAM to AM monomer ratio, the temperature alert threshold can be further tailored to monitor different health conditions, like hyperthermia and hyperpyrexia. The next-generation wearable sensors aim to monitor more than one piece of health information. Dong *et al.* created a wearable device for simultaneous temperature and strain monitoring. They achieved this by programming a thermochromic elastomer prepolymer and a conductive hydrogel

precursor to form core–shell segmental fibers using a straightforward wet-spinning method.[171] The device features a sharp color change due to incorporation of thermochromic elastomer and thermochromic microcapsules. It can be fabricated with tunable lengths, making it a flexible wearable device for monitoring body motion and temperature for improved health management. Enhancing the sustainability of wearable colorimetric sensing techniques could drive their advancement. Hybrid hydrogels with self-healing properties and environmental responsiveness offer significant potential for the development of smart wearable devices. For example, Chen *et al.* developed a hybrid hydrogel by incorporating commercially available thermochromic and photochromic dye microcapsules into branched polyacrylate, which was further complexed with zinc sulfate through multi-hydrogen bonds and ionic bonds.[172] This hybrid hydrogel exhibited rapid color changes when exposed to thermal or UV stimuli due to synergistic effect of color-changing microcapsules and polyacrylate, enabling effective human health monitoring and achieving adaptive camouflage. Furthermore, hydrogel's self-healing capabilities make it highly promising for long-term body monitoring.

Humidity indicates skin hydration and environmental moisture levels and is frequently measured by wearable devices. It is generally associated with skin diagnosis and thus health management. Wang *et al.* devised a one-step sputtering technique to create silver nanowire clusters on a disordered anodic alumina oxide (DAAO) substrate.[173] This simple method enables the easy creation of wearables like bracelets and bags. Plasmon coupling in nanowire clusters enhances the electric field significantly, increasing refractive index sensitivity and causing distinct extinction spectra changes in the presence of water. By combining a cholesteric main-chain polymer with a hygroscopic poly(ampholyte), Haan *et al.* achieved an elastic cholesteric polymeric material that exhibits responsive behavior to both strain and humidity.[174] They fabricated a bilayer film that changes color with strain and humidity: When wet, it shifts from green to yellow, and stretching shifts it from green to blue.

Sweat is rich in physiological information including electrolytes and metabolites. Sweat analysis is an important format for wearable sensors in health management. Rogers *et al.* advanced wearable colorimetric sensors by developing a soft, skin-integrated microfluidic system capable of real-time monitoring of sweat rate and multiple biomarkers, including chloride, glucose, and lactate (Fig. 13a).[175] The microfluidic system integrates colored dye references directly onto the platforms, allowing for quantitative analysis using digital imaging techniques through a smartphone. The same group also designed a sweat sticker with an integrated colorimetric chloride assay to measure the concentration of chloride in sweat. This approach serves as a robust biomarker for confirming the diagnosis of cystic fibrosis for children outside of clinical settings.[176] Dong *et al.* achieved recyclability and flexibility in sensing devices by directly printing thermochromic, photochromic, and pH-chromic inks onto a sustainable starch support.[177] The devices monitored multiple parameters, including UV intensity (0–2500 μW cm^{-2}), temperature (0–38 °C), and pH (4.0–7.0), translating them into distinct RGB values for simple data interpretation. The Bandodkar group achieved the function of on-demand and longitudinal sweat analysis in a wearable microfluidic system using finger-actuated pumps and valves.[178] This innovative device allows for longitudinal analysis of multiple analytes in sweat to reflect specific health conditions, and condition-specific analysis can be achieved *via* embedding desired assays in different sensing chamber (Fig. 13b). It incorporates colorimetric calibration for physiological parameters, including chloride, calcium, glucose, and urea. Quantitative analysis, based on imaging analysis of RGB values, provides accurate measurements of these physiological markers.

Interstitial fluid (ISF) connects capillaries and tissue cells, hence contains similar metabolites as in blood.[179] ISF is also readily accessible and less invasive, offering great potential to

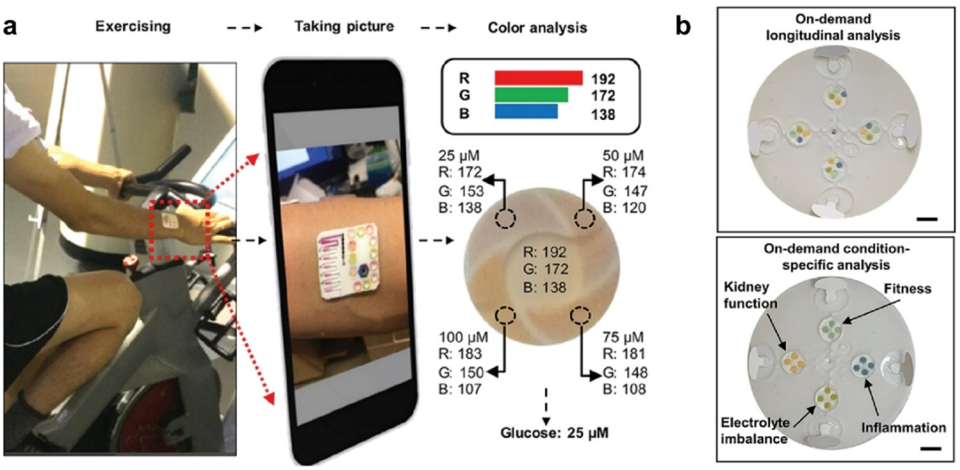

Fig. 13 Wearable colorimetric sensing devices. (a) Multifunctional sensing devices used in sweat collecting and colorimetric analysis.[175] (b) Wearable microfluidic patch for on-demand longitudinal and condition-specific analysis.[178] Four different analyte assays were embedded in one chamber and each chamber can be tested at one specific time point to achieve longitudinal analysis while an array of one specific analyte assay was embedded in each chamber to achieve condition-specific analysis. (a) Reproduced with permission from ref. 175. Copyright 2019 American Chemical Society. (b) Reproduced with permission from ref. 178. Copyright 2022 American Chemical Society.

monitor health-related biomarkers. Xu *et al.* developed a swellable microneedle (MN) patch using methacrylated hyaluronic acid that were able to rapidly extract ISF.[180] The extracted ISF metabolites was efficiently recovered *via* centrifugation, and levels of glucose and cholesterol were determined using colorimetric method, demonstrating the effective and minimally invasive ISF sampling and detection. To enhance wearable comfort, Xu *et al.* fabricated colorimetric dermal tattoo biosensor using a four-area segmented MN patch and demonstrated multiplexed detection of health-related biomarkers such as pH, glucose, uric acid and temperature.[181] The color changes in response to concentration of biomarkers provide effective health monitoring over 4 days, showing potential for long-term usage without complicated devices. Want *et al.* also explored wearable MN-based colorimetric patch for real time uric acid (UA) analysis. Uricase can catalyze oxidation of UA sampled from ISF to produce H_2O_2, which was further reacted with TMB in presence of polypyrrole nanoparticles with peroxidase-like activity.[182] The color variation can be observed *via* naked eyes or quantified using a smart phone, offering potential to monitor UA levels, and hence can possibly be one health management technique for patients with gout.

4.3.2 Strengths, limitations and developments. Wearable colorimetric sensing devices have garnered growing research interest owing to their non-invasive characteristics, personalized monitoring capabilities, and direct visual output. These devices have found successful applications in biomarker sensing, as discussed earlier. Furthermore, ongoing studies are investigating their potential integration into daily accessories like face coverings and diapers, thereby broadening the scope of health monitoring applications including pandemic surveillance.[183,184] Despite the advantages of cost-effectiveness, flexibility, and spatial multiplexing, wearable colorimetric sensing devices face several challenges. These include the need to enhance adhesion for long-term monitoring, design of durable bio-material interface, improve the effectiveness and ease of biofluid extraction/collection to facilitate measurements, eliminate sources of contamination, and enhance detection sensitivity for accurate measurements.[168,185]

5. Colorimetric sensor-array systems

A sensor array employs a sensing strategy akin to a "chemical-nose" or "chemical-tongue" and achieves this through the utilization of synthetic molecules and materials that emulate the human olfactory system. It distinguishes itself from specific sensors by not conforming to the lock-and-key mechanism (Section 6). Instead, sensor arrays depend on the selective binding of an analyte to a cross-reactive array of receptors, leading to the generation of a distinct response pattern (Fig. 14). This pattern can subsequently be deciphered and associated with a specific analyte through pattern recognition.

Sensor arrays demonstrate outstanding capabilities in detecting unknown analytes, thus accommodating a wide range of analyte inputs, and effectively dealing with interference from analog compounds and complex sample compositions. They achieve this without the need for screening and modifying recognition elements, as each analyte produces a unique pattern within the array. The key to the sensor array is the simultaneous interactions of multiple analytes with multiple receptors, resulting in the generation of specific response patterns. These patterns are sensitive to the overall changes in complex mixtures, making the sensor-array approach particularly robust for sensing complex biological matrices and enabling the identification of subtle variations within these intricate mixtures. Colorimetric sensors-array have been exploited for the detection of explosives[186,187] and VOC,[188,189] environmental monitoring,[190–192] healthcare.[193,194] We discuss the mechanisms of sensor arrays, the analysis of color signal patterns, and their representative applications for detecting metal ions, small molecules, biomolecules, cells or pathology conditions.

5.1 Sensor-array design

Chemical-nose sensor design includes multiple recognition events, signal transductions, and a unique step-pattern recognition through statistical analysis. Recognition elements interact with multiple analytes, resulting in cross-reactivity among receptors. The recognitions generate individual signals (colorimetric, fluorometric, electric, *etc.*), which are aggregated and analyzed

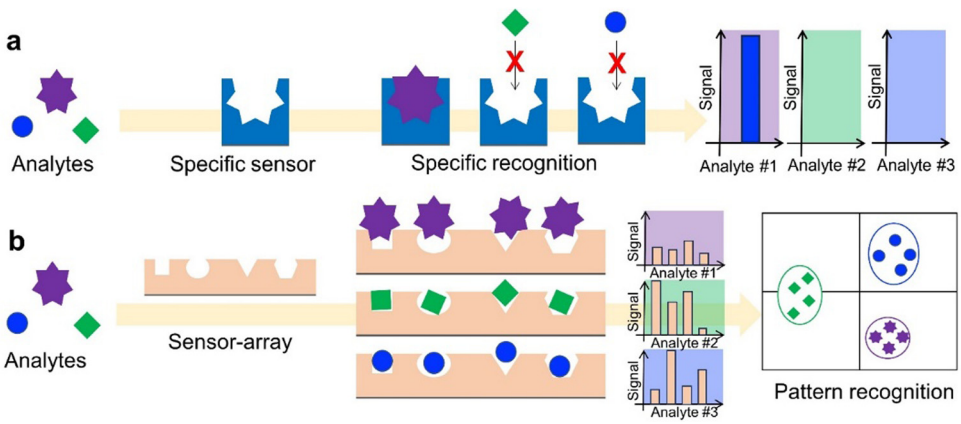

Fig. 14 Illustration of a specific sensor *versus* a sensor-array. (a) Specific sensors designed for individual analytes based on a lock-key mechanism. (b) A sensor-array composed of multiple cross-reactive and non-specific receptors can interact with multiple analytes: Each analyte is discriminated *via* a unique pattern recognition.

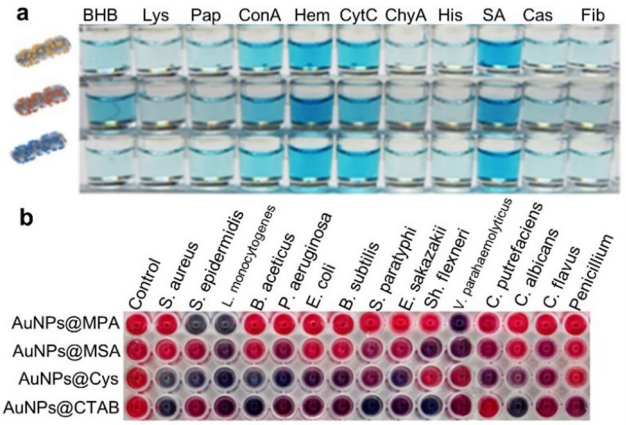

Fig. 15 (a) Catalytic activity of metal-nanoparticle-supported nanozymes in the presence of various proteins.[195] (b) Color change of suspension of the ligated AuNPs after addition of microorganisms.[196] (a) Reproduced with permission from ref. 195. Copyright 2022 American Chemical Society. (b) Reproduced with permission from ref. 196. Copyright 2017 American Chemical Society.

using statistical techniques for pattern identification and result classification. In this review, we focus on sensor-array generating colorimetric responses where the presence of the analyte provokes color changes (or not) of each channel of the sensor array which can be interpreted by the naked eyes or with spectroscopy methods. As an example, Fig. 15 shows two colorimetric sensor-arrays for the detection of proteins or microorganisms using metal-NP-supported nanozymes catalytic activity[195] or AuNPs aggregation,[196] respectively. In both cases, a specific colorimetric pattern could be observed by the naked eye for each analyte. In this section, we describe the design of a colorimetric sensor-array, including the recognition event, the signal transduction, and the statistical analysis.

5.1.1 Recognition event. Specific recognitions are primarily used in lock-and-key sensors. However, they can also be integrated as one of the receptors in sensor arrays. Sensor arrays achieve optimized resolution through numerous cross-reactive receptors. These receptors of varying properties interact with a range of analytes, distinguishing them based on binding affinities. The collective responses of these receptors with the analytes create a unique fingerprint pattern. Receptors can be either conjugated to the transducer or can transduce the signal by themselves. For example, pH-dependent[197] or redox-sensitive[198] dyes have been used in colorimetric sensor-array as well as chemoresponsive dyes.[199] In these cases, the receptors undergo color changes due to intermolecular interactions with the analyte, serving as both a recognition element and transducer. Some applications require complex receptors that cannot transmit optical signals and need additional colorants. The employed receptors encompass small molecules,[200] amino acids,[201] polymers,[202,203] DNA,[204,205] or peptides,[20] each with its unique set of advantages and limitations. The selection among these receptors depends on the specific application requirements and their compatibility with the desired transducer.

5.1.2 Signal transduction. The sensor-array recognition event can be transduced through various methods, including colorimetric, fluorometric,[13] Raman,[206] chiral,[207] IR spectroscopies,[208] and electrochemical read-outs.[209] In this context, our primary emphasis is exclusively directed towards colorimetric transduction perceptible to naked eye. This approach incorporates colorants including dyes and plasmonic nanoparticles. Generally, sensor array design conventions streamline their approach by employing a single type of colorant reporter alongside varying receptors. This simplification eases the complexity of potential interactions and pattern classification. Consequently, colorants capable of generating an extensive spectrum of hues are highly desirable for array applications, thereby maximizing the conveyance of information regarding receptor binding events in sensor arrays.

5.1.3 Statistical methods for pattern analysis. Cross-reactivity sensor arrays produce complex colorimetric patterns that cannot be directly interpreted. Data processing is thus necessary to classify and associate these patterns with specific conditions or categories, such as pathology stage, media composition, or cell lines, *etc.* The goal is to condense sensor-array data to differentiate patterns and to link these from unknown samples and to these of a known class. This subsection covers three common statistical methods: hierarchical cluster analysis (HCA), principal component analysis (PCA), and linear discriminant analysis (LDA).[13] These techniques employ unsupervised learning (PCA and HCA) to discover discriminative patterns or naturally clustered data, or supervised learning (LDA) using a known sample training dataset to test unknown samples.

Hierarchical cluster analysis (HCA). HCA is an unsupervised method that groups data points by pairing them with their nearest neighbors to create clusters. These clusters are then connected to neighboring clusters, forming larger ones, and so on.[210] This iterative process ultimately results in the formation of a dendrogram. This dendrogram serves to visually represent the connectivity and distance between all pairs of data points or clusters. In a chemical analysis, the connectivity and distance are important to determine the similarity between two samples and the magnitude of their similarity, respectively. Janzen *et al.* developed a robust sensor array utilizing chemoresponsive dyes for VOC identification: HCA facilitated the classification of more than a hundred closely related VOCs.[61] Overall, HCA is a convenient tool for semi-quantitatively assessing similarities between data. HCA methods have three main limitations: (i) as an unsupervised method, it is not predictive; (ii) when a new object is added, the dendrogram has to be re-created, and comparing dendrograms can only be done qualitatively; (iii) mis-clustering of noisy data can be easily misinterpreted.

Principal component analysis (PCA). PCA is an unsupervised method that reduces the dimensions of the data sets without significant loss of information. It uses linear combination of the initial dimensions to create a new orthogonal set of dimensions.[211] New dimensions, or components, are ranked by variance, with the first component describing the highest variance and the second the second-highest, and so on. This results in a new coordinate system, where the first axis is the

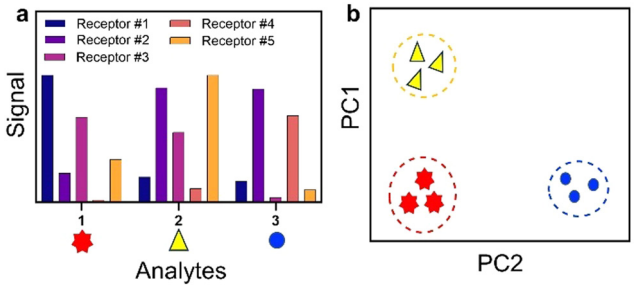

Fig. 16 Schematic representation of a fingerprint response of three analytes with a sensor-array composed of 5 receptors (a) and its simplification *via* principal component analysis (b).

first principal component (PC1), orthogonal to the second axis, PC2. Typically, the number of dimensions is chosen to capture 95% of the variance. The resulting plot of these two principal components is often easier to interpret than the original dataset. It allows for spatial separation in the testing of one sample cluster from the testing of another analyte, aiding in multiple testing (Fig. 16). PCA, like HCA, is primarily for classifying data, not predicting. Yet, if two key components offer clear class separation, PCA can be used for basic predictions of unknown samples.

Linear discriminant analysis (LDA). LDA is a supervised technique that transforms the original dataset into a new orthogonal set of dimensions. The objective of LDA is to identify dimensions that effectively separate the data into known classes. The resulting dimensions are called discriminant factors and are computed to maximize the ratio of between-classes to within-classes variations, essentially enhancing the signal-to-noise ratio.[212] Unlike PCA, LDA uses a training dataset to classify unknown samples into the correct classes and thus can distinguish various analytes within sample classes (Fig. 17a and b). For example, Li *et al.* developed a sensor-array based on the aggregation of AuNPs with different surface charges for the discrimination of microorganisms.[196] With a four-channel sensor, they could distinguish correctly 15 pathogens using LDA analysis (Fig. 17c and d).

The primary limitation of LDA is its sensitivity to sample size. Unlike other statistical methods, LDA considers sample class covariance, making it unstable when the sample size is smaller than the number of sample classes, especially in high-dimensional datasets. Consequently, LDA yields fluctuating results with small sample sizes compared to PCA and HCA.

5.2 Sensor-array applications

5.2.1 Metal ions. Heavy metal ions (*e.g.*, Cd^{2+}, Hg^{2+}, Pb^{2+}, Cr^{3+}) in food, water, and soil pose health and environmental risks, necessitating sensitive sensor-arrays monitoring. For example, Sener *et al.* developed the first colorimetric sensor arrays using mercaptoundecanoic acid (MUA)-capped AuNPs and five amino acids to detect toxic metal ions (Hg^{2+}, Cd^{2+}, Fe^{3+}, Pb^{2+}, Al^{3+}, Cu^{2+}, and Cr^{3+}).[214] Amino acids influence the colloidal stability of MUA-capped AuNPs in the presence of metal ions, either preventing or promoting AuNP aggregation,

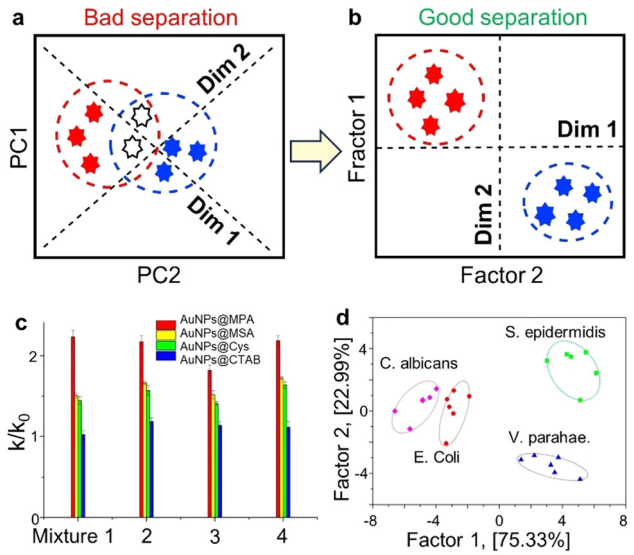

Fig. 17 Comparing score plots by using PCA (a) and LDA (b). Dimension 1 allows the most obvious separation by eyes in the PCA plot and is used as the first dimension in the LDA analysis and is a representation of the between-sample variance. The two color-less analytes are thus associated to the correct class using LDA while their identification was ambiguous with PCA.[213] (c) Response (k/k_0) patterns in the presence of the microorganisms. Mixtures 1–4 represent (*L. monocytogenes* + *C. albicans*), (*L. monocytogenes* + *E. coli*), (*L. monocytogenes* + *V. parahemolyticus*), and (*L. monocytogenes* + *S. epidermidis*) suspensions, respectively. (d) Canonical score plot for the response patterns as obtained from LDA.[196] (a) and (b) Reproduced from ref. 213 (2020) in accordance with CC BY-NC 3.0 with permission from the Royal Society of Chemistry. (c) and (d) Reproduced with permission from ref. 196. Copyright 2017 American Chemical Society.

resulting in a color change from red to blue (Fig. 18a). Combining color changes in amino acid channels allows unique colorimetric responses for each metal ion (Fig. 18b). HCA analysis distinguishes the seven heavy metal ions over a wide concentration range (Fig. 18c). Nevertheless, the detection limit was 2 μM, above the necessary detection limit for real samples in the low nM range (Fig. 18d).

Since then, several methods have been reported in the literature to improve the limit of detection. For example, He *et al.* developed a colorimetric sensor-array based on the binding competition of urease and several thiolate molecules for heavy metal ions (Ag^{+}, Ni^{2+}, Cd^{2+}, Hg^{2+}, Pb^{2+},Mn^{2+}, Cu^{2+}, Co^{2+}, Zn^{2+}, Fe^{3+}, Sn^{4+}).[197] The three cross-reactive receptors used, glutathione reduced (GSH), cysteine (Cys) and mercaptoethanol (MCE), have all different abilities to bind the metal ions compared to urease. Urease, when not binding to metal ions, decomposes urea into ammonia, altering the solution's pH, observable with bromothymol blue as a pH indicator. Each metal elicits a distinct colorimetric response, enabling pattern recognition and classification using LDA and HCA. This method is rapid (within 30 seconds), sensitive, and visually discriminates metal ions. Discrimination among the 11 metal ions is achieved through color changes in the three channels such as GSH, Cys, and MCE (Fig. 19a–c). LDA was used to convert the colorimetric response into identifiable recognition

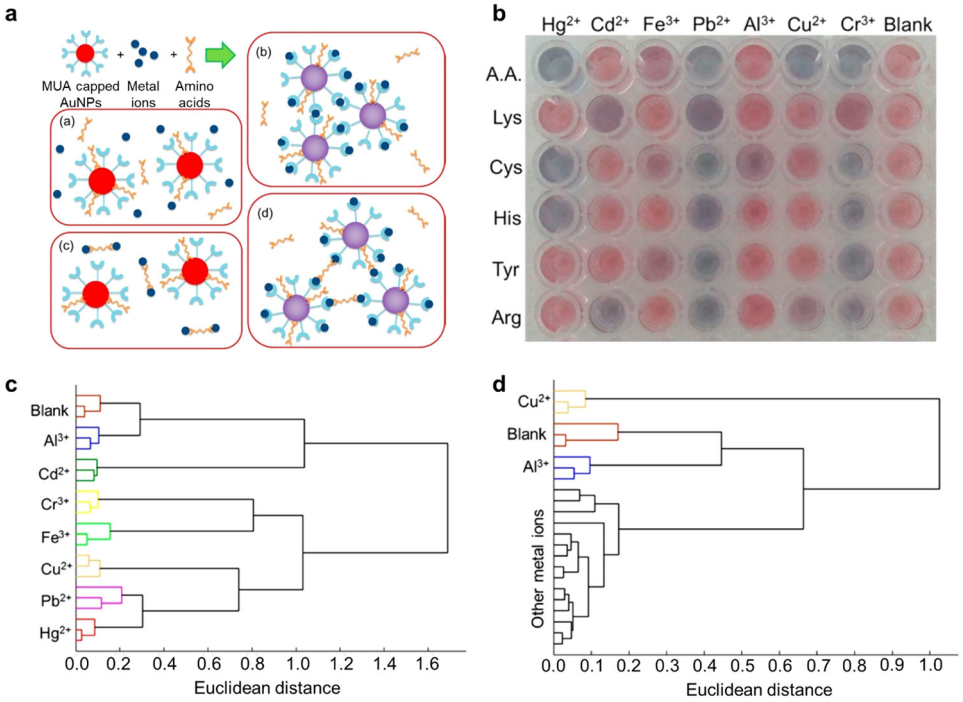

Fig. 18 (a) Schematic representation of metal ions, amino acids and AuNPs interactions: No interactions, metal ions induce the aggregation of AuNPs, amino acids interact with metal ions and prevent the aggregation of AuNPs, and metal ions and amino acids co-contribute to the aggregation of AuNPs. (b) Representative photograph of the colorimetric sensor array response against 20 μM of metal ions (c) and (d) Hierarchical cluster analysis of colorimetric sensor array of seven different metal ions at different metal ion concentrations: (c) 20 and (d) 2 μM.[214] Reproduced with permission from ref. 214. Copyright 2014 American Chemical Society.

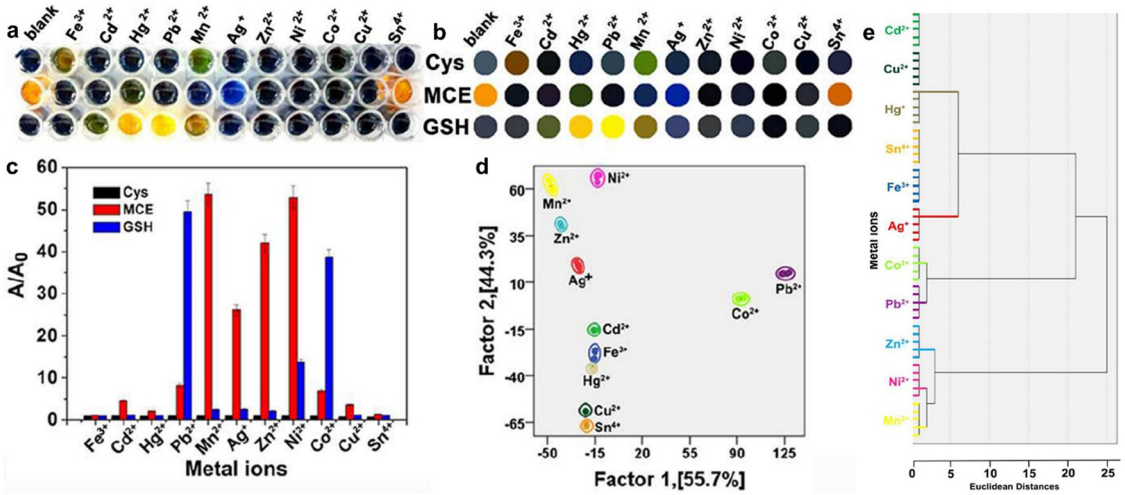

Fig. 19 (a) Thiols act as receptors in a colorimetric sensor array, thus distinguishing heavy metal ions with unique color change patterns at 10 nM. (b) Color map corresponding to (a). (c) Fingerprints of the 11 metal ions at 10 nM based on the patterns of the corresponding values of A/A_0 obtained from the colorimetric responses of the sensor array. (d) Canonical score plot for the first two factors of colorimetric signal patterns analyzed by LDA (five parallel measurements). (e) HCA plot for discriminating 11 metal ions (all at 10 nM) based on the colorimetric signal changes of the sensor array.[197] Reproduced with permission from ref. 197. Copyright 2018 American Chemical Society.

patterns and the discrimination of the metal ions could be performed for concentrations as low as 5 nM (Fig. 19d). Different concentrations of the same metal ion could also be discriminated with a limit of detection of 2.29 nM which is to date the best LoD reported for such system. The discrimination of metal ions was successfully supported by hierarchical clusters analysis (Fig. 22e). Control metal ions were used (K^+, Na^+, Mg^{2+}, Al^{3+}, Ca^{2+}, and Fe^{2+}) and no interferences with the classification of the heavy metal ions was observed. The sensor array was applied to tap water spiked with heavy metal ions, achieving 100% classification accuracy.

5.2.2 Proteins. High-throughput detection of proteins is crucial for proteomics and screening protein biomarkers in various disease samples. Current methods involve mass spectrometry and immunoassays are specific but not suitable for high-throughput protein measurement.[215] Detecting proteins in biofluids like serum is challenging due to the naturally high concentration (mM) of over 20 000 different proteins. Lu *et al.* reported a sensor-array for protein sensing using programmable metal-NP-supported nanozymes as artificial receptors. (Fig. 20a).[195] The *in-situ* reduction of various metal salts on assembly of molybdenum disulfide (MoS_2) and polypyrrole (PPy), PPy@MoS_2, was used as encoder as it generated differential nonspecific interactions with bioanalytes such as proteins. The sensor-array was composed of three channels each one using a specific type of nanoparticles, *e.g.*, Au, Ag and Pd NPs. The decoration of metal NPs could modulate the catalytic properties of PPy@MoS_2 nanocomposites. TMB was used to generate a colorimetric signal upon oxidation (Fig. 20b) which was impacted by the interaction NPs-bioanalytes. Using PCA, they could discriminate 11 proteins at a nanomolar concentration as well as complex protein mixtures (Fig. 20c). The identification of proteins in human plasma could also be demonstrated.

NPs-based sensor-arrays are simple and cost-effective and when distinct colorimetric patterns can be obtained, they can even be used for naked-eyes identification of samples. Jokerst *et al.* reported peptide-AgNPs interactions and its use in a sensor-array for the visual identification of viral proteins in external breath condensate or saliva.[20] The study explored the interaction between AgNPs coated with BSPP and peptides containing a bridging motif, which interact with NPs through electrostatic or hydrophobic mechanisms. During assembly, BSPP-AgNPs form fractal structures, altering the LSPR band and causing a visible color change. Protein presence disrupts the peptide-AgNPs interaction, creating a specific color change for detection (Fig. 20d). Nine different peptide sequences were used in the colorimetric sensor-array and allowed the discrimination between nM concentrations of viral proteins, *i.e.*, the main protease (M^{pro}) and the papain-like proteases (PL^{pro}) of SARS-CoV-2 and Neuraminidase (NA) from influenza, and human proteins such as hemoglobin (Hgb), bovine serum albumin (BSA), trypsin (Tps) and pepsin (Pps). LDA detects viral proteins at sub-nanomolar concentrations in breath condensate or saliva and distinguishes them from healthy samples. The array is eye-readable, displaying multiple color changes due to pronounced LSPR band deformation covering the visible spectrum (Fig. 23e). Fig. 20f shows a simplified sensor with three colorimetric channels that effectively distinguish different proteins. The color changes were so unambiguous that 100% accuracy was obtained for a blind study of 50 unknown samples based only on visual identification of the samples.

5.2.3 Cell phenotyping. The cell membrane is a complex structure where subtle changes can describe an alteration of their function. For example, cell phenotyping has been exploited for understanding and treating cancers.[216,217] Direct analysis of cancerous cells possesses obvious advantages compared to the traditional cell lysis-based methods. However, the identification of subtle changes at the cell surface is challenging and there is a clear need to develop an efficient platform for cell phenotyping. AuNPs decorated with DNA can interact

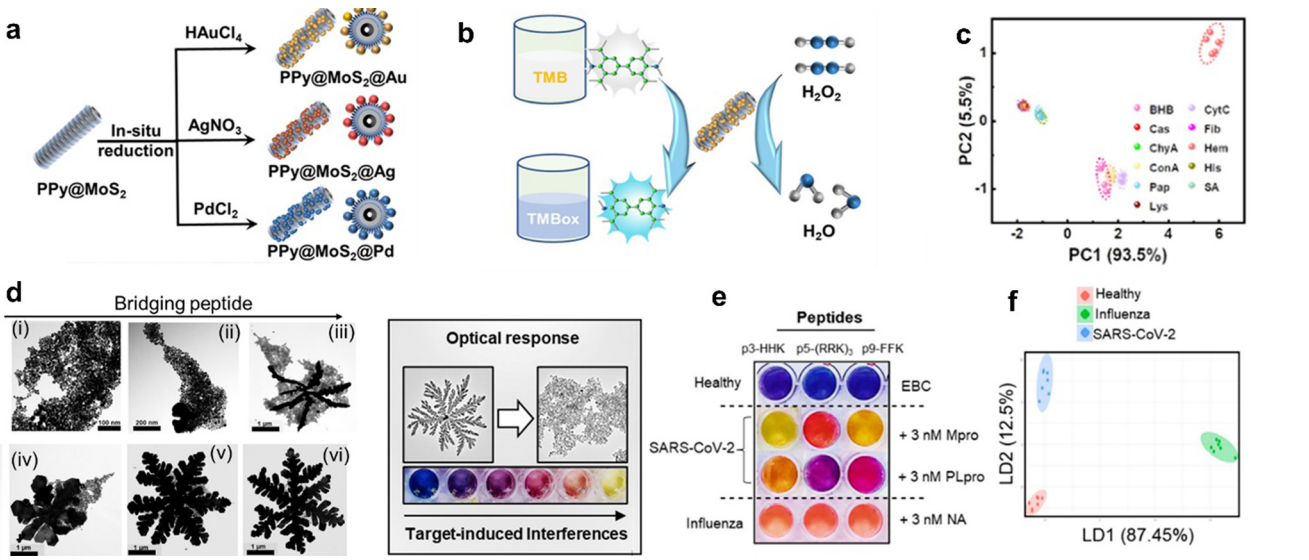

Fig. 20 Modes of sensor response and structural features of NPs. (a) Synthetic process of Au, Ag, and Pd NP-supported PPy@MoS_2 nanocomposites *via in situ* reduction.[195] (b) Catalytic oxidation of TMB by PPy@MoS_2@Au.[195] (c) PCA plot for the discrimination of 250 nM of 11 proteins.[195] (d) Illustration of the sensor-array with the optical response that is proportional to the interference caused by the analyte in the peptide–particles interaction.[20] (e) Canonical score plot for the first two factors of the simplified optical response pattern from the sensor-array obtained by the LDA against 3 nM M^{pro} and PL^{pro} or NA spiked in healthy EBC. Ellipses are 99% of confidence.[20] (f) Simplified picture of the sensor-array against healthy EBC spiked or not with 3 nM M^{pro}, PL^{pro}, or NA.[20] (a)–(c) Reproduced with permission from ref. 195. Copyright 2022 American Chemical Society. (d)–(f) Reprinted with permission from ref. 20. Copyright 2022 American Chemical Society.

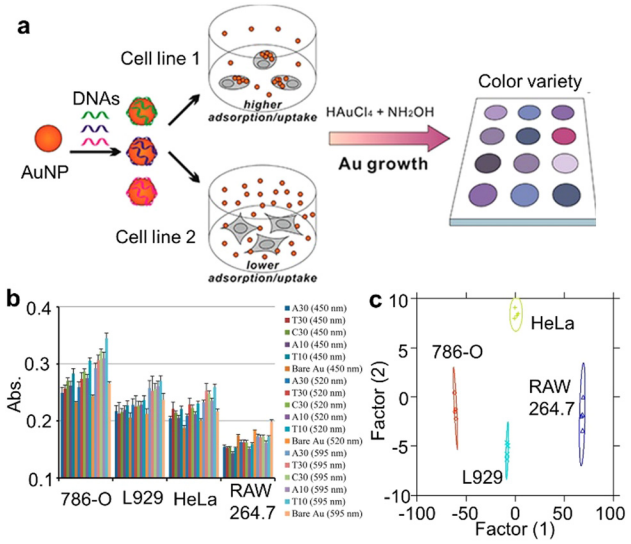

Fig. 21 Sensor-array for cancer cells phenotyping. (a) Illustration of cancer cell lines phenotyping with DNA-modified AuNPs and fingerprint-like colorimetric pattern for four cell lines (768-O, L929, HeLa, and Raw264.7) and (b) and (c) the associated canonical score plot.[218] Reproduced with permission from ref. 218. Copyright 2014 American Chemical Society.

with the cell membrane and be subsequently internalized. By using poly-adenine, poly-cytosine and poly-thymine modified AuNPs, Yang *et al.* found that their internalization is strongly dependent on (i) the length of the DNA strands and (ii) the cell line.[218] A seeds-growth method was then employed to produce a colorimetric signal and LDA analysis could be used to discriminate four different cell lines: 786-O (human kidney carcinoma cell line), L929 (murine aneuploid fibrosarcoma cell line), HeLa (cervical cancer cell line) and RAW264.7 (macrophage cell line) (Fig. 21).

Identifying macrophage polarization states is crucial for drug research, toxicological screening, and immunotherapy. The complexity of macrophage activation poses a challenge for current biomarker-based methods. Geng *et al.* demonstrated a five-channel sensor-array for the rapid (<30 minutes) identification of macrophages polarization.[213] The sensor exploits a polymeric complex between a GFP and a cationic polymer poly(oxanorbornene) containing a pyrene dye molecule resulting into a FRET assembly. The interaction with the macrophage membrane disrupts the fluorescence quenching and a fluorescent response is observed. Different subtypes of bone-marrow macrophages could be discriminated. Using a similar system, Jiang *et al.* could detect macrophage responses in term of membrane surface changes to femtomolar concentrations of common pesticides.[219]

5.2.4 Microorganisms. Detecting microorganisms is one of the keys in medicine and the food industry, with bacterial and fungal infections posing global challenges. Traditional methods including culture and counting, immunological assays, and PCR are time-consuming and costly. Colorimetric sensor arrays offer effective, rapid, and cost-efficient solutions for microorganism identification.

Li *et al.* developed a sensor-array based on AuNPs possessing diverse surface charge for the detection of various microorganism (Fig. 22a).[196] The variation in surface charge impacts the interaction between the AuNPs and the microorganisms, resulting in their dispersion or aggregation. The diverse dispersity of the suspensions provides various colorimetric responses that were analyzed with LDA, allowing the discrimination of 15 microorganisms (Fig. 22b). Moreover, a mixture of microorganisms could be identified. Sensor-arrays based on nanoparticles with similar surface charges have also been developed. Li *et al.* showed that combination of diverse sizes of unmodified AuNPs and AgNPs (only citrate-capped NPs) could be used in a sensor-array for the discrimination of bacteria (Fig. 22c and d).[220] The two presented examples are based on the interaction between nanoparticles and the membrane surface of microorganisms, but alternative concepts can also be explored. For example, Gao *et al.* exploited the metabolism of bacteria to develop a colorimetric sensor-array (Fig. 22e). D-Amino acids decorated AuNPs were used as probes for the discrimination and classification of eight different kinds of bacteria, including multi resistant strains (Fig. 22f).[221]

5.2.5 Pathology. Sensor arrays can identify disease-related chemical signatures in biofluids without specifying a particular analyte, especially through the detection of VOCs in exhaled breath, which can offer insights into various pathologies. For example, Mazzone *et al.* developed a colorimetric sensor-array for the identification of the metabolic biosignature of lung cancers.[222,223] Lung cancer is often asymptomatic and non-specific symptoms delay diagnosis until a late, less treatable stage, highlighting the need for non-invasive and cost-effective testing methods. Thirty-six chemically sensitive dots were utilized and impregnated on a disposable cartridge (Fig. 23a). VOCs in the breath of lung cancer patients create a unique colorimetric pattern distinct from healthy individuals (Fig. 23b–d). Smoking history, demographics, and cancer stage did not impact the results.

Besides lung cancer, exhaled breath metabolites provide information about other kinds of respiratory diseases. For example, Bordbar *et al.* developed a smart mask during the COVID-19 pandemic for the colorimetric detection of SARS-CoV-2 infections.[224] A sensor-array was introduced on a thin face mask and used to detect the exhaled breath metabolites of 130 subjects, distributed in three main groups: healthy, COVID-19 and cured. The sensor was composed of 32 sensing elements ranging from porphyrazines, organic dyes or even modified AuNPs (Fig. 24a–c). The sensor is directly exposed to the exhaled breath stream and interactions between the volatile metabolites and the sensing components occur, providing a unique colorimetric pattern response as a function of the disease state. An accuracy of >80% was reached and a good correlation between the colorimetric response and the disease severity was obtained (Fig. 24d). Furthermore, the participants were divided into the following 5 groups based on their disease severity determined by a pulmonologist. The total responses of the sensor array and each sensing component were quantified. As an example, the intensity of the color of the sensing element S8 was strongly impacted by the disease severity (Fig. 24e).

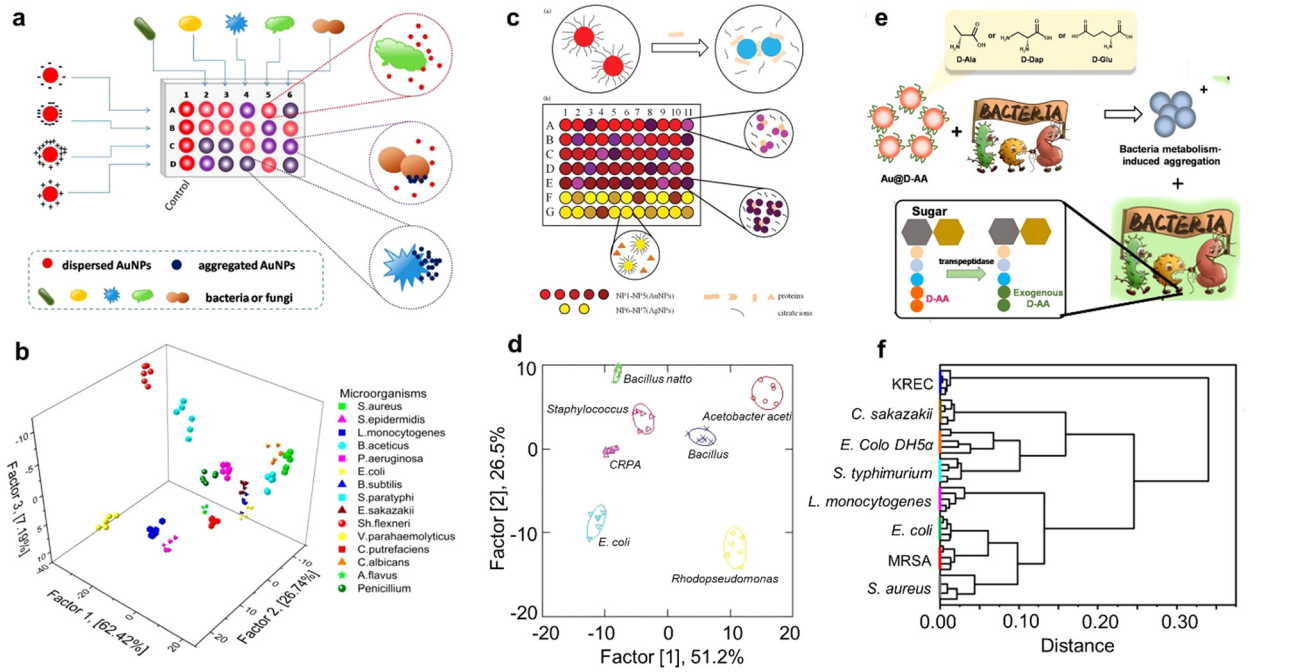

Fig. 22 Sensor-arrays for bacteria sensing. (a) A sensor-array based on AuNPs of diverse surface charge for the detection of various microorganism.[196] (b) The diverse colorimetric responses were analyzed with LDA, allowing the discrimination of 15 microorganisms.[196] (c) and (d) A combination of diverse sizes of unmodified AuNPs and AgNPs was used in a sensor-array for bacteria discrimination.[220] (e) and (f) D-Amino acids decorated AuNPs were used in a sensor-array for discriminating eight different bacteria.[221] (a) and (b) Reproduced with permission from ref. 196. Copyright 2017 American Chemical Society. (c) and (d) Reproduced with permission from ref. 220 (2015) with permission from the Royal Society of Chemistry. (e) and (f) Reprinted with permission from ref. 221. Copyright 2022 American Chemical Society.

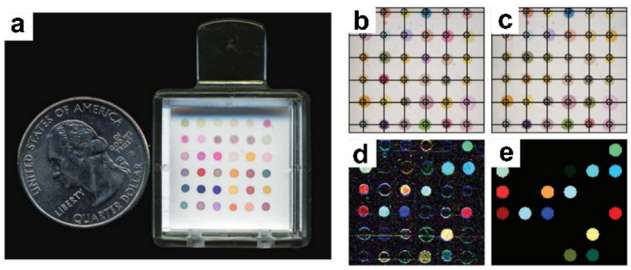

Fig. 23 (a) Sensor-arrays for exhaled breath sensing with a size of coin. The scanner images the sensor array at baseline (b) and after being exposed to a chemical sample such as exhaled breath (c).[222,223] The difference in the colors from time A to B is pictured in panel (d).[222,223] (e) Cleaned-up version of panel (c).[222,223] Reproduced with permission from ref. 222. Copyright 2007 Elsevier.

Similarly, the response of the sensor was determined as a function of the viral load, determined by rRT-PCR analysis and a significant trend could be observed. As an example, Fig. 24f shows the relationship between the color change of the sensing element S15 and the viral load.

5.3 Outlook and limitations

Cross-reactive sensor arrays excel in discerning subtle differences in highly similar complex samples, offering an advantage over specific lock-key sensors that struggle with analytes of similar structures. Numerous examples of rapid and cost-effective colorimetric sensor arrays are provided for the identification of various molecules and conditions, with a primary focus on plasmonic NPs as colorants (Table 7). However, challenges persist in terms of long-term stability, background interferences in real samples, and controlling the density of sensing elements per particle. Addressing these limitations may involve developing highly engineered cross-reactive receptors and ligands to enhance both nanoparticle stability and receptor specificity.

6. Activatable colorimetric systems

An activatable colorimetric system changes color in response to a specific analyte or stimulus. Some studies have delineated activatable system to exclusively address the activity detection, but here we also consider the presence detection.[227] In particular, the recognition component (Section 3.2) recognizes analytes *via* the lock-and-key mechanism, and the transducer component conveys these specific interactions through color changes. The recognition component ensures high selectivity, minimizing non-specific interference. The on/off signals provide substantial contrast, easy readout, and are potentially quantifiable through ratiometric analysis. In some scenarios, activatable systems amplify signals, as the recognitions catalyze or trigger a cascade of reactions that transduce multiple signals.[16,228] The target versatility includes ions, small molecules, molecular receptors, DNA, antibodies, enzymes, pathogens, among others, and makes activatable sensors useful for clinical diagnostics, environmental monitoring, and food safety. In this section, we

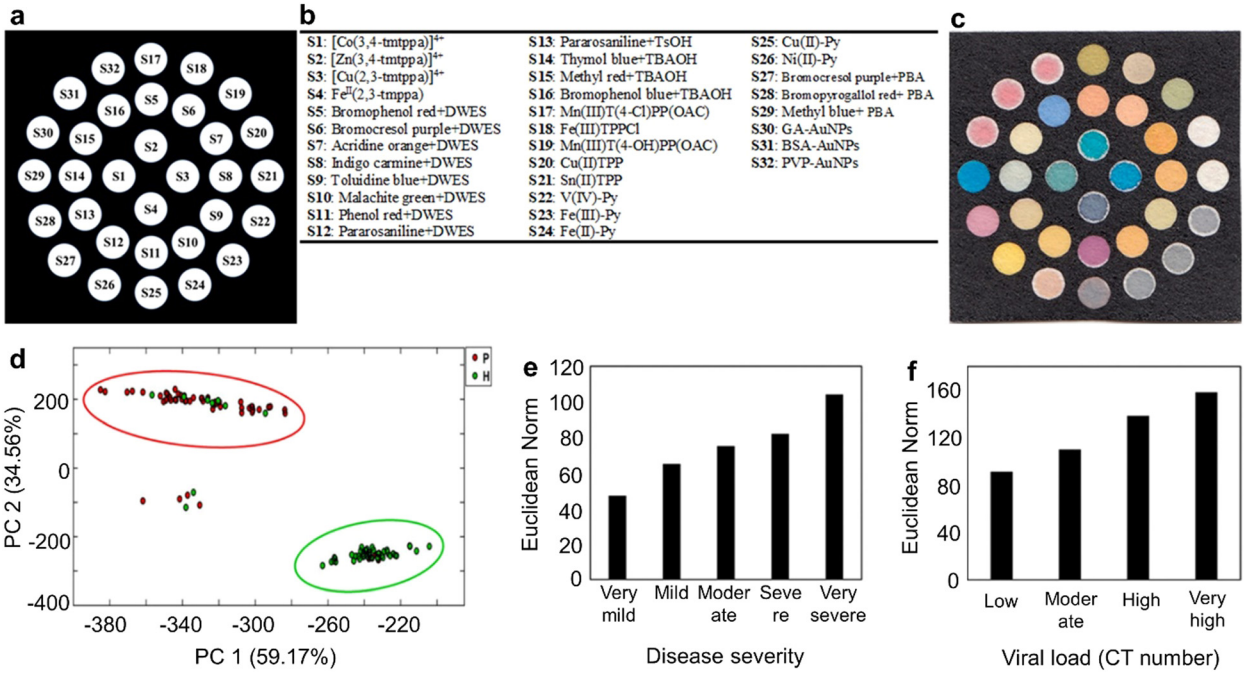

Fig. 24 Sensor-arrays for exhaled breath sensing. (a)–(c) The schematic pattern of sensor designed by AutoCAD, the names of sensing elements and their locations and the image of fabricated sensor array.[224] (d) The score plots obtained by PCA analysis for three different matrices including the data of patients and healthy samples.[224] (e) The correlation between the response of S8 and disease severity and (f) the relationship of S15 responses with the viral load obtained by rRT-PCR analysis. Reproduced with permission from ref. 224. Copyright 2022 Elsevier.

organize the presentation flow and chemistry insights based on various analytes, and describe the use of inorganic nanoparticles and organic chromophores as color agents.

6.1 Ions and functional groups

6.1.1 Protons (H^+). Colorimetric proton assays are crucial for pH monitoring in cells, health, and industry, given the critical role of pH in metabolism and chemical reactions. The combination of conventional pH-sensitive dyes, such as phenolphthalein, thymol blue, bromophenol blue, and methyl red, on filter paper produces commercially available pH strips (Fig. 25a).[60] These strips surpass conventional litmus paper by providing a refined and accurate pH readout in various settings including laboratory and aquarium. In addition to alkalinity/acidity test, the commercial pool, spa, or fish water test strips (*e.g.*, EASYTEST 7®) show extra color detection for ions (bromine, chlorine), total hardness, and cyanuric acid. Recently developed diapers (Kirkland signature brand) contain a wetness indicator—bromophenol blue—a pH-sensitive dye (Fig. 25b). The diaper initially appears yellow when dry, but the alkaline pH of urine (pH 4.5–7.8) causes it to turn blue when wet. This color change serves as a quick indicator for parents to know when the diaper needs changing.

Over the past decade, flavylium compounds, derived from natural flavonoids and contribute to plant colors, have emerged as a relatively new class of pH indicators, food colorants, and textile dyes.[230] For example, carboxypyranomalvidin-3-*O*-glucoside (vitisin A), a polyphenolic pigment present in red wines, exhibits a remarkable color tuning from pH 0.3 to 10.[231] The flavylium cation and quinoidal bases of riccionidin A also display different colors at the same pH range (0.3 to 10).[232] While effective for pH measurement, common pH indicator dyes have limited transition ranges and sensitivity. This can pose challenges when measuring pH at low concentrations or within hard-to-reach compartments like cells. Alternative dyes, like fluorescein and its derivatives, as well as benzoxanthene dyes such as seminaphthorhodafluor (SNARF), have been employed for enhanced pH sensitivity within the physiological range (pH 7.3–7.4) and for intracellular measurement.[233] Most studies have focused on the pH-dependent emission profiles of these dyes. However, we emphasize that they also exhibit pH-dependent absorbance profiles and are suitable for ratiometric and colorimetric pH analysis. For example, SNARF exhibits absorption peaks at 475 and 515 nm (orange) at pH 6 and at 550 nm (pink) at pH 9 (Fig. 28c).[56,234] In addition, ICG and Cyanine7.5 derivatives with nucleophilic substituents can change colors from green to brown through reversible self-cyclization at alkaline conditions.

Conducting polymers, such as polyaniline, are also used as optical pH sensors. The electronic absorption band of polyaniline sensitive to pH changes is very broad and extends into the near-infrared region, making it suitable for pH measurement in the range of pH 2–12.[73]

In addition to organic colorants, inorganic nanoparticles coated with proton-sensitive ligands have been utilized as pH reporters. For instance, Kim *et al.* developed a pH-sensitive ligand, 4-(2-(6,8-dimercaptooctanamido)ethylamino)-2-methyl-4-oxobut-2-enoic acid, which undergoes a charge conversion

Table 7 Representative work: sensor-arrays colorimetric detection for various analytes

Analyte	Probe	Sensing strategy	LoD	Ref.
Metal ions	MUA-capped AuNPs and amino acids	LSPR change of AuNPs due to Aggregation	N.A.	225
Metal ions	MCE, Cys, GSH and Urease	Change of pH due to the metal-free urease converting urea in ammonium	2.29 nM	197
Small molecules – toxic gases	Chemically responsive dyes	A set of 36 different dyes react with the analyte *via* Lewis basicity, Brønsted acidity/basicity, polarity or redox reactions.	1–50 ppm	189
Small molecules – organic solvents and anions	Porphyrin-anion supramolecular assemblies	Organic solvents or anions interfere with the assembly	N.A.	190
Small molecules – biogenic amines	pH-sensitive dyes complexed with nanomaterials	Change of alkalinity	1.3 ppb	191
Small molecule – triacetone	Redox dyes	Acid decomposition	<2 ppb	198
Small molecules	Imprinted polymers and benzofurazan-based dye	Dye displacement	N.A.	202
Small molecules – Aroma	Amino acids conjugated AuNPs	Aggregation of AuNPs	0.5 g L^{-1}	201
Small molecules – VOCs	Chemically responsive dyes	A set of 36 different dyes react with the analyte *via* Lewis basicity, Brønsted acidity/basicity, polarity or redox reactions.	N.A.	61
Proteins	Metal-nanoparticle (NP)-supported nanozymes (MNN)	The analyte interfere with in the catalysis of TMB by the MNN	N.A.	195
Proteins	ssDNA aptamers and AuNPs	The analyte disturb the aptamer-nanoparticles interaction and causes their aggregation.	50 nM	204
Proteins	DNA strands and AuNPs	Binding between the proteins and the DNA that affect the colloidal stability of AuNPs.	20 nM	205
Proteins	Peptides and silver nanoparticles	Peptide-induced reshaping of nanoparticles	500 pM	20
Cells	DNA-AuNPs conjugates	Seeded-growth methods affected by cellular uptake.	N.A.	218
Microorganisms – Bacteria and fungi	AuNPs with diverse surface charges	Aggregation of AuNPs	N.A.	196
Microorganisms – Bacteria and proteins	Citrate-capped AuNPs and AgNPs	NPs aggregation	0.5 μM	220
Microorganisms – Bacteria	Amino acids modified AuNPs	Bacteria metabolism induce AuNPs aggregation	N.A.	221
Microorganisms – Bacteria	36 chemically responsive dyes	Metalloporphyrins, pH indicators, metal salts, and solvatochromic dyes, that change color when exposed to a broad range of volatile analytes.	N.A.	226
Pathology – Lung cancer	Chemically responsive dyes	A set of 36 different dyes react with the analyte *via* Lewis basicity, Brønsted acidity/basicity, polarity or redox reactions.	N.A.	222
Pathology – Covid-19	Optical sniffer composed of 32 sensing elements (porphyrazines, organic dyes, modified AuNPs, *etc.*)	Interaction between volatile metabolites and the sensing elements.	N.A.	224

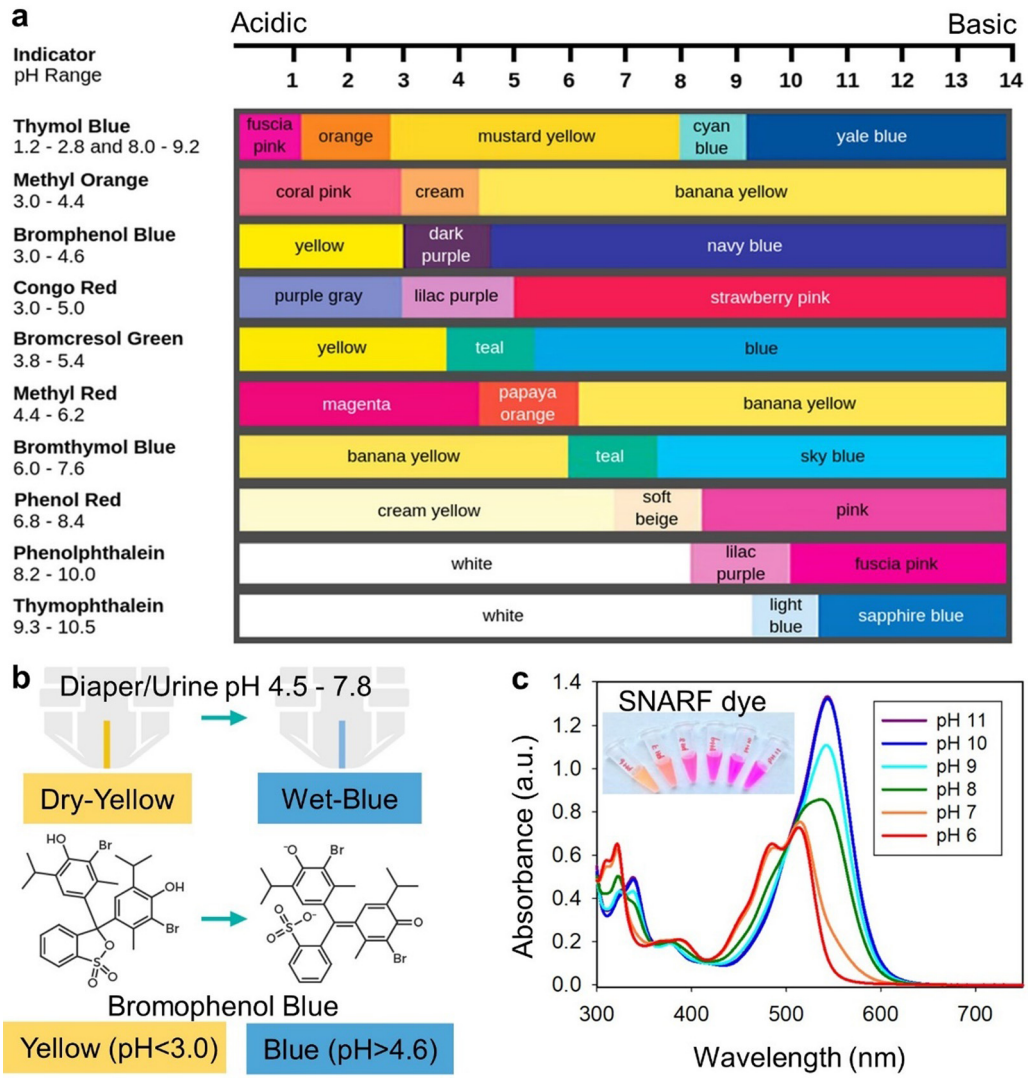

Fig. 25 Color detection for protons. (a) pH Indicator chart.[229] (b) Commercial diapers use bromophenol blue as a wetness indicator from yellow (dry) to blue (wet). (c) The absorbance and color of SNARF dye are pH dependent.[56] (a) Photo credit to Labster.com. (c) Reproduced with permission from ref. 56. Copyright 2019 American Institute of Physics.

from negative to positive in an acidic environment. AuNPs functionalized with this ligand exhibited electrostatic-induced aggregation at pH 5.5, leading to cancer cells imaging and localized heating for cancer treatment.[235]

6.1.2 Mercury ion (Hg^{2+}). The World Health Organization (WHO) mandates a maximum allowable level of inorganic mercury in drinking water, set at 6 ppb (30 nM). Mercury ions are classified as soft Lewis acids. Typical binding sites in mercury sensors include boronic acid, porphyrin, thiolate, carboxylate groups, aniline, and thymine residues. Reversible mono- and bis-boronic acid-bearing rhodamine derivatives were developed by Yoon *et al.* as colorimetric sensors for Hg^{2+}, with measured association constants of 3.3×10^3 M^{-1} and 2.1×10^4 M^{-1}, respectively. The spirolactam ring opening by Hg^{2+} complexation accounted for the fluorescence enhancement and color changes.[236]

Hg^{2+} coordinates with the lone pair electrons of nitrogen, forming stable coordination complexes based on the HSAB theory.[237] For instance, Jung *et al.* reported aniline-bearing azobenzene receptors for Hg^{2+} detection, which change color from yellow to deep red. The color change is due to aniline-Hg^{2+} complexation favored by electronic charge transfer upon photoexcitation (or intramolecular charge transfer, ICT). The association constant for aniline-Hg^{2+} coordination was 3.05×10^5 M^{-1}.[238] This formulation was further coated onto a portable chemosensor film to achieve a mercury detection limit as low as 28 nM.[238] The ICT mechanism of azobenzene and Hg^{2+} has been leveraged for many mercury chemosensors with various binding sites, such as dithioacetal deprotection.[239] Other studies use porphyrin as an excellent ion binding chemosensors because of its multiple pyrrolic N atoms, variable macrocycle sizes, peripheral substitution, and tunable optical profiles.[57]

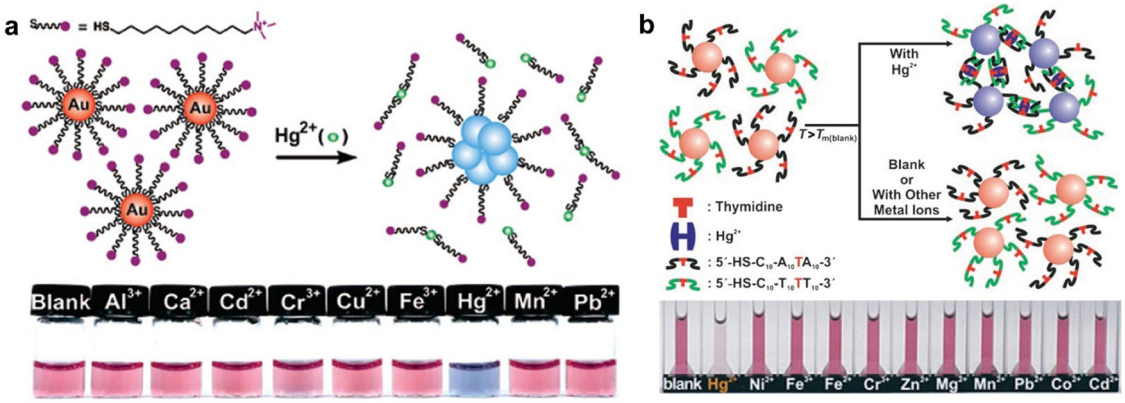

Fig. 26 Color detection for mercury. (a) Schematic representation of mechanism for the Hg^{2+} induced colorimetric response of quintenary ammonium-AuNPs.[241] (b) Colorimetric detection of mercuric ion using T–Hg^{2+}–T interactions and DNA-AuNPs.[242] (a) Reprinted with permission from ref. 241. Copyright 2010 American Chemical Society. (b) Reproduced with permission from ref. 242. Copyright 2007 Wiley.

Liu *et al.* developed porphyrin-based Hg^{2+} chemosensors, including tri-(p-carboxyphenyl)porphyrin-cholesterol dyad (TPPOC), which exhibited selective colorimetric response to both organic and inorganic mercury in water. TPPOC aggregates showed decreased absorption at 404 nm and a new peak at 465 nm upon the addition of organic $PhHg^{2+}$, resulting in a color change from light pink to bright green. Inorganic Hg^{2+} ions caused a color change from light pink to olive yellow, allowing discrimination between organic and inorganic mercury. The binding constant for the porphyrin aggregates with $PhHg^{2+}$ was higher than that of the free structure, and the detection limit was 6.7×10^{-7} M.[240]

The sulfhydryl-/thymine-Hg^{2+} coordination has been widely utilized in plasmonic nanoparticle strategies for colorimetric mercury detection. For example, Jiang *et al.* found that only Hg^{2+} removes thiolates from AuNPs capped with (11-mercaptoundecyl)-trimethylammonium, QA-AuNPs.[241] The introduction of Hg^{2+} to QA-AuNPs led to a red-to-blue color change due to high affinity of Hg-S binding and competitively break Au–S bonds,[127] a transformation not observed with other metal ions (Fig. 26a). The detection limit was 30 nM with a wide detection range from 3×10^{-8} to 1×10^{-2} M. The Mirkin group developed a colorimetric assay for Hg^{2+} using a complementary DNA-AuNP system that relies on thymine–Hg^{2+}–thymine (T–Hg^{2+}–T) coordination chemistry. The dsDNA de-hybridizes at the melting temperature, causing a color change from purple to red. However, in the presence of Hg^{2+}, the color remains purple due to strong T–Hg^{2+}–T coordination, enhancing sensitivity and lowering the limit of detection to 100 nM (20 ppb), which is much lower than organic colorimetric systems (Fig. 26b).[242] Chen *et al.* utilized the T–Hg^{2+}–T coordination to further develop portable μPADs for mercury detection.[243] Their cocktail included label-free ssDNA and unmodified AuNPs that interact with each other *via* hydrophobic interactions. The addition of Hg^{2+} ions changes the ssDNA structure into a hairpin structure based on T coordination chemistry, leading to reduced surface potential, AuNP aggregation, and color change. This strategy is specific to Hg^{2+} and improves the detection limit to 50 nM using simple paper-based devices. Results can be read and stored using cloud computing *via* a smartphone, and the total turnaround time is 40 min.

6.1.3 Nitrite (NO_2^-). Nitrite is a common water contaminant with environmental and health risks. It is also a vital biomarker for early urinary tract infections (UTI) diagnosis, as bacteria like *E. coli* in UTIs convert nitrate into nitrite. A positive nitrite test in urine indicates a 99% likelihood of UTI in children of all ages.[244] Griess test is used to detect the presence of nitrite. For example, the Griess assay measures nitrite concentrations in biological samples and serves as the European standard for assessing nitrite concentrations in drinking water and detecting nitroglycerine in forensic science. This assay is based on the reaction of nitrite with a sulfanilamide derivative and *N*-(1-naphthyl)-ethylenediamine to form a reddish-purple azo compound (Fig. 27a). The detection limit of the Griess test ranges between 0.02 and 2 μM. The modified Griess reactions provide fundamental solutions for building nitrite diagnostic devices. For example, Budd *et al.* developed an innovative transmission-based colorimeter for the quantitative read based on Chemstrip 10 + SG test strip and the Multistix 10SG test strip (Fig. 27b). The detection limit in artificial urine was determined as 1.6 μM, which is 16× more sensitive than commercial dipstick reflectance analyzers such as Urisys 1100 and Clinitek Status+.[245]

The Griess reaction was also employed by Mirkin *et al.* within an AuNP-crosslinking strategy to develop a colorimetric assay for nitrite detection, and the detection limit was 22 μM (Fig. 27c).[246] Beyond Griess mechanism, Zhang *et al.* developed an AuNPs dissociation strategy for nitrite detection. They initiated the process by aggregating AuNPs with 4-aminothiophenol (4-ATP) as the color agents. Introduction of nitrite under acidic conditions reacted with the amine group of 4-ATP, thus forming a diazonium cation and causing AuNP dissociation. This resulted in a color shift from purple to red, with a low LoD of 1 μM.[247]

6.1.4 Cyanide (CN^-). The median lethal dose (LD_{50}) of hydrogen cyanide ranges from 2,500 to 5000 mg min m^{-3}, and the maximum acceptable cyanide concentration in drinking

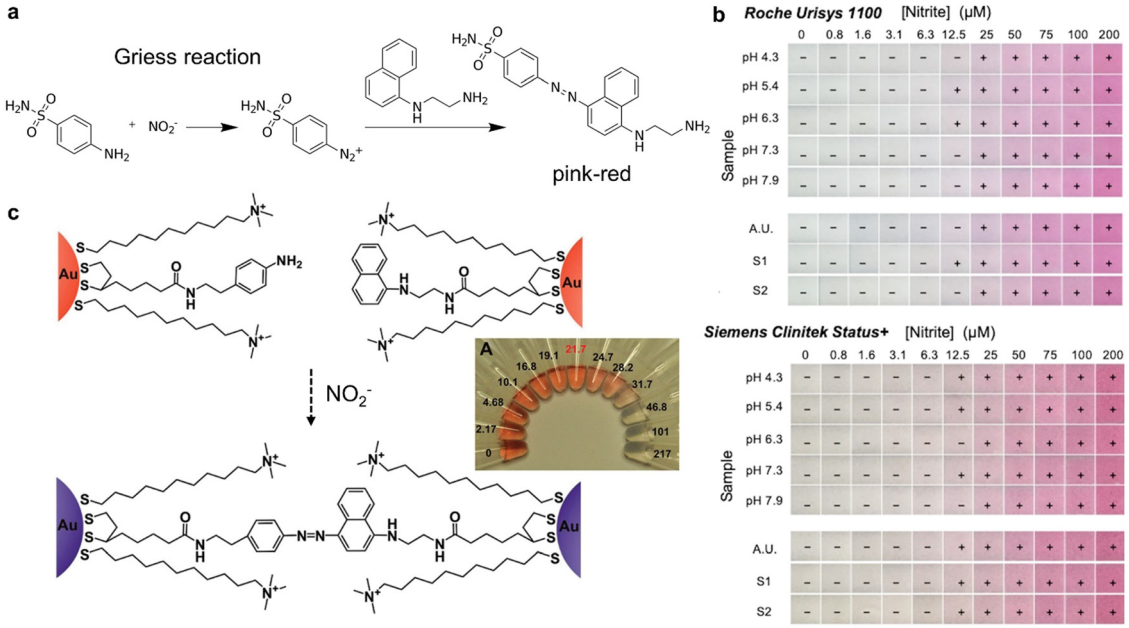

Fig. 27 Color detection for nitrite. (a) The Griess test is a two-step reaction. (b) Cropped images of commercially available Chemstrip 10 + SG and Multistix 10SG dipsticks that were exposed to varying concentrations of nitrite and pH. These dipsticks were used for at-home UTI detection.[245] (c) Colorimetric detection of nitrite with functionalized AuNPs by Griess reaction. Photograph of the AuNP dispersions after incubation with various concentrations of nitrite.[246] (b) Reproduced from ref. 245 in accordance with CC BY-NC-ND 4.0. Copyright 2022 American Chemical Society. (c) Reprinted with permission from ref. 246. Copyright 2009 American Chemical Society.

water is 0.5 mg L^{-1} for over 5 days (or 1.9 μM), as per the WHO.[248] Generally, the presence of CN^- induces nucleophilic addition to certain chromophores, leading to chromogenic transformations and color changes. For example, Raymo *et al.* developed a chromogenic oxazine molecule that detects cyanide as low as 1 μM through a quantitative chromogenic transformation. The [1,3]oxazine ring of the compound opens in response to CN^- to form a 4-nitrophenylazophenolate chromophore, resulting in a color change from yellow to red (Fig. 28a).[249] Guo *et al.* developed a rhodafluor dye probe with a trifluoroacetylamino moiety (TFA-RF1), which reacts with CN^- to form cyanohydrins and turns color from colorless to yellowish green. TFA-RF1 probe exhibited a detection limit of 26.6 nM and high selectivity with minimal fluorescence changes induced by other anions.[250] Li *et al.* developed a ratiometric colorimetric molecule (Azo-1) to detect CN^- in CH_3CN solutions. The addition of CN^- to Azo-1's dicyano-vinyl group reduces the conjugated electron network and intramolecular charge transfer efficiency, causing a color change from deep red to light yellow (Fig. 28b). It can be used as a practical colorimetric sensor with a 1.1 μM detection limit on a "dip-stick" format.[251]

The strong complexation of metal atoms with CN^- is harnessed for colorimetric sensing using metallic NPs.[40] For example, Ju *et al.* reported that cysteamine-decorated AuNPs form $Au(CN)_n$ complexes and undergo a color shift from red to purple in the presence of CN^- due to the detachment of surface ligands. The system displayed a detection limit of 128 nM and minimal interference from other anions.[253] Chen *et al.* extended the color change range using Au@Ag core/shell nanoparticles. They showed an absorption shift from 400 nm to 520 nm with CN-etching and $[Ag(CN)_2]^-$ complex formation, achieving a 0.4 μM detection limit. Their study highlighted the advantages of the core–shell structure compared to individual AuNPs and AgNPs. (Fig. 28c).[252]

6.1.5 Reactive oxygen species (ROS). Aerobic organisms generate ROS during vital processes, which play diverse roles in signal transduction, inflammation, carcinogenesis, and neurodegenerative injury. Most ROS probes report *via* fluorescence, and there have been few reports of colorimetric sensors for this purpose. The most common ROS is hydrogen peroxide (H_2O_2) that has been widely tested by colorimetric strip. The commercial test strips use peroxidase enzymes and TMB reagent to react with H_2O_2, causing a color change from colorless to blue correlated with its concentration (0–100 ppm) for quantitative measurement. Custom colorimetric assays were developed for detecting various ROS (*e.g.*, –OCl, $ONOO^-$, and H_2O_2). Zhang *et al.* reported a simple tricyanoethylene-derived colorimetric dye probe for –OCl detection.[254] Upon the addition of –OCl, the probe exhibits a significant decrease in absorbance at 527 nm and undergoes a color change from red to colorless within 10 min, and the detection limit is 4 μM. Jokerst *et al.* developed hybrid Ag-coated Au nanorods (Au/AgNRs) capable of Ag–shell dissolution upon ROS exposure like hydrogen peroxide and peroxynitrite. Oxidative etching of the silver shell causes changes in absorption spectra, allowing for colorimetric and photoacoustic imaging. The linear range of ROS detection spanned in mM was reported, and the ability of endogenously generated ROS to oxidize the silver shells was validated using photoacoustic imaging with ovarian cancer cells (SKOV3), known for high levels of free radical production.[255] The same

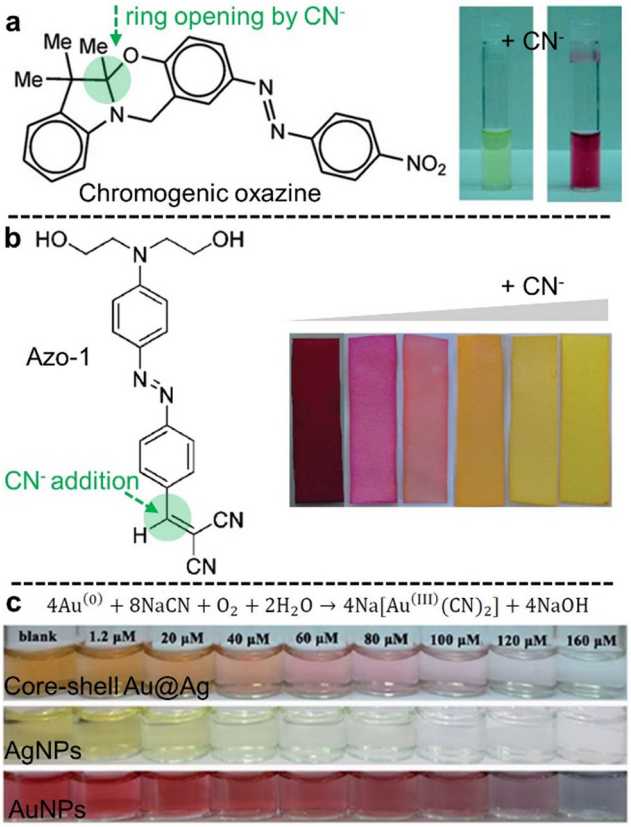

Fig. 28 Color detection for cyanide. (a) The [1,3]oxazine ring of the chromogenic oxazine reacts with CN^-, resulting in a color change from yellow to red.[249] (b) Increasing concentrations of CN^- to Azo-1 causes color change from red to yellow on the test strips.[251] (c) Photographs of the Au@Ag core/shell NPs Ag NPs and Au NPs with the addition of various amounts of cyanide.[252] (a) Reprinted with permission from ref. 249. Copyright 2005 American Chemical Society. (b) Reprinted with permission from ref. 251. Copyright 2012 American Chemical Society. (c) Reproduced from ref. 252 (2014) with permission from the Royal Society of Chemistry.

group later fine-tuned the electrochemical properties of these materials by employing halide doping (AgI/AuNR). Halide doping lowered the reduction potential of Ag, resulting in significantly increased sensitivity to H_2O_2 (1000-fold) and $ONOO^-$ (100 000-fold).[45]

6.1.6 Thiols. Thiols (or sulfhydryl groups) are crucial in mediating redox environment, *e.g.*, molecules like cysteine (Cys), homocysteine (Hcy), and glutathione (GSH) are key participants in many biological events,[256] while synthetic aromatic thiols are highly toxic to human body.[21] In addition to small thiol molecules, Cys sulfhydryl is crucial to the overall functionality and engineering of proteins (*e.g.*, enzyme catalytic domain, antibody–drug conjugation).[257] Finally, thiols and amines serve as key target analytes for detecting food spoilage, exemplified by putrescine, cadaverine, and tyramine resulting from decarboxylation processes mediated by decarboxylases, as well as methanethiol, ethanethiol, and dimethyl sulfide generated through microbial degradation of cysteine and methionine residues. Ellman's colorimetric assay measures thiol concentration and thiol-containing enzyme activity in biological samples by reacting 5,5′-dithiobis-(2-nitrobenzoic acid) (DTNB) with thiols to create a yellow product, TNB, quantified through spectrophotometer absorbance (ε = 14 150 M^{-1} cm^{-1} at 412 nm).[258] This mechanism is used in the commercial Glutathione Assay Kit available from Sigma-Aldrich Inc. Ellman's reagent is sensitive to hydrolysis, potentially leading to underestimated thiol concentration and susceptibility to background interference from protein absorbance. Recently, coumarin and chromene derivatives were reported to detect biological thiols. For example, Yin *et al.* developed a selective thiol-containing colorimetric probe using a chromene derivative. The probe rapidly detects thiol species such as Cys (k_{obs} = 0.62 s^{-1}), Hcy (k_{obs} = 0.065 s^{-1}), and GSH (k_{obs} = 0.082 s^{-1}) in buffer, producing a color change from colorless to yellow within 10 s.[259] Hirai *et al.* developed a reusable chemosensor using a colorless spiropyran dye that transforms into the colored merocyanine form upon exposure to aromatic thiols. The dye can be reverted back to its original colorless spirocyclic form with visible light irradiation.[260]

While the previously mentioned dye colorants showed limited selectivity for thiols, Strongin *et al.* achieved selective detection between Cys and Hcy using a readily available aldehyde molecule.[261] Upon addition of Cys to the aldehyde molecule, a color change from yellow to colorless was observed within 10 min, while Hcy did not induce any color change.[261] Zhao *et al.* introduced a dication methyl viologen that affords selective blue color formation only corresponding to the presence of Hcy but not Cys or GSH in plasma media (Fig. 29a).[261]

Antibody–drug conjugate (ADC) was conceived to bridge the gap between the mAb and cytotoxic drug for the improvement

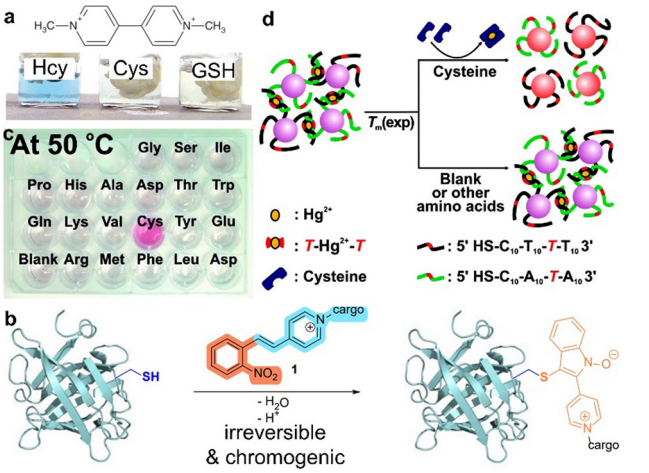

Fig. 29 Color detection for thiols. (a) Selective Hcy detection in human plasma by a dipyridinium cation methyl viologen, showing a blue color.[261] (b) Merging the thiol–ene reaction of vinyl-pyridinium ions with *N*-hydroxy indole synthesis results in an irreversible cysteine bioconjugation that is accompanied by color change.[262] (c) Colorimetric detection of cysteine using DNA–AuNPs in a competition assay format. (d) The colorimetric response of the DNA–AuNP/Hg^{2+} complex aggregates in the presence of the various amino acids (each at 1 μM) at 50 °C.[263] (a) Reprinted with permission from ref. 261. Copyright 2005 American Chemical Society. (b) Reprinted with permission from ref. 262. Copyright 2023 ChemRxiv. (c) and (d) Reprinted with permission from ref. 263. Copyright 2008 American Chemical Society.

of therapeutic window.[257] After IgG reduction, interchain disulfide bonds are easily reduced on the antibody's surface, exposing free cysteine sites for conjugation, reducing ADC heterogeneity. Colorimetric evaluating the drug to antibody ratio promotes an easy measure for the quality of ADC. Köhler *et al.* discovered that the addition of a sulfhydryl group to water-soluble *N*-alkyl(*o*-nitrostyryl)pyridinium ions, leads to the formation of *N*-hydroxy indole pyridinium ions (Fig. 29b).[262] The accompanying red-shift (>70 nm) to around 385 nm enables convenient monitoring of the drug labeling yield using an absorption spectroscopy.

Unlike cyanide that etches surface atoms, thiols (soft Lewis bases) coordinate onto AuNPs *via* thiolate–Au bond (strength = 126–184 kJ mol^{-1}).[118] This strong coordination enables thiol sensing *via* competitive displacement strategies. The first approach uses weakly-bound AuNP-dye and fluorescence recovery transduction.[33,264] The second approach uses disassociation of AuNP aggregates and visual color changes. For example, Qiu *et al.* developed a colorimetric assay for detecting biothiols (GSH, Hcy, and Cys) using S-adenosyl-L-methionine aggregated AuNPs. Aggregated AuNPs react with biothiols, dispersing the particles and changing the color from purple to red. The detection limits are 35.8 nM for GSH, 21.7 nM for Cys, and 62.4 nM for Hcy, all within 5 min.[265] Mirkin *et al.* devised a highly sensitive and selective cysteine detection using AuNPs functionalized with strategically placed thymidine–thymidine mismatches complexed with Hg^{2+} (Fig. 29c and d). This assay relies on the sharp melting transition of nanoparticle aggregates (purple) and the very specific coordination of Hg^{2+} with cysteine (red) from other amino acids. The detection limit is 100 nM for cysteine.[263]

6.2 Small (bio)molecules

6.2.1 Adrenaline. Adrenaline, also known as epinephrine, serves both as a hormone for stress response and as an anesthetic adjuvant to extend block duration. Sugimoto *et al.* employed molecularly imprinted polymers (MIP) incorporated with close-packed AuNPs as a colorimetric sensor. Adrenaline causes the MIP gel to swell, inducing a blue shift in the SPR of the immobilized AuNPs with a detection limit of 5 μM.[266] Ma *et al.* detected adrenaline using AuNPs coated with 4-amino-3-hydrazino-5-mercapto-1,2,4-triazol (AHMT) as a colorimetric sensor. Adrenaline's one amine group and three hydroxyl groups offer four hydrogen bonding sites for NH···O and NH···N with AHMT ligands, leading to AuNP aggregation and producing a color change. The limit of detection for was 1 nM.[267] Seal *et al.* optimized the label-free detection of adrenaline using aptamer-functionalized AuNPs. By conjugating 2 nM thiolated aptamers with 13 nm spherical particles in the presence of salt, they achieved a high detection limit of 0.9 nM for adrenaline due to the reduced surface potential. Furthermore, they tested the performance of the sensor on a hydrophobic cellulose-based paper substrate, enabling the build-up of a portable and point-of-care tool.[268] Despite concerted efforts, there is currently no standardized colorimetric point-of-care device available in the market for detecting adrenaline.

6.2.2 Glucose. High glucose levels lead to serious health issues in diabetes patients, making glucose measurement critical for patient-specific insulin therapy and disease management. The color detection of reducing sugars, including glucose in urine, can be traced back to the year 1848 (Fehling's solution) and the year 1908 (Benedict's solutions). Subsequently, the hydrogen peroxide produced during glucose oxidation by glucose oxidase (GOx) provides a fundamental mechanism for various test strips (*e.g.*, Clinitest®, Tes-tape roll®, Clinistix®, Dextrostix®) and colorimetric glucose determination.[269] In 1963, Ernie Adams invented Dextrostix®, a paper strip that changes color proportionally to glucose concentration.[270] The paper strip coated with dehydrated GOx was integrated into some glucose meters to colorimetrically measure hydrogen peroxide.[271] Glucose dehydrogenase, hexokinase, and Prussian blue NPs are alternatives to GOx.[44] A partial oxidation of 3,3′,5,5′-tetramethylbenzidine (TMB) by hydrogen peroxide lead to the production of a blue-green reaction product (Fig. 30a).[272] Yetisen *et al.* developed a tattoo biosensor to monitor glucose levels in interstitial fluid using glucose oxidase, TMB, and peroxidase (Fig. 30b and c). The sensor, injected into a porcine skin model's dermis layer, detects glucose by monitoring RGB values and color changes, transitioning from yellow to dark green in correlation with glucose levels from 2 to 50 mM.[273]

Alternatively, AuNPs and Prussian blue NPs are used for colorimetric glucose detection in low-step, wet-chemistry assays introduced by the Pinheiro group for three target biomarkers, including glucose. These assays are implemented on microfluidic paper-based devices, and the mechanism involves reduction of gold salt Au^{3+} to Au^0 by glucose's aldehyde group and nucleation of Au seeds, leading to red color shifts proportional to glucose concentration. The detection limit was 1.25 mM for this method, which is higher compared to the enzymatic GOx/TMB method (*i.e.*, 0.01–0.9 mM).[274]

6.2.3 Phenolic compounds. Phenolic compounds are secondary metabolites including catechol, dopamine, flavonoids, and polyphenols. Dopamine is a key neurotransmitter central to brain functions, including reward-related behavior, movement, and mood. Tian *et al.* reported that AuNPs functionalized with 4-mercaptophenylboronic acid (MBA) and dithiobis(succinimidylpropionate) (DSP) ligands exhibited specific recognition to the diols and amine groups in dopamine. This resulted in particle aggregation and color changes with a detection limit of 0.5 nM. Furthermore, MBA/DSP-AuNPs were used to analyze dopamine levels in the rat brain through *in vivo* microdialysis, detecting fluctuations caused by nomifensine and tetrodotoxin injection.[275] Kim *et al.* used DNA-copper hybrid nanoflowers with laccase-mimicking nanozymes to distinguish phenolic compounds in paper microfluidic devices. The enzymatic oxidation of phenolic compounds reacted with a coated 4-aminoantipyrine substrate resulted in a colored adduct. This setup enabled colorimetric detection of phenolic compounds, such as dopamine, catechol, and hydroquinone, with low detection limits of 4.5, 3.0, and 4.5 μg mL^{-1}, suitable for point-of-care testing.[276]

6.2.4 Antibiotics. Widespread use of antibiotics is leading to resistance—this is a global issue as highlighted by the WHO.

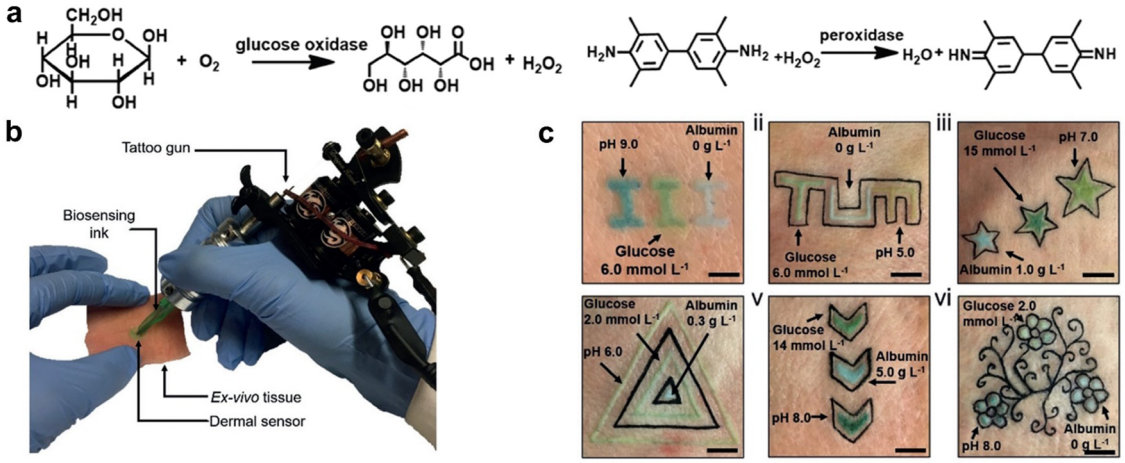

Fig. 30 Color detection of glucose. (a) The chemical structures of the glucose-sensing compounds involve (i) the oxidation of D-glucose to D-gluconolactone and the generation of hydrogen peroxide, and (ii) the oxidation of TMB, resulting in the formation of a blue-green dye in the presence of hydrogen peroxide.[273] (b) The biosensing ink was injected into the dermis layer of a porcine skin using a tattoo gun.[273] (c) Multiplexed dermal biosensors were created with individual areas dedicated to the detection of different analytes, producing various colors corresponding to pH, glucose, and albumin concentrations.[273] Reproduced with permission from ref. 273. Copyright 2019 Wiley.

Colorimetric sensors for antibiotics typically use nanoparticles. For instance, Zhang *et al.* demonstrated that penicilloic acid binds to Au@Ag NPs *via* two carboxyl groups, leading to a color change from yellow to grey.[277] Chavada *et al.* developed an ultra-sensitive colorimetric technique using unfunctionalized AgNPs to detect azithromycin (AZM).[278] At a concentration as low as 0.2 μM, AZM induced rapid aggregation of AgNPs through electrostatic interactions, resulting in a color change from yellow to purple. In fact, a lack of practical antibiotic-detection colorimetric sensors persists, which remains at the bench level with limited translation to practical applications.[279]

6.2.5 Toxins. Exposure to fungal, bacterial, or marine toxins causes serious foodborne concern.[280] For example, tetrodotoxin (TTX) is a potent neurotoxic marine toxin found in pufferfish and blue-ringed octopus.[281] TTX detection is crucial for food safety, given that approximately 50 people die from such poisoning in Japan annually. Ling *et al.* developed specific and sensitive immunochromatographic test strips using an anti-toxin monoclonal antibody, gold nanoflower (AuNF), and latex microsphere (LM) probes.[282] These POC test strips exhibited a linear detection range of 9.5–331.0 ng mL^{-1} for AuNF and 5.4–443.2 ng mL^{-1} for LM, with respective limits of detection of 9.5 ng mL^{-1} and 5.4 ng mL^{-1}.

6.2.6 Drugs of abuse. The proliferation of drugs of abuse is occurring at an accelerated pace globally. Colorimetric spot tests allow law enforcement officers or crime scene analysts to make a quick on-site presumptive identification when a potential drug is seized from a suspect. Several commercially available spot tests, *e.g.*, Marquis (NIK-A), Duquenois-Levine, and modified Scott (NIK-G) utilize a mix-and-measure assay for visualizing cocaine and opioids like fentanyl, hydrocodone, and heroin (Table 4).[283–285] Fig. 31a displays the results of testing fentanyl with the NIK-A test and cocaine with the NIK-G test. Fentanyl produced an immediate orange color in the NIK-A test, which darkened to brown over 3 minutes. Cocaine, when tested with the NIK-G test, resulted in a final presentation of a top pink layer over a bottom blue layer. Kangas *et al.* improved the mix-and-measure testing by introducing a new Eosin Y device, which can be used as either a mix-and-measure assay or a paper test, providing color changes for the rapid detection of fentanyl and a mixture with cocaine or hydrocodone.[286] When compared to the control (water), the color changes are visible to the naked eye in phosphate buffer (pH = 7) and acetate buffer (pH = 5) (Fig. 31b).

AuNP growth strategy has been utilized for colorimetric sensing of gamma-hydroxybutyric acid (GHB), a previous anesthetic used in the 1960s and now known for its recreational use due to its euphoric effects.[288] Despite its popularity, GHB misuse has been linked to neurotoxic damage. Xing *et al.* introduced a GHB detection involving a specific enzyme-substrate interaction with GHB dehydrogenase, leading to oxidation and producing nicotinamide adenine dinucleotide (NADH).[287] The NADH molecule facilitates the reduction of a gold(III) complex, yielding a pink color with a sensitivity of 3.51 mM (Fig. 31c).

6.3 Oligonucleotides

Oligonucleotides detection is of utmost importance in genetic research, diagnostics, and therapeutics, driving advancements in vaccine medicine, disease detection, and targeted drug delivery. The COVID pandemic has heightened public health awareness, amplifying this significance. PCR and southern blot use fluorescent, radioactive, or DNA-binding dyes like ethidium bromide, SYBR Green, and propidium iodide, which change their fluorescence properties upon binding to DNA. Alternatively, AuNP-based colorimetric analysis has emerged as a formidable technology for oligonucleotide readout.[14,289] This technique primarily relies on plasmonic coupling, induced by DNA hybridization, charge screening effects, or nuclease digestion.

Functionalizing AuNPs with complementary single-stranded DNA (ssDNA) allows for the formation of compact superstructures upon DNA hybridization, leading to significant color

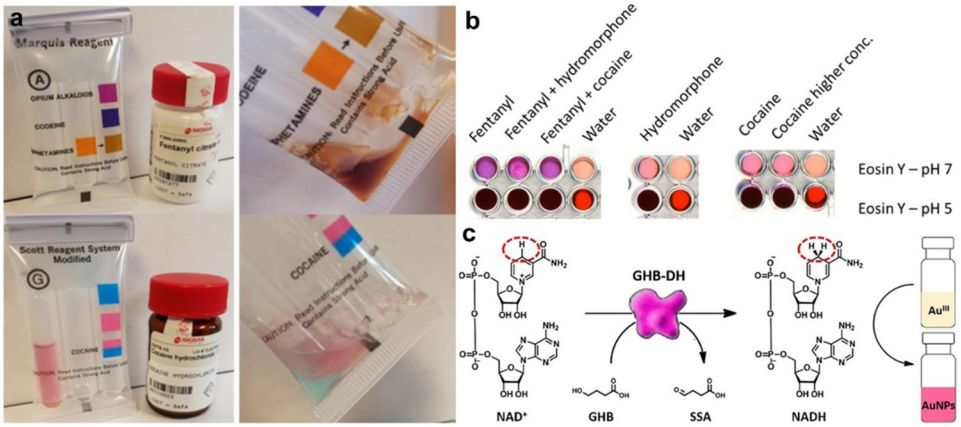

Fig. 31 Color detection of drug-of-abuse. (a) Results of commercial NIK-A and NIK-G test kit testing on fentanyl and cocaine, respectively.[286] (b) Eosin Y reacting with fentanyl, hydromorphone, cocaine and the mixtures leading to visible color changes in buffers (phosphate and acetate).[286] (c) Scheme illustration of a selective sensing of illicit date rape drug GHB by AuNP reduction.[287] (a) and (b) Reprinted with permission from ref. 286. Copyright 2017 Juniper Publishers. (c) Reprinted with permission from ref. 287. Copyright 2020 Wiley.

changes.[129] This colorimetric detection approach, initially pioneered by Mirkin *et al.* in 1996, involved using two sets of AuNPs functionalized with noncomplementary thiolate ssDNA strands, which were complementary to both ends of the target oligonucleotides (Fig. 32a). The highly specific base-pairing of DNA strands, combined with the exceptional absorptivity of AuNPs, enables the precise and sensitive quantitative colorimetric detection of the target analytes.[290,291]

The above colorimetric strategy uses specific AuNP crosslinking, yet it is non-directive and has drawbacks: low sensitivity (>5 nM) and a limited dynamic range. To address the drawbacks, Kim *et al.* finely tuned the surface DNA functionalization by promoting minimal interparticle gaps through the formation of a Y-shaped DNA duplex.[292] This approach enables selective oriented AuNP dimerization upon target binding, greatly improving long-term stability and broadening the detection range over two orders of magnitude compared to conventional sensors. (Fig. 32b and c). The limit of detection was 1 pM.

Most DNA-mediated colorimetric sensors rely on DNA hybridization, which requires heat cycles. Techniques such as triplex DNA binders allow for DNA-mediated colorimetric sensing at room temperature (Fig. 32d).[293] In these systems comprising DNA-AuNPs and target DNA analytes, triplex DNA binders lock and stabilize triplex structures below the melting temperature. This stabilization effect triggers the color change *via* particle aggregation. The assay's simplicity, without temperature cycles, makes it efficient for high-throughput screening of suitable binders from large combinatorial libraries.

While the crosslinking mechanism using DNA-AuNPs involves laborious salt-assisted DNA immobilization, an alternative non-crosslinking approach uses unmodified AuNPs for simply distinguishing between ssDNA and double-stranded DNA (dsDNA). The aggregation and resulting color change of AuNPs are triggered by the charge screening effect (or non-crosslinking) rather than crosslinking.[298,299] Rothberg *et al.* observed that ssDNA and dsDNA exhibit different tendencies to adsorb onto AuNPs in colloidal solutions, with ssDNA-adsorbed AuNPs exhibiting high stability in high ionic strength environments or *vice versa* (Fig. 32e).[295] This assay offers a simple implementation for visual detection at a level of 100 fmol and it can be easily adapted to detect single-base mismatches between the probe and target. Similarly, Li *et al.* harnessed this non-crosslinking mechanism to develop a visual and quantitative genetic detection method.[297] The ssDNA shields AuNPs from salt-induced destabilization. When target DNA is added, hybridization disrupts this protection, causing AuNP aggregation and color changes with a low LoD of 0.28 nM. Recent findings by Liu *et al.* demonstrated that NaF, as a salt for screening effect, exhibited a 2.3-fold higher sensitivity compared to NaCl in these assays due to the weak adsorption of F^- ions to gold surfaces, enhancing the sensitivity.[300] In a comprehensive study, Maede *et al.* compared the color change kinetics between crosslinking and non-crosslinking aggregation modes, both resulting in a red-to-purple color change.[301] The crosslinking mode showed faster color change with a small number (1 equiv.) of cross-linker/complementary DNAs. Conversely, the non-crosslinking aggregation occurred more rapidly than crosslinking when a large number (64 equiv.) of DNAs were present.

Nuclease cleavage is an alternative mechanism for colorimetric DNA detection, as well as for measuring nuclease activity. Zhang *et al.* reported that the positively charged cysteamine-capped AuNPs electrostatically aggregate with polyanionic DNA without S1 nuclease, leading to a purple/blue color.[294] However, S1 nuclease cleaves ssDNA into smaller fragments, preserving a red AuNP dispersion, enabling simple visual measurement of nuclease activity. The probe detected S1 nuclease activity in the 0–30 U mL^{-1} range.

An aptamer is a short, single-stranded DNA or RNA molecule that selectively binds to specific target molecules, widely used in molecular recognition, biosensing, and drug delivery. While many colorimetric sensors involve AuNP-aptamer conjugates are reported, here, we only focus on the universal approach validated by the Plaxco group.[301] This method utilizes a sensing strategy consisting of an ssDNA probe (or an aptamer),

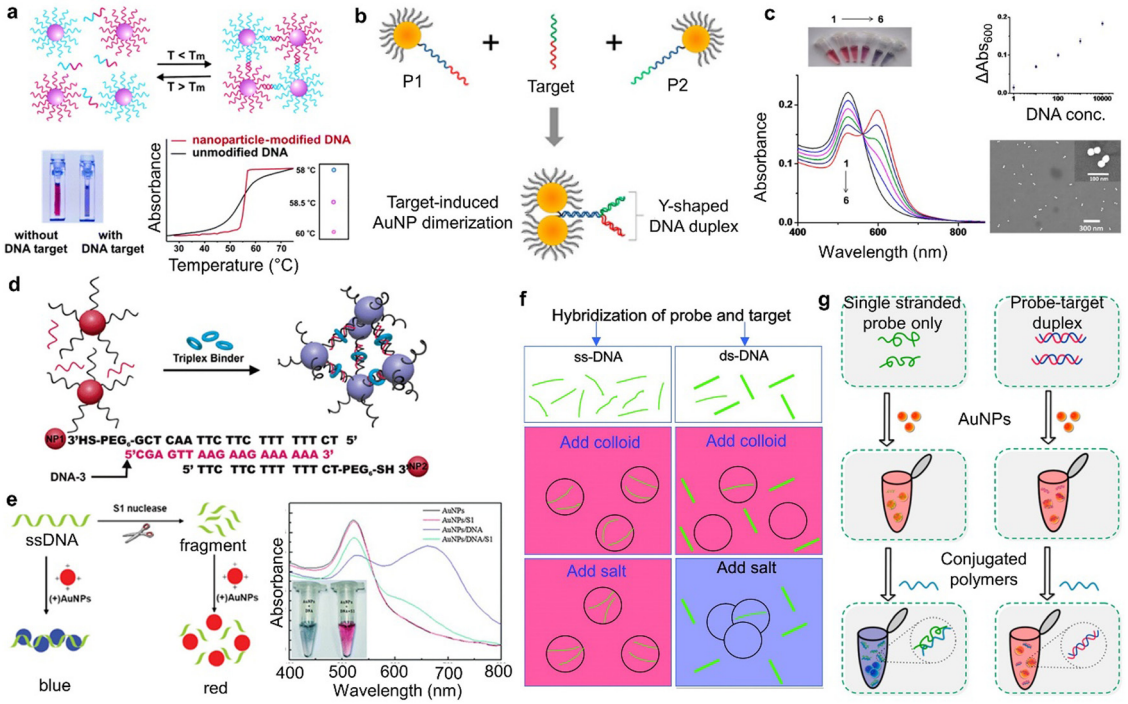

Fig. 32 Color detection of oligonucleotides. (a) Complementary target DNA triggers the aggregation of oligonucleotide-functionalized gold nanoparticles, resulting in a color change from red to blue, which can be observed using UV-vis spectroscopy or by spotting the solution on a silica support.[289] (b) The principle of enhancing sensor performance through AuNP dimerization by forming Y-shaped DNA structures.[292] (c) Experimental evidence including photographs, optical absorption spectra, and TEM images illustrating AuNP dimerization after adding different concentrations of target DNA.[292] (d) Representation of the structure and color change of the nanoassembly when a triplex binder is present at room temperature.[293] (e) Interaction between positively charged AuNPs and polyanionic ssDNA leads to AuNP aggregation and a color change from red to blue. However, enzymatic degradation of ssDNA by S1 nuclease prevents the color change. Absorption spectra of AuNPs in the presence of DNA are shown before and after digestion with S1 nuclease.[294] (f) Pictorial representation of the non-crosslinking colorimetric method for distinguishing between single-stranded and double-stranded oligonucleotides using unmodified AuNPs under high salt conditions.[295] (g) Mixing a positively charged polyelectrolyte with ssDNA/aptamer causes gold nanoparticle aggregation and a noticeable color change. In contrast, the addition of this polymer to folded DNA does not induce a color change.[296] (a) Reprinted with permission from ref. 289. Copyright 2005 American Chemical Society. (b) and (c) Reprinted with permission from ref. 292. Copyright 2013 American Chemical Society. (d) Reprinted with permission from ref. 293. Copyright 2006 American Chemical Society. (e) Reproduced from ref. 294 (2011) with permission from the Royal Society of Chemistry. (f) Reprinted with permission from ref. 295. Copyright (2004) National Academy of Sciences, U.S.A. (g) Reprinted with permission from ref. 296 (2010).

unmodified AuNPs, and a positively charged polyelectrolyte known as poly[(9,9-bis(6′-*N*,*N*,*N*-trimethylammonium) hexyl) fluorene-*alt*-1,4-phenylene] bromide (PFP-Br). In this system, the polyelectrolytes preferentially bind to ssDNA rather than double-stranded or folded DNA. This preferential binding prevents the ssDNA from stabilizing the unmodified AuNPs, thus resulting in an aggregation color change (Fig. 32f and g). When aptamers are used as ssDNA, the resulting colors depend on whether the target molecule folds the aptamer. This approach can detect a range of analytes such as oligonucleotides, thrombin, cocaine, and mercury ions. The detection limit is 1.25 pM for DNA; nonetheless, the complexity of real samples induces non-specific absorption, which could compromise the detection results.

While nucleic acid testing methods like PCR remain the gold standard for SARS-CoV-2 diagnosis and mass COVID surveillance, AuNP-based technologies, such as colorimetric LFA and face coverings, have also been developed and run parallel for viral DNA detection during pandemic. Confirmation of SARS-CoV-2 infection involves the combined detection of the E and ORF1ab, N, or S regions. For example, Pan *et al.* developed a rapid point-of-care LFA-based nucleic acid test (NAT) for diagnosing positive COVID-19 cases without the need for RNA extraction and amplification.[302] The test utilizes 6-carboxyfluorescein (6-FAM) and biotin-labeled antisense oligonucleotides (ASOs) designed to target the N-gene sequence of SARS-CoV. After amplification, the viral DNA is mixed with FAM and biotin-labeled ASOs, ensuring DNA unfolding and optimal hybridization with the ASO strands. The resulting mixture is then added to a lateral flow strip. As the sample flows through the strip, the test line (T) immobilized with anti-FAM antibody captures the assembly using the FAM-labeled ASO 2. Additionally, the biotin-labeled ASO 1 attracts streptavidin-coated gold nanoparticles, resulting in the formation of a faint red T line (Fig. 33a). The reported detection limit for the N gene is 0.02 copies per μl within a 10-minute timeframe.

To shorten the time for viral gene amplification in clinical samples, Tan *et al.* demonstrate a one-pot direct reverse transcript loop-mediated isothermal amplification (RT-LAMP) assay for SARS-CoV-2 using a colorimetric LFA (Fig. 33b–d).[303] The

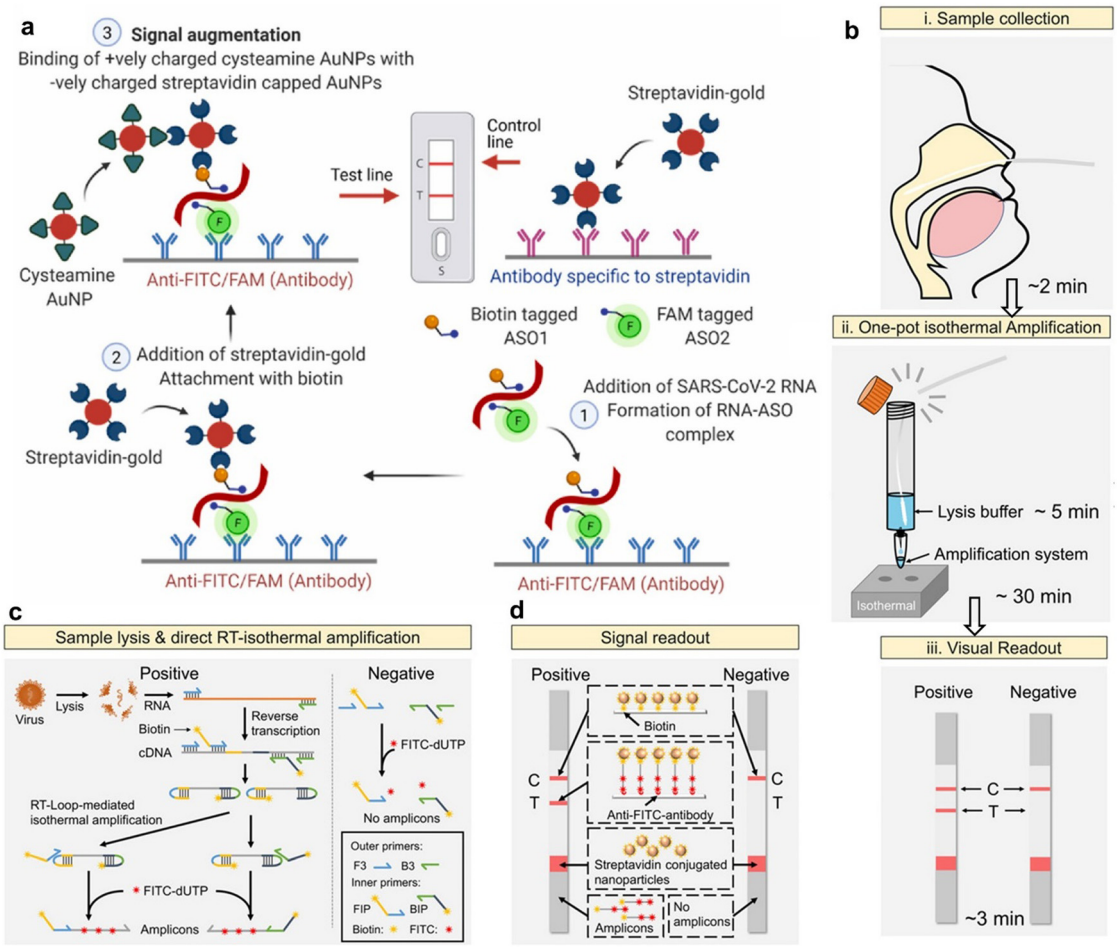

Fig. 33 Color detection of SARS-CoV-2 oligonucleotides based on LFA. (a) Illustration of the working principle of the nucleic acid-based lateral flow assay using ASO.[302] (b)–(d) Workflow for SARS-CoV-2 detection using the RT-LAMP-LFA system. Principle of direct reverse transcription loop-mediated isothermal amplification (RT-LAMP) amplification and visual detection using the lateral flow assay.[303] (a) Reproduced with permission from ref. 302. Copyright 2022 Elsevier. (b)-(d) Reproduced from ref. 303 in accordance with CC BY-NC-ND 4.0. Copyright 2021 American Chemical Society.

entire workflow, from sample to answer, is completed within 40 minutes without the need for professional instruments or technicians. The detection limit for ORF1ab and N genes is 40 copies per μL, and importantly, the RT-LAMP achieves a 100% total accuracy when analyzing clinical RNA samples. Recently, Zhou *et al.* modified a CRISPR/Cas9-mediated TL-LFA combined with multiplex RT-RPA for simultaneous detection of dual-gene targets (E and Orf1ab genes) of SARS-CoV-2.[304] Cas9/sgRNA was used for DNA recognition and bridging of AuNP-DNA probes, which bind to the biotinylated amplicons specifically recognized by the Cas9/sgRNA complex. The test exhibited a sensitivity of 100 RNA copies per reaction (25 μL). Analysis of 64 clinical samples showed 100% negative predictive agreement and 97.14% positive predictive agreement.

The nanoamplified colorimetric test described by Pan *et al.* utilizes plasmonic AuNPs coated with two antisense oligonucleotides (ASOs) as a reporter for detecting amplified nucleic acid from SARS-CoV-2, the causative virus of COVID-19 (Fig. 34a).[305] The ASOs specifically target the N-gene of SARS-CoV-2, and binding to the target sequence induces aggregation of the gold nanoparticles, resulting in a change in their plasmonic coupling and therefore color change. Clinical sample testing demonstrated high accuracy (>98.4%), sensitivity (>96.6%), and specificity (100%), with a detection limit of 10 copies per μL. This versatile test can be easily adapted for diagnosing other viral infections by modifying the ASOs and primer sequences. James *et al.* developed a portable and textile-functionalized system with freeze-dried, cell-free synthetic circuits including CRISPR-based tools, for *in situ* detection of SARS-CoV-2 oligonucleotides in exhaled aerosols on a face-covering.[306] The colorimetric sensor was activated upon rehydration and then reported the presence of SARS-CoV-2 RNA targets. Specifically, the optimized Cas12a SHERLOCK sensor in the μPAD reaction zone enables trans-cleavage of a co-lyophilized FAM-biotin ssDNA probe, which is detected using the anti-FITC conjugated AuNPs in an integrated LFA strip for a visual readout (Fig. 34b). The sensors exhibit a limit of detection of 500 copies (17 aM) of SARS-CoV-2 IVT RNA, comparable to standard laboratory-based RT-PCR assays endorsed by the World Health Organization. Li *et al.* developed an inexpensive assay ($0.30 per test) for the rapid colorimetric

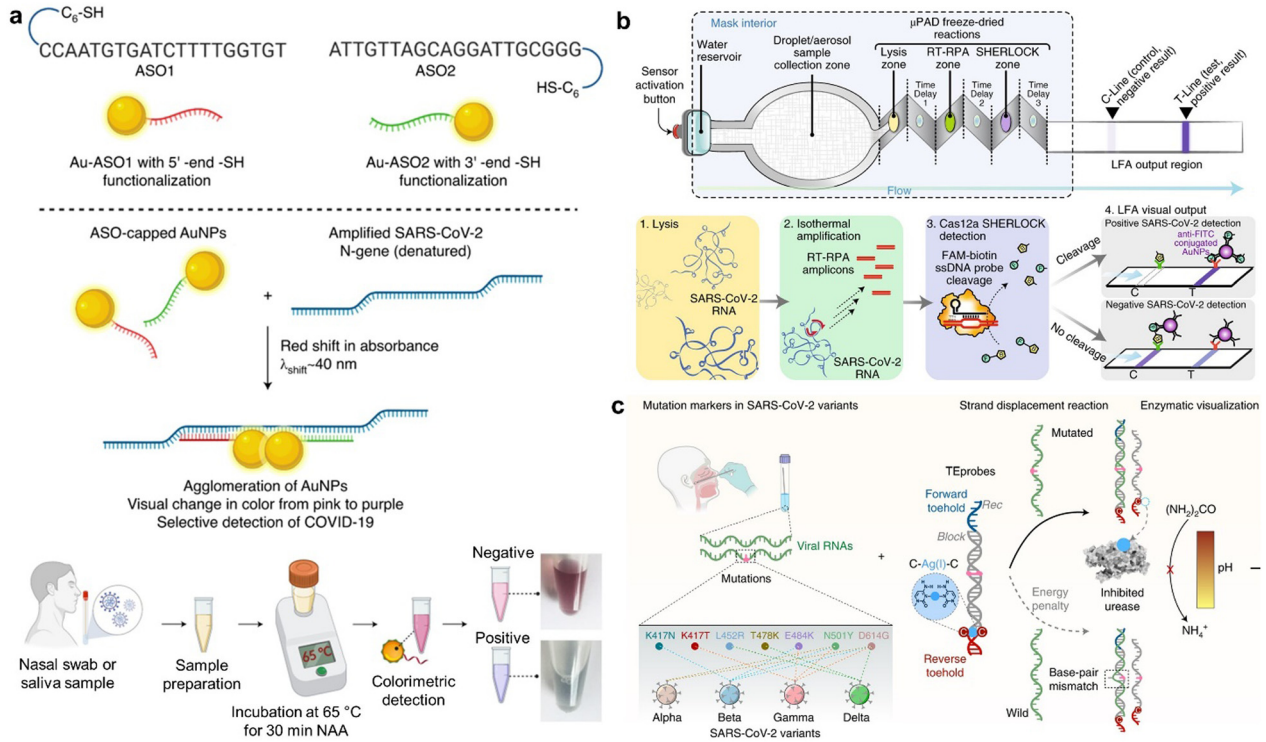

Fig. 34 Color detection of SARS-CoV-2 oligonucleotides based on portable mask. (a) Illustration of the hybridization process between ASO-conjugated AuNPs and the complementary target gene sequence, enabling colorimetric, naked-eye detection of SARS-CoV-2.[305] (b) Schematic representation of the sensor components integrated into a face-mask-based wearable diagnostic for SARS-CoV-2. Upon puncturing the buffer blister reservoir, viral particles from the wearer's respiration are transported through a wicking material to freeze-dried reactions within a μPAD device. The final visual output is obtained using an externally passed LFA strip.[306] (c) Development of foldable COVID paper strips utilizing nucleic acid strand-displacement reactions, thermodynamic energy penalty resulting from single-base-pair mismatches, and metal-ion-controlled enzymatic cleavage of urea to enhance the recognition of viral RNAs. The colorimetric readout is *via* pH changes.[307] (a) Reproduced with permission from ref. 305. Copyright 2021 Nature. (b) Reproduced with permission from ref. 306. Copyright 2021 Nature. (c) Reproduced from ref. 307 in accordance with CC BY 4.0. Copyright 2022 Wiley.

detection of SARS-CoV-2 variants within 30 min.[307] Instead of AuNP colorant, they utilized pH paper as the color readout. Specifically, by employing a precisely designed double-stranded DNA probe known as the TEprobe, they were able to control the thermodynamic energy of the strand displacement reaction induced by input RNAs through adjustments in its terminal forward and reverse toehold sequences. This control enabled differentiation between mutated and wild viral RNAs based on the thermodynamic energy penalty arising from single-base-pair mismatches. The recognition of viral RNAs triggered the release of Ag(I), a metal ion serving as a urease inhibitor, thus facilitating the regulation and amplification of urea cleavage and NH^{4+} levels (Fig. 34c). Utilizing this tool, they were able to visualize key mutation markers of SARS-CoV-2 variants, such as Alpha, Beta, Gamma, and Delta, through distinct pH values.

6.4 Peptide and protein

Colorimetric measurement for proteins is essential for disease identification and monitoring, enabling early diagnosis and disease management. Traditional colorimetric assays like Bradford, Lowry, Biuret, and bicinchoninic acid measure total protein levels but lack specificity. ELISAs are excluded in this review. In this subsection, we briefly discuss nanotechnology-based colorimetric detection for representative peptides, proteins, and antibodies.

6.4.1 Amyloid-β peptide. The recognition mechanisms for peptides include metal coordination, π-stacking, coiled-coil, or antibody-peptide interactions, enabling diverse nanotechnology-based colorimetric assays.[308–310] The presence of Aβ aggregate in cerebrospinal fluid, serum, or retina is associated with an increased risk for Alzheimer's disease (AD), although the role of Aβ as a definitive biomarker for predicting AD onset is still under research and debate.[309,311] While most Aβ probes including curcumin derivatives use fluorescence for *in vivo* applications,[312] a few studies employ *in vitro* colorimetric strategies. For example, Xu *et al.* discovered a simple colorimetric assay based on the favorable interaction between Aβ40 and AuNPs, facilitated by the hydrophobic interaction between peptide amino groups and anionic nanosurfaces.[313] Cu^{2+} effectively binds with Aβ through coordination, leading to AuNP aggregation by bridging separate Aβ strands, causing a color change from wine red to blue (Fig. 35a). The assay has a detection limit of 0.6 nM for Aβ40, within the clinical range of 0.4 to 1.5 nM. Building upon this sensing mechanism, Mahmoudi *et al.* employed additional AgNPs as color agents, enabling their sensor array to discriminate between Aβ42, Aβ40, and human serum albumin within the range of 50 nM to 500 nM, including their mixtures.[314] Lee *et al.* introduced a

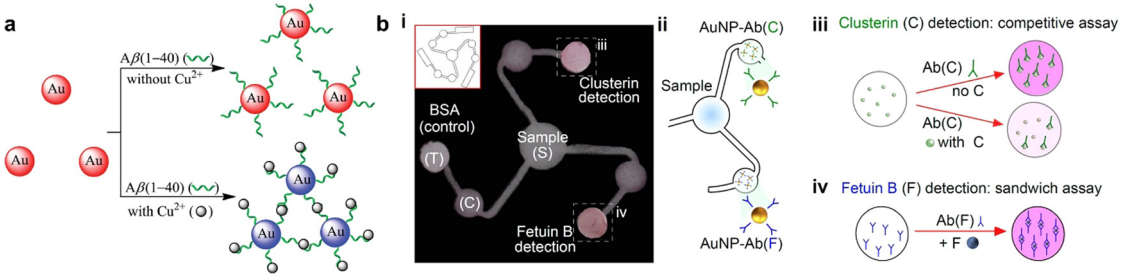

Fig. 35 Colorimetric detection of peptide and protein biomarkers. (a) Schematic illustrations showcasing the colorimetric mechanism of AuNP-based detection of Aβ40 upon addition of Cu^{2+}.[313] (b) Scheme of a lateral flow paper device designed for detecting clusterin and fetuin B, crucial markers for Alzheimer's disease detection.[316] (a) Reproduced with permission from ref. 313. Copyright 2015 Wiley. (b) Reprinted with permission from ref. 316. Copyright 2019 American Chemical Society.

real-time colorimetric assay that monitors the molecular assembly of Aβ monomers, utilizing AuNPs as nucleation sites and colorimetric reporters. This assay allows for easy detection of aggregation kinetics at physiologically relevant micromolar concentrations and offers a convenient approach for high-throughput drug screening in AD and optimizing Aβ aggregation prevention dosage once Aβ as a definitive AD biomarker is proved.[315] In addition to nano-based coloration, the synthetic dye CRANAD-2 changes from colorless to purple with Aβ aggregates due to favored hydrophobic interactions (K_d near 38 nM) and altered dye dispersity in aqueous solution.

6.4.2 Proteins. Colorimetric protein measurement is essential for diagnostics. One example of a 36.7 kDa hCG LFA is the Abbott TestPack Plus hCG urine assay, introduced by Osikowicz *et al.* in 1990, which employed colloidal selenium nanoparticles.[317] The mechanism involves the capture of colloid-labeled anti-α-hCG antibodies (or primary antibodies) at the test line immobilized with anti-α-hCG antibodies, resulting in color staining from the selenium nanoparticles, while the control line immobilized with the anti-β-hCG/hCG complex (or secondary antibodies) captures any colloidal conjugates.[318] However, with an LoD of 50 mIU mL^{-1}, this test lacked sensitivity for detecting early-stage pregnancies, only becoming effective at later stages. In 2006, Tanaka *et al.* developed a urine hCG LFA using gold conjugates, resulting in enhanced sensitivity (1 pg mL^{-1}) due to the localized surface plasmon resonance of the gold nanoparticles, leading to intensified color formation at the test line.[319]

Insulin, a blood glucose-regulating hormone, should be below 25 mIU L^{-1} in healthy individuals. However, those with diabetes often have inadequate insulin production, leading to high blood glucose levels even after meals.[320] Combining an insulin detection device with glucose monitoring can significantly enhance diabetes patient care, ensuring optimal treatment outcomes. A recent POC assay system (SelexOn, Osang Healthcare Inc., Anyang-si, Korea) based on colorimetric LFA technique comprises a cartridge employing a rapid sandwich immunoassay with AuNPs attached to a capture antibody, and a POC analyzer that interprets information and enables densitometric analysis using a built-in camera; however, the range of this LFA for insulin and connecting peptide (C-peptide) in whole blood samples was limited (218.1–275.72 pmol L^{-1}) and further optimization is required to cover a broader range before clinical implementation.[321]

Measuring fetuin B, clusterin, and tau as protein biomarkers has gained increasing interest in Alzheimer's disease diagnosis. Zucolotto *et al.* developed a paper-based POC device that immobilizes selective antibodies on AuNPs, allowing lateral flow of biofluid towards the selective antibody, resulting in AuNP-Ab accumulation on the test zone and a color change from white to pink (Fig. 35b). The detection limit is 0.24 nM for fetuin B and 0.12 nM for clusterin, both well below the clinically relevant range.[316]

Native pathogen proteins and cytokines serve as common protein biomarkers associated with disease infection. In the case of SARS-CoV-2, native pathogen proteins like the N or S-protein act as antigen targets for biosensing. Antigen detection is crucial in the early stage of SARS-CoV-2 infection when nucleic acid tests are negative, and antibodies are undetectable. LFAs for antigen detection operate on the principle of the double-antibody sandwich method, similar to the hCG (pregnancy) LFA test, and require the specific antibody pairs to be identified. Kim *et al.* employed phage display technology and ELISA to screen single-chain variable fragment (scFv)-crystallizable fragment (Fc) fusion proteins as specific antibodies. These antibodies were then used on a cellulose nanobead-based LFIA platform.[322] The newly developed scFv-Fc antibodies exhibit specific binding to the SARS-CoV-2 N-protein with a detection limit of 2 ng in 20 min. Loading the sample onto the platform results in the formation of a double-antibody sandwich complex in the test region, capturing the N-protein antigen. In addition to LFA techniques, Timur *et al.* developed a dot blot nanodiagnostic platform for detecting the SARS-CoV-2 spike protein (S-protein). The platform utilizes immobilized primary Anti-S protein antibody and various primary antibody functionalized color agents such as AuNPs, silver coated AuNPs, and dye-loaded polymersome. The detection limit achieved by the dye-polymersome is 0.11 ng mL^{-1}.[323] However, the presence of viral variants increases the risk of false-negative detection based on S-protein detection. Zhou *et al.* devised a colorimetric sandwich-type bioassay using a human ACE2 (hACE2)-based peptide pair as an alternative to S-protein antibodies.[324] This peptide pair was inspired by the interactions between hACE2 and the viral S

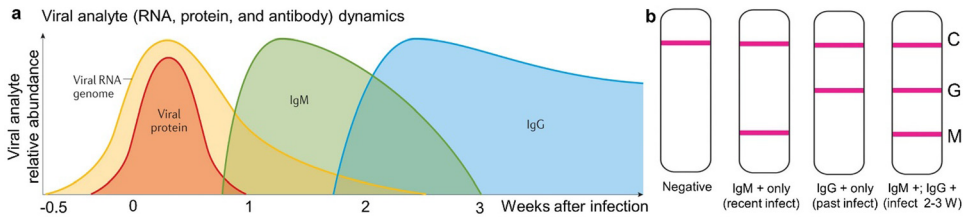

Fig. 36 Antibody LFAs for COVID detection. (a) After infection with SARS-CoV-2, the RNA genome peaks at symptom onset, while viral proteins increase rapidly in a shorter timeframe. The body responds with IgM and IgG antibodies, persisting for weeks to months.[328] (b) LFA cassettes with various tested results indicate the infectious stage. (a) Reproduced with permission from ref. 328. Copyright 2021 Nature.

protein during viral entry. Remarkably, the bioassay enabled the sensitive detection of S-protein at levels as low as 0.01 nM (0.26 ng mL^{-1}) in SARS-CoV-2 variants.

6.4.3 Antibodies. Colorimetric antibody test based on LFA serological (blood) assay detects the presence of antibodies (IgG, IgM, and IgA) produced by the immune system in response to disease infection (Fig. 36a).[325] For example, newer systems targeting SARS-CoV-2 require finger prick blood samples or nasal swab. Ye *et al.* optimized and tested a rapid point-of-care lateral flow immunoassay that simultaneously detects IgM and IgG antibodies against SARS-CoV-2 in human blood within 15 min.[326] The test strip has two lines: one for IgM and one for IgG, with mouse anti-human monoclonal antibodies. Colloidal AuNPs with a SARS-CoV-2 antigen bind to the testing antibodies. IgM binds to the M (IgM) line, IgG binds to the G (IgG) line, and no antibodies yield no lines. The test results indicate (Fig. 36b): No IgM or IgG – no COVID-19; IgG (no IgM) – past infection; IgM (no IgG) – active antibodies (recent infection); Both IgM and IgG – active antibodies to a previous infection (likely 2–3 weeks).[327] A typical detection limit for antibodies falls within the ng mL^{-1} range.[325]

6.5 Enzyme and protease

Enzymes are key participants in various biological processes, both normal and disease-related, including cancer, stroke, infection.[329] Proteolytic activity is utilized as a marker for disease progression and therapeutic monitoring. For example, dysregulated matrix metalloproteases (MMPs) and cysteine cathepsins activities contribute to tumor progression, invasion, and metastasis.[330] Caspase-3 participates in programmed cell death.[331] Gingipains from *Porphyromonas gingivalis* contribute to periodontal disease and systemic inflammation.[332] Granzymes are the molecular executors of immune-mediated cytotoxicity.[333] Lysosomal proteolysis is used for protein degradation and trigger release of antibody–drug conjugates featuring non-cleavable linkers, leading to the liberation of the drug bound to the conjugated amino acid.[334] Lipases, amylases, and decarboxylases have a great impact on food processing, quality control, and spoilage. Colorimetric systems involving enzymes focus on either targeting enzymes as analytes or using enzymes as amplification tools, often in conjunction with their specific substrates. In this section, we exclude the use of enzymes as reporter amplification, such as the pairs of HRP-TMB or alkaline phosphatase-BCIP/NBT in ELISA, GOx-glucose-TMB in glucose detection, the urease-urea-pH strip in LFAs,[307] and recent CRISPR/Cas9-DNA pair in DNA assays.[306] Instead, we focus on directly measuring the autocatalytic activity of enzymes based on detection mechanisms such as dye separation, modulation of nanoparticle diversity, and nanoparticle growth (Table 8).

6.5.1 Dye desorption. A few commercially available colorimetric enzyme assays use substrates for recognition and dye colorants for signaling through surface adsorption/desorption. For example, the amylase test is a colorimetric assay for detecting amylase in biological samples like saliva or semen. The Phadebas® tablets and forensic paper use a cellulose substrate and starch nanoparticles linked with blue dye.[349] α-Amylase breaks the α-1,4-glucosidic linkage, releasing blue dye to detect saliva or semen in crime scene samples (Fig. 37). Jokerst *et al.* modified this colorimetric assay and investigated respiratory droplet interactions with face coverings using aerosolized saliva biomarkers.[183] They found 3 times higher α-amylase levels in worn neck gaiters and surgical masks compared to N95 respirators, mainly on the inner layer (96% on the inner layer and 4% in the middle layer). A diagnostic test strip for α-amylase was further developed and validated based on the amylase forensic paper. Additional colorimetric amylase substrates include the hydroxyproply-β-cyclodextrin-curcumin host–guest complexes. Other commercial enzyme tablets like tetramethylbenzidine tablets are used for peroxidase activity detection in biological samples.[350] These methods all focused on manipulating how dye colorants bind and release from surfaces in the presence of specific substances of interest. They utilized biocompatible nano/micro-scale frameworks, like conjugatable polymers, MOF, polystyrene NPs, magnetic beads, coacervates, and calcium carbonate particles, to achieve this.

6.5.2 Nanoparticle dispersity. Modulating nanoparticle dispersity through enzymatic activation is an alternative mechanism for colorimetric detection of enzyme activity. Strategies to manipulate plasmonic coupling are categorized into covalent chemistry (or crosslinking) and physical factors (or non-crosslinking), involving a variety of interparticle interactions. Scrimin *et al.* initially employed dithiol-appended substrates [Cys–$(Xaa)_n$–Cys, where Xaa is arbitrary amino acids] to chemically crosslink AuNP aggregates for the colorimetric detection of thrombin, achieving a detection limit of less than 5 nM in 90 min.[335] This approach can be adapted for other proteases and nanoparticles. Subsequent studies demonstrated that

Table 8 Color-based enzyme detection by activatable systems

Mechanism	Interactions	Key elements or substrate	Enzyme	LoD, time	Comments	Ref.
Dye disassociation	Covalent	Glucosidic linkage	Amylase	N/A	Amylase releases blue dyes from the starch microsphere	183
Crosslinking NP aggregation	Au–S	Cys–$(Xaa)_x$–Cys	Thrombin, lethal factor	5 nM, 90 min	Dithiol peptide aggregates spherical AuNPs	335
			Trypsin	0.47 nM, 30 min	Dithiol peptide aggregates slice-like Ag/AuNPs	336
		$(Cys)_2$-$(Xaa)_x$-$(Asp)_3$	M^{pro}	18.9 nM, 10 min	Dithiol fragment crosslink AuNPs	131
	Coordination	His_6–$(Xaa)_x$–His_6	MMP-7	10 nM, 1 h	Histidine crosslink AuNPs	337
	Covalent	Thiolamino and cyanobenzothiazole groups	Legumain	N/A	Enzyme cleavage exposes thiolamino group for click cycloaddition	128
	Au–S and electrostatic	Sphingomyelin-based liposomes encapsulated with cysteine	Sphingomyelinase	1.4 pM	Enzyme destroy liposome and release cysteine for crosslinking AuNPs	338
Non-crosslinking NP aggregation	Electrostatic	Phosphate group	Intestine alkaline phosphatase (CIALP)	16 nM	Enzyme converts ATP to adenosine and reduces the charge valence	339
		Cys-Tyr(PO_3^{2-})-Arg	ALP	0.3 μM, 4 min	Enzyme cleave the Tyr(PO_3^{2-}) and imbalance the charge	340
		$(Asp)_n$-$(Xaa)_x$-$(Arg)_m$	Mpro	10 nM, 10 min	The cleaved Arg fragment aggregates the BSPP-AuNPs	16
				0.5 nM	The cleaved Arg fragment aggregates the BSPP-AgNPs	20
		$(Asp)_n(Glu)_o$-$(Xaa)_x$-$(Arg)_m(Lys)_p$	SV3CP	28 nM, 10 min	The cleaved Arg/Lys fragment aggregates the BSPP-AuNPs	134
		$[EG]_8$-$(Xaa)_x$-RGD-$[EG]_5$-Cys	MMP-9	N/A	Enzyme cleaves the PEG, and exposes RGD for interparticle association	341
	π–π stacking	$(Asp)_n$-$(Xaa)_x$-$(Phe)_m$	Mpro	20.8 nM, 10 min	The cleaved FFPC fragment aggregates the AuNPs	342
NP disassociation	Electrostatic	Arg_6	Trypsin	1.6 ng mL^{-1}	Enzyme reduces the charge valence of substrate, preventing citrate-AuNP aggregation	343
		Arg-$(Xaa)_x$-Arg	Mpro	20 nM	Enzyme reduces the charge valence of substrate, redispersing TPPTS-AuNP aggregates	109
		Lys-$(Xaa)_x$-Lys	SV3CP	250 nM, 48 h	Enzyme reduces the charge valence of substrate, redispersing DPPS-AuNP aggregates	
	π–π stacking	Fmoc-$(Xaa)_x$-Cys	Thermolysin	90 ng mL^{-1}	redispersion of aggregated AuNPs due to proteolytic removal of F-moc group	344
	Au–S	$(Arg)_m$-PEG-SH	Trypsin	100 pM	Enzyme releases PEG-SH fragment, which redisperse the AuNP aggregates	345
			RgpB	100 pM, 2 h	Enzyme releases PEG-SH fragment, which redisperse the BSPP-AgNP aggregates	346
NP growth	Electrostatic	Tyr(PO_3^{2-})-Arg	ALP	N/A	Enzyme releases positively charged dephosphorylated peptides, leading to aggregative growth	347
	Au–S	Cys–$(Xaa)_x$–Cys	Trypsin	45 pM	Enzyme doubles the thiol amount for surface passivation and impedes the NR growth	348

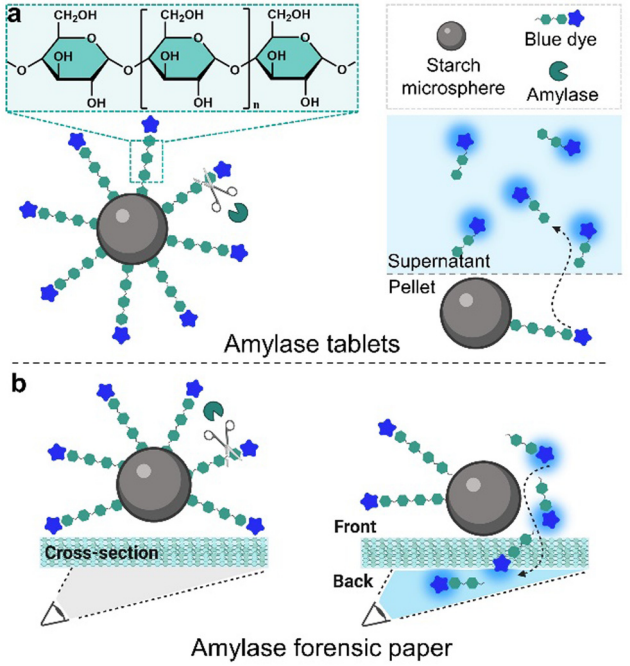

Fig. 37 Color detection of amylase. Mechanistic representation of amylase reagent (top) and forensic paper test (bottom). α-Amylase digests the α-1,4-glucosidic linkage and releases the blue dyes from the starch microsphere, producing colorimetric signals.[183] Reproduced with permission from ref. 183. Copyright 2021 American Chemical Society.

slice-like gold-silver core–shell nanoparticles exhibited the strongest colorimetric response and increased spatial separation of dithiol in the peptide crosslinker reduced plasmonic coupling and color changes.[336] Replacing cysteine-thiol with histidine-imidazole also enables nanoparticle crosslinking due to the strong coordination between the imidazole group and metallic surfaces. Kim *et al.* used carboxy AuNPs and peptides flanked with hexahistidine [His_6–$(Xaa)_n$–His_6] through metal-affinity coordination, achieving a detection limit of 10 nM for MMP-7 within 1 h (Fig. 38a).[337] While effective in enzyme level detection, the conventional dithiol flanking design of nanoparticle assembly suffers from the absence of hydrophilic domains necessary to maintain a balance between water solubility and responsiveness. Our group improved the peptides with a novel formula [$(Cys)_2$-$(Xaa)_n$-$(Asp)_3$] to facilitate the assembly of AuNPs and enhance their performance in aqueous environments (Fig. 38b).[131] The intact substrate probe stabilizes the AuNPs in the absence of protease due to the Asp solubilizing group, while the AuNPs aggregate after probe being cleaved by protease. They also demonstrated that di-cysteine is the optimal crosslinking unit by varying the number of cysteines. This system was validated for nanoplasmonic sensing of the recombinant SARS-CoV-2 main protease (M^{pro}), achieving a detection limit of 18.9 nM in a spiked exhaled breath matrix. This detection limit could be above the clinically relevant level of M^{pro} (<160 pM) in patients' exhaled breath condensate without protease amplification techniques. Overall, the thiol-to-metal based crosslinking strategy necessitates moderate surface passivation and an exposed core for thiolate substrate coordination.

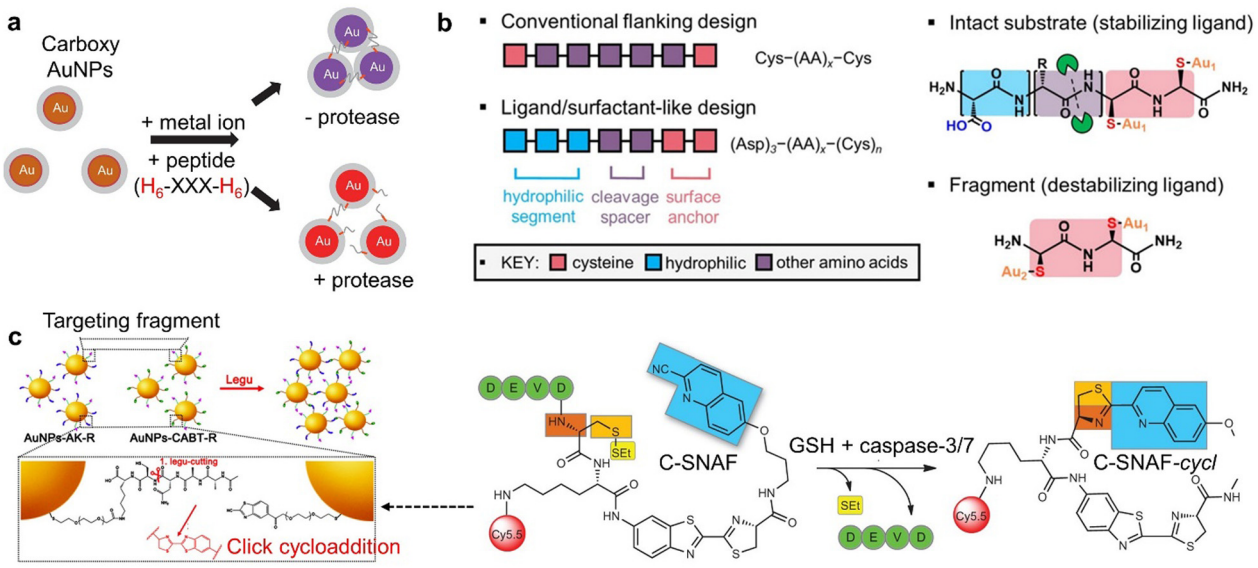

Fig. 38 Color detection of protease based on covalent crosslinking. (a) Schematic illustration of a carboxy-protected AuNP-based colorimetric assay for proteases using designed His_6-ended peptides and metal ions.[337] (b) In the conventional flanking design (top), the peptide head and tail are modified with a cysteine. The novel peptide design consists of three modules: the surface anchor, the cleavage site, and the hydrophilic segment (bottom). The intact peptide stabilizes AuNPs while the protease-cleaved fragment aggregates the AuNPs, giving color changes.[131] (c) Molecular mechanism of the legumain-activated click cycloaddition and aggregation process of AuNP-A&C-R. The click cycloaddition reaction between free cysteine and cyanobenzothiazole is given in the right panel.[128,351] (a) Reproduced with permission from ref. 337. Copyright 2013 Elsevier. (b) Reprinted with permission from ref. 131. Copyright 2022 American Chemical Society. (c) Reprinted with permission from ref. 128. Copyright 2017 American Chemical Society. Reproduced with permission from ref. 351. Copyright 2014 Nature.

Alternatively, covalent coupling of surface ligands is a crosslinking mechanism that requires a highly compact ligand layer with terminal functional groups. Gao *et al.* introduced dual-functional AuNPs to enhance their accumulation in glioblastoma multiforme (Fig. 38c).[128] The AuNPs, named AuNP-A&C-R, consisted of two distinct functional particles: Ala-Ala-Asn-Cys-Asp (AK) and R8-RGD-comodified AuNPs (AuNP-AKR), as well as 2-cyano-6-amino-benzothiazole (CBT) and R8-RGD-comodified AuNPs (AuNP-CABT-R). In the presence of legumain, AuNP-A&C-R exhibited aggregation properties due to the cleavage-generated thiolamino group, allowing click cycloaddition with cyanobenzothiazole under physiological conditions, as previously reported by Rao *et al.*[351]

Non-crosslinking colorimetric systems alter physical factors and thereby affecting NP dispersity, and the selectivity is ensured by enzyme-substrate recognition. For instance, NPs stabilized by electrostatic double layer repulsions tend to aggregate when an excess of counterionic residues is introduced. This aggregation occurs due to a charge screening effect and follows the Schulze–Hardy rule.[110] The Schulze-Hardy rule enables colorimetric enzyme detection through strategic modification of substrate electrophoretic properties, such as charge reversal and valence alternation. For example, Li *et al.* developed a colorimetric assay to monitor an enzymatic dephosphorylation process involving the conversion of adenosine 59-triphosphate (ATP) to adenosine using calf intestine alkaline phosphatase (CIALP).[339] The observed aggregation is caused by negatively charged ATP phosphates adsorbing on AuNP surfaces, increasing their colloidal stability. In contrast, adsorption of enzymatic products like uncharged nucleosides (*e.g.*, adenosine and inosine) leads to AuNP aggregation by reducing surface potential (Fig. 39a). The detection limit for CIALP is 0.16 units/20 mL (~16 nM).

Colorimetric detection of ALP can also rely on a short phosphorylated peptide, Cys-Tyr(PO_3^{2-})-Arg, developed by the Tung group.[340] The phosphate group prevents binding between the guanidine group (Arg side chain) and AuNPs, leaving Cys to

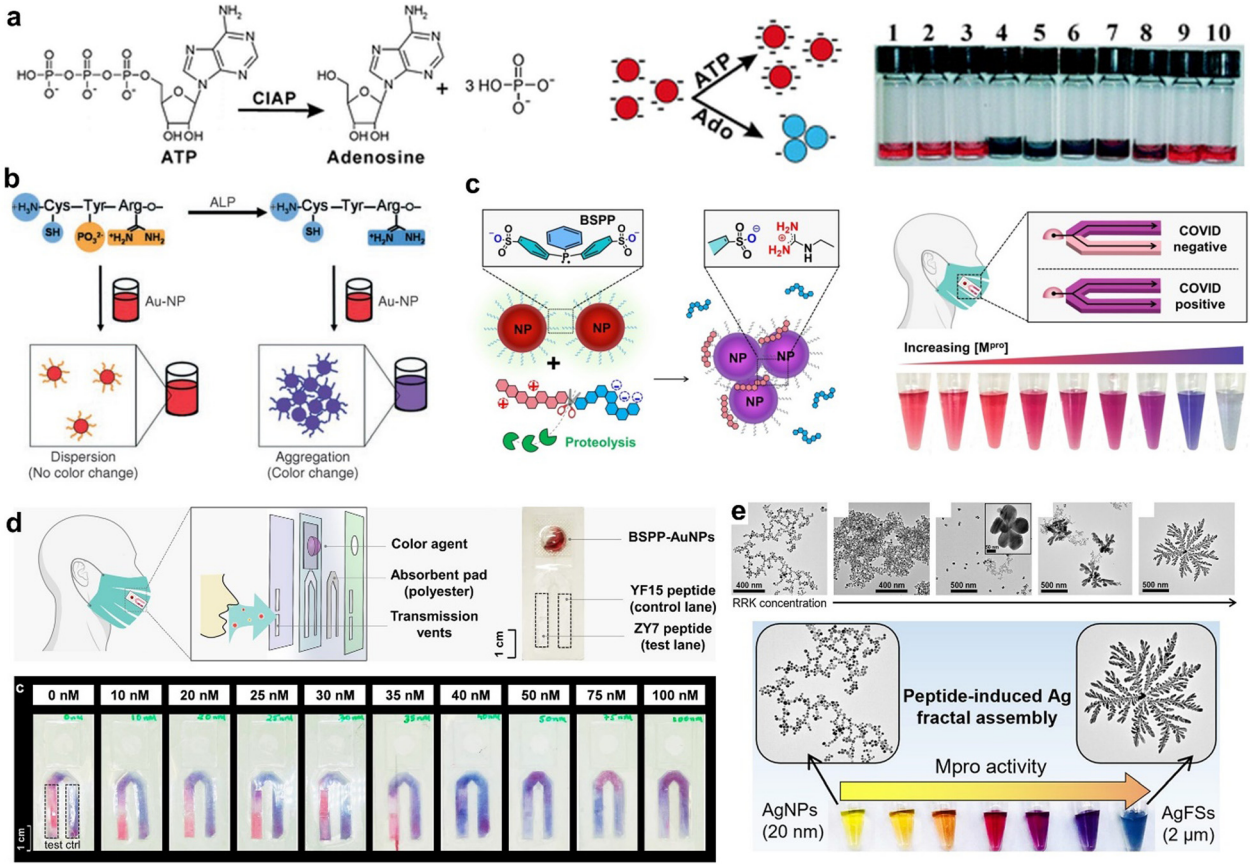

Fig. 39 Color detection of protease based on NP aggregation. (a) Chemical conversion of ATP into adenosine by CIAP reduces the negative charge. Photographs show AuNP solutions containing 60 mM ATP, ADP, AMP, inosine, and adenosine (vials 1–5). Vials 6–10 are the AuNPs with 30, 20, 10, 5 and 2.5 mM adenosine.[339] (b) The ALP assay uses peptide-induced AuNP aggregation, with phosphotyrosine acting as an aggregation switch. The phosphate group prevents arginine-AuNP binding, enabling interaction with gold by cysteine. Enzymatic hydrolysis removes the phosphate, leading to AuNP aggregation.[340] (c) Aggregation of BSPP-AuNPs caused by proteolytic hydrolysis of the zwitterionic peptide, reversing the net charge of intact peptide and its fragment. (d) A flow sticker on face covering for colorimetric M^{pro} sensing with an LoD of 30–40 nM. Pink-red: No M^{pro} or below detection; violet-blue: M^{pro} presence.[16] (e) Color changes due to fractal assembly of AgNPs and change of morphology in the presence of M^{pro} enzymatically releasing RR peptide.[20] (a) Reproduced from ref. 339 (2007) with permission from the Royal Society of Chemistry. (b) Reproduced with permission from ref. 340. Copyright 2007 Wiley. (c) and (d) Reproduced with permission from ref. 16. Copyright 2022 Wiley. (e) Reproduced with permission from ref. 20. Copyright 2022 American Chemical Society.

interact with gold. ALP cleavage at Tyr(PO_3^{2-}) allows Cys thiol to bridge with AuNPs, and Arg's positive charge triggers the colorimetric change (Fig. 39b). The detection limit for ALP is lower than 0.3 μM in 4 min. Jokerst *et al.* developed a charge-reversible peptide targeting the M^{pro} implicated in SARS-CoV-2.[16] The zwitterionic peptide [$(Asp)_n$-$(Xaa)_x$-$(Arg)_m$] releases positively charged $(Arg)_m$ moiety after cleavage, which leads to the assembly of negatively charged BSPP-AuNPs and color changes within 10 min (Fig. 39c and d). The limit of detection for M^{pro} in breath condensate was less than 10 nM. They also showed the assay's adaptability to a lateral flow sticker format and integration into portable point-of-care devices, including those attached to face coverings. This universal design can target other proteases by tuning the recognition sequence, and an example includes the Southampton norovirus 3C-like protease (SV3CP).[134] The charge-reversible substrate design can also be combined with AgNPs for improved sensitivity.[20] However, the color change is not due to NP aggregation but to fractal morphological alteration of spherical AgNPs caused by coalescence (Fig. 39e). This approach achieved an LoD of 0.5 nM and demonstrated the capability to visually distinguish a wide protease concentration range (1.25–30 nM). Electrostatically induced NP aggregation is rapid and sensitive; however, it is largely affected by impurities or additives in testing media. Alternatively, our group validated aromatic forces to induce the AuNP aggregation for colorimetric assays.[342] Surfactant-like peptides [$(Asp)_n$-$(Xaa)_x$-$(Phe)_m$] were designed that self-assemble into higher-order structures upon protease stimulation, resulting in NP aggregation and colorimetric readout. The observed plasmonic coupling results from the FFPC fragment's strong aggregation, forming micron fibers through aromatic stacking, which, in turn, establishes multivalent Cys thiol bridges with AuNPs. This system offers advantages over the electrostatic approach by working effectively in complex media with various electrolyte scavengers. The assay detects M^{pro} in exhaled breath condensate and saliva, with respective detection limits of 20.8 and 26.1 nM.

At the heart of NP dispersity and color change is surface chemistry, which determines colloidal stability, aggregation tendency, and impacts detection sensitivity. Researchers assessed the aggregation kinetics of AuNPs with various coatings in the presence of peptide aggregants (Fig. 40a–c).[118] The coatings cover a diverse range of ligands, varying from labile monodentate monomers to multicoordinating macromolecules. AuNPs coated with tannic acid and sulfonate phenolphosphine ligands showed the most favorable electrostatic-based aggregation due to their low molecular weight, compact size, high charge valence, and significant aromaticity. In contrast, AuNPs coated with citrate or polyvinylpyrrolidone performed best in dithiol-induced and π–π stacking interactions, typically featuring hard Lewis base-anchoring groups, resulting in weaker binding strength. The study also emphasized the importance of pairing low charge valence aggregating peptides with charged NPs of weak stability, or *vice versa*, for successful electrostatic-based sensors.

The NP core composition is another key component in colorimetric protease sensors and impacts visual sensitivity. Liedberg *et al.* evaluated plasmonic composition to enhance the visualization of subtle optical responses in nanoplasmonic bioassays, taking into account human color vision physiology.[51] The study showed that $Au_{0.8}Ag_{0.2}$ alloy NPs achieve semi-quantitative naked-eye detection of MMP-7 activity at concentrations five times lower than prior assays with AuNPs (Fig. 40d and e). The limit of detection was 0.082 μg mL^{-1} for $Au_{0.8}Ag_{0.2}$ compared to 1.25 μg mL^{-1} for AuNPs.

The NP aggregation-based colorimetric mechanism could be compromised by the complex composition of the medium, involving protein corona formation and substrate scavenging. In this case, NP-disassociation strategy could be complemented for protease detection in matrices. Zhang *et al.* discovered that the aggregation of citrate-AuNPs with Arg_6 substrate can be prevented by incubating Arg_6 with trypsin. They achieved an LoD for trypsin as low as 1.6 ng mL^{-1}. However, the *in situ* disassociation of the complexed AuNP-Arg_6 aggregates by trypsin was not evaluated in the study.[343] Jokerst *et al.* elucidated the mechanism underlying the disruption of plasmonic coupling as a consequence of charge valence induction.[109] They reported that the aggregation and dispersion behavior of AuNPs, driven by charged peptides, follows the Schulze-Hardy rule. The critical coagulation concentration (CCC) depends on the charge valency (Z) of counterions, with CCC proportional to Z^{-6}. This insight inspired the design of a new substrate [Arg-$(Xaa)_x$-Arg] for protease detection and the reduced charge valence break the plasmonic coupling (Fig. 41a). They also validated a reversible and *in situ* disassociation of AuNP-peptide aggregates by protease, where the color turned to pink at 20 nM of M^{pro}. The protease's interaction with aggregated AuNPs, in spite of spatial limitations and steric hindrance in non-directive peptide-AuNP complexes, remains an open question.

Klajn *et al.* proposed that the aggregates' dynamics, maintained by electrostatic interactions, allow for reorganization and exposure of the aggregants (peptide) to the surrounding solute (protease).[110] The plasmonic decoupling strategy induced by the break of charge valence is a universal design, which has also been validated in SV3CP detection.[352] In a previous study, Stevens *et al.* highlighted that AuNP-peptide aggregates, formed through aromatic interactions, can be dissociated by thermolysin enzyme.[344] The Fmoc terminated peptide ligand facilitates AuNPs aggregation owing to its strong aromaticity. Thermolysin cleavage releases Fmoc moieties and exposes amine groups, imparting a positive charge to NP surfaces, causing disassociation and color change (Fig. 41b). This approach reached a detection limit of 90 zg mL^{-1} for thermolysin. The disassociation of NP aggregates by good stabilizing ligands such as thiolate PEG is an alternative approach for colorimetric detection. The steric hindrance is not a limiting step for redispersing kinetics due to the small molecular weight and size of the stabilizing ligands. For example, upon cleavage of a charge-shielded HS-PEG-peptide conjugate, the HS-PEG fragment is released, exhibiting a higher affinity for the metallic NP surface.[345] This leads to the redispersion of the aggregated NPs and reversal color change (Fig. 41c and d). This strategy detects trypsin and gingipain (RgpB) at 100 pM in 2 hours using BSPP-AgNPs. The inclusion of PEG is beneficial

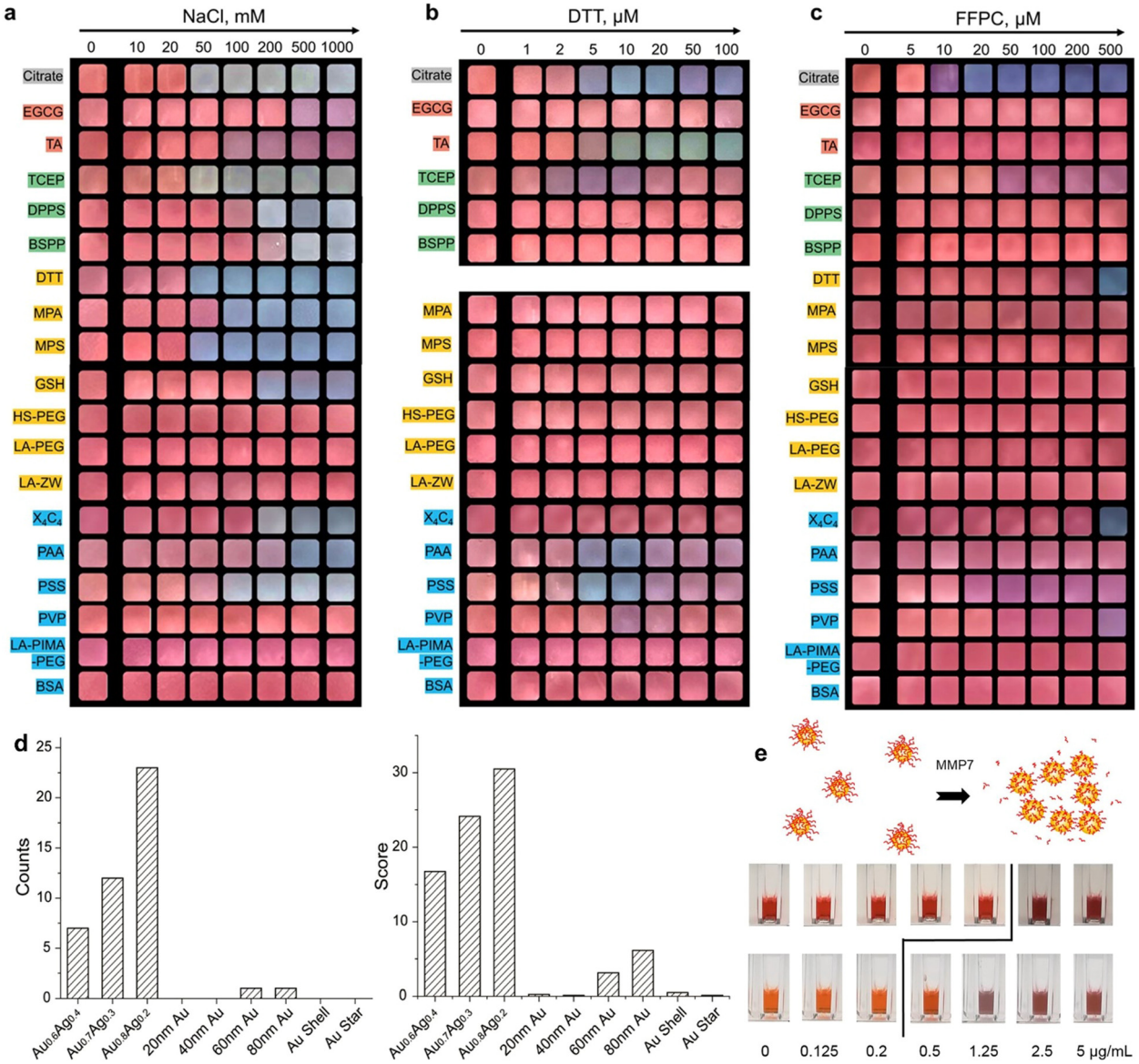

Fig. 40 Role of surface chemistry and core composition of NP in aggregation-based colorimetric assays. (a)–(c) Color patterns of the ligated AuNPs in a series of NaCl, dithiothreitol (DTT), and amphiphilic peptide (sequence: FFPC) solutions of increasing concentrations.[118] (d) The plasmonic nanoparticle samples scored with the most obvious color change against reflective index changes. (e) An illustration of a colorimetric MMP7 sensor with photos of AuNPs and $Au_{0.8}Ag_{0.2}$ at varying MMP7 concentrations.[51] (a)–(c) Reprinted with permission from ref. 118. Copyright 2023 American Chemical Society. (d) and (e) Reproduced with permission from ref. 51. Copyright 2018 American Chemical Society.

because the disassociation capability of HS-PEG remains unaffected in complex media.

The majority of dispersity-modulated colorimetric detections for enzymes adapt a stepwise procedure, *e.g.*, (i) incubation of enzyme with substrate, and (ii) NP introduction. The recognition and signaling steps are separated. Only a few studies used one-step detection where the enzyme-substrate recognition and nanoparticle aggregation/disassociation occur *in situ*. This requires the rationale design of coating ligand/substrate for good nanoscale recognitions on scaffolds (*e.g.*, NP,[341,353] antibody,[354] polymer,[355,356] biocondensate[357–359]), including optimized accessibility, homogeneity, orientation, and functionality. For example, Ulijn *et al.* demonstrated that enzymatic unveiling of surface-bound zwitterionic tetrapeptides through MMP-9 can activate the self-assembly of AuNPs.[341] They used PEG-peptide conjugates as surface ligands, with PEG serving as an entropic spacer for enzyme access to the peptide substrate and as steric hindrance to prevent self-assembly. Enzyme cleavage of the PEG exposes the charge-complementary RGD peptide, effectively assembling AuNP superstructures with electrostatic side-chain patterns. Nie *et al.* also employed a similar approach; however, they achieved the assembly of AuNPs through DNA hybridization after enzyme cleaving the surface-bound PEG-peptide ligands.[360] Other work emphasized the significance of a spacer in a one-step colorimetric sensor.[361] They conducted a comparison of substrate cleavage on the surface with and without a polyPro (P_x) domain.

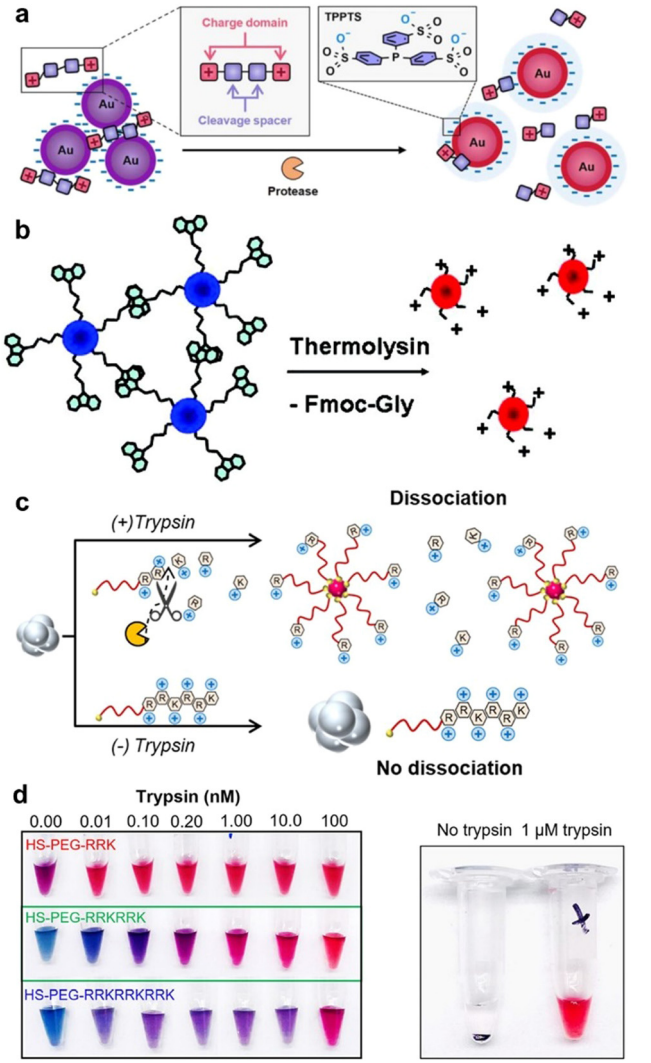

Fig. 41 Color detection of protease *via* NP-disassociation strategy. (a) Charge valence reduction by protease enables disassociation of aggregates and color change.[109,343] (b) Schematic illustration of the re-dispersion of aggregated AuNPs modified with protease-cleavable Fmoc-peptides.[344] (c) Proteolytic cleavage of peptide-PEG conjugates releases the stabilizing ligand HS-PEG, causing AuNP aggregate redispersion. (d) The photos illustrate the reversible transition of AuNP aggregates from black pellet to red dispersion induced by trypsin using peptide-PEG conjugates.[345] (a) Reproduced from ref. 343 (2011) with permission from the Royal Society of Chemistry. (b) Reprinted with permission from ref. 344. Copyright 2007 American Chemical Society. (c) and (d) Reprinted with permission from ref. 345. Copyright 2022 American Chemical Society.

By incorporating a zwitterionic peptide ligand with P_x, enzymatic cleavage was achieved, resulting in a decrease in surface potential, subsequent aggregation of AuNPs, and a corresponding color change. The detection limit was 2 to 5-fold higher than that of the sensor utilizing a stepwise method. This difference is likely attributed to the irregular enzymatic kinetics occurring at complex bio-NP interfaces.[362,363] Furthermore, the study validated similar findings with other proteases such as trypsin and MMP-14.

6.5.3 Nanoparticle growth. Modulation of NP growth is a less commonly reported mechanism for colorimetric protease detection. Aizawa *et al.* utilized the color development that occurs during the synthesis of AuNPs as an indicator of ALP activity using its substrate.[347] In the presence of ALP, the synthesis process resulted in aggregated Au nanostructures instead of well-dispersed violet nanostructures, attributed to positively charged dephosphorylated peptides. Others employed a dithiol peptide as a substrate for enzymatic modulation of nanorod growth.[336,348] Enzymatic dithiol peptide cleavage doubles the single thiolate concentration, slowing growth kinetics due to the strong affinity of single thiolate for Au surfaces and resulting in a distinct color compared to the non-cleaved assay. The limit of detection is 45 pM for trypsin.

6.6 Infectious pathogens

A colorimetric pathogen sensor identifies unique biomarkers (*e.g.*, pH, nucleotides, antigens, enzymes, metabolic byproducts, and exosomes) or detects whole pathogens.[364] Its processing time is faster than traditional methods like culture and counting, immunological assays, and PCR. This subsection briefly discusses color-based pathogen detection with target analytes and colorants.

6.6.1 Bacteria. Bacteria are unicellular organisms classified as either Gram-negative or Gram-positive. Examples of Gram-negative bacteria include *Escherichia coli* (*E. coli*), *Pseudomonas aeruginosa*, *Brucella abortus*, *Salmonella enterica*, and *Mycobacterium tuberculosis*, causing urinary tract infections, brucellosis, salmonellosis, and tuberculosis, respectively. Gram-positive bacteria like *Streptococcus pyogenes*, *Staphylococcus aureus*, and *Listeria monocytogenes* can cause pneumonia infections and listeriosis, respectively.[365] Sun *et al.* developed a portable paper-based band-aid (PBA) for detecting and treating drug-resistant bacteria.[366] The PBA relies on its acid response capacity using bromothymol blue. The study demonstrated an interaction between the drug-resistant bacteria (*E. coli*) and the PBA: In the case of drug-sensitive bacteria, the acidic microenvironment of the bacteria resulted in a color change of bromothymol blue from green to yellow (Fig. 42a). This acidic condition was attributed to the secretion of β-lactamase and nitrocefin from *E. coli*. This method also detected *E. coli* infections in mice wounds with a limit of 104 CFU per mL in 4 hours, confirming drug resistance. The study also discovered that Zr-MOF PCN-224 generates ROS under visible light (638 nm), damaging bacterial cell walls and reducing survival rates.

Nugen *et al.* developed a colorimetric assay for detecting *E. coli* by targeting the enzyme indicator β-galactosidase (β-gal) activity.[367] This assay involved the enzymatic reaction-induced silver deposition on the surface of AuNRs (Fig. 42b). The presence of β-gal triggered the hydrolysis of the substrate, producing p-aminophenol (PAP), which then reduced silver ions, forming a silver shell on AuNRs. This process induced multicolor changes in the detection solution, shifting from light green to orange-red. The assay achieved a detection limit of 128 pM for β-gal. In suboptimal environments, the specific recognition and interaction between phages and their host bacteria is highly robust. Chen *et al.* developed chimeric phages that target *P. aeruginosa*, and by thiolating the phages, they

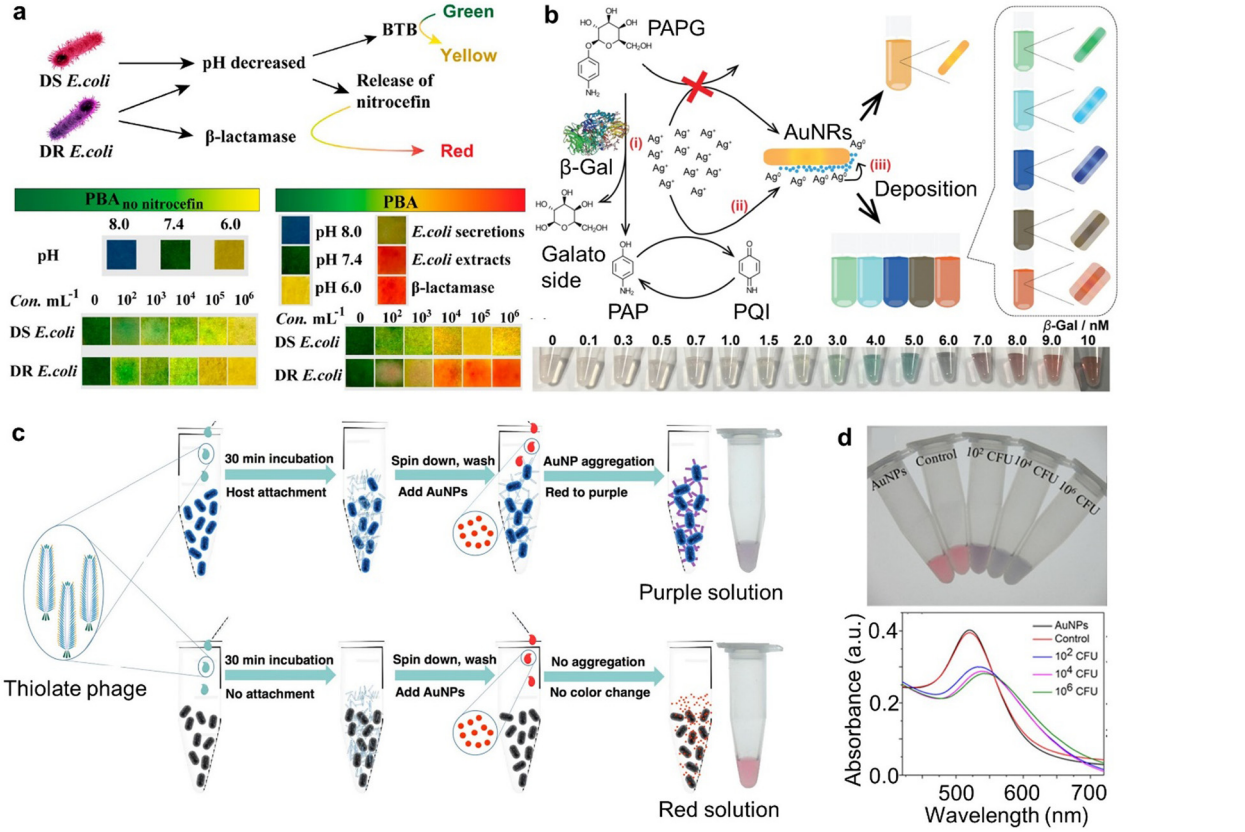

Fig. 42 Color detection of bacteria. (a) The schematic diagram illustrates the PBA (green) used for sensing bacterial infection (yellow) and drug resistance (red). Shown are the typical pictures of PBA before and after exposure to various substances.[366] (b) The sensing mechanism of the enzyme-induced AuNR growth-based colorimetric assay for monitoring β-gal concentration.[367] The tubes show colors change from green to red with increasing amount of β-gal. (c) To detect bacteria with phage AuNPs, thiolated phages are added to the sample with bacteria. After separating cell-phage complexes from free phage *via* centrifugation, resuspension causes AuNPs to aggregate, changing the color from red to purple. Nonhost cells do not cause NP aggregation and color change. (d) Photo and optical spectral detection of *P. aeruginosa* with thiolated phage and AuNPs in purchased milk.[368] (a) Reproduced from ref. 362,366 in accordance with CC BY-NC 4.0. Copyright 2020 American Chemical Society. (b) Reproduced with permission from ref. 367. Copyright 2016 Wiley. (c) and (d) Reproduced from ref. 368 in accordance with CC BY-NC 4.0. Copyright 2020 American Chemical Society.

induced the aggregation of AuNPs *via* Au–S bond, resulting in a colorimetric response.[368] The testing sample is mixed with chimeric phages, spun down, and then resuspended with AuNPs. The color indicates either no bacteria (free AuNPs, red) or bacteria presence (AuNPs attached to phages, purple, Fig. 42c and d). The limit of detection for this method was around 40 CFU or at least 100 cells of the target bacteria. This LoD is two orders of magnitude lower than that of commercially available bacterial detection kits.

6.6.2 Viruses. Viruses have genetic material (DNA or RNA) enclosed in a protein coat, and they interact with recognition moieties like antibodies, aptamers, protein receptors, and phages. For example, Niedziolka-Jonsson *et al.* developed a colorimetric immunosensor for T7 virus using covalently bonded anti-T7 antibodies on AuNPs, where the formation of immunological complexes between T7 virions and the antibody-modified nanoparticles leads to aggregation, achieving a limit of detection of 1.08×10^{10} PFU per mL (18 pM) for T7.[369] The specific recognition between antibodies and viruses has also been used for SARS-CoV-2 detection. Velotta *et al.* demonstrated that AuNPs functionalized with antibodies targeting three surface proteins of SARS-CoV-2 (spike, envelope, and membrane) undergo a red-shift within minutes when exposed to a viral particle solution.[370] The comparison of the biosensor's readout at 560 nm with the threshold cycle (C_t) of real-time PCR confirmed the detection of viral loads corresponding to $C_t = 36.5$ by the colorimetric biosensor. Materón *et al.* utilized a similar approach by covalently bonding the antibody to the AuNPs, achieving a detection limit of 0.28 PFU per mL for SARS-CoV-2 in human saliva.[371]

Bansal *et al.* developed a rapid and highly specific colorimetric sensor for detecting the murine norovirus (MNV) virion, the main cause of norovirus gastroenteritis, by combining the target specificity of a MNV AG3 aptamer and the NanoZyme activity of AuNPs.[372] The sensor probe, consisting of AuNPs passivated with the AG3 aptamer, recovers the NanoZyme activity selectively in the presence of MNV, leading to the generation of a characteristic blue color through the catalytic oxidation of the colorless TMB substrate. The LoD was 200 viruses per mL in 10 min.

The pathogen SARS-CoV-2 enters the host cell by binding to the human angiotensin-converting enzyme 2 (ACE2) receptor. Exploiting the specific interactions between the coronavirus and

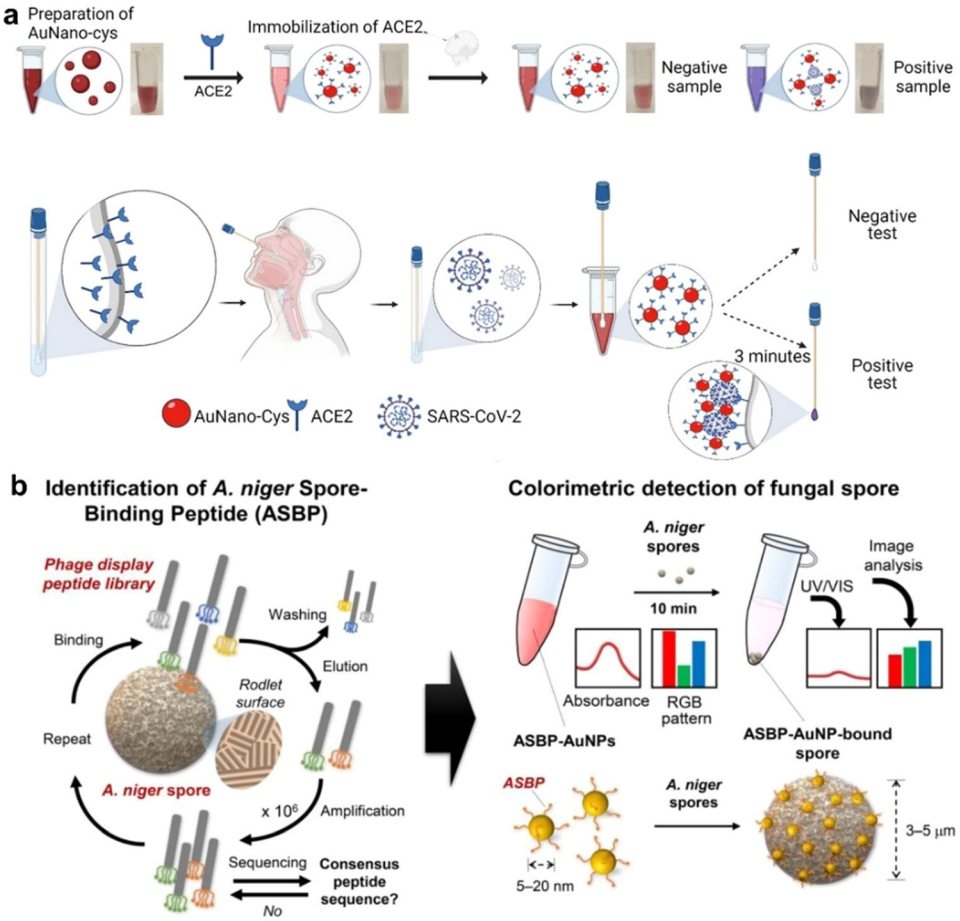

Fig. 43 Color detection of viruses and fungi. (a) Steps and photos demonstrate the colorimetric detection of SARS-CoV-2 in an aqueous medium using the synthesized AuNano-cys-ACE2. The method detects the SARS-CoV-2 spike protein by observing a AuNano-cys-ACE2 color change from red to purple, caused by aggregation.[373] (b) A schematic depicting the process of identifying *A. niger* spore-binding peptide ligands and their subsequent use in the colorimetric detection of fungal spores.[374] (a) Reproduced from ref. 373 in accordance with CC BY-NC-ND 4.0. Copyright 2021 American Chemical Society. (b) Reproduced with permission from ref. 374. Copyright 2021 Wiley.

ACE2, Fuente-Nunez *et al.* developed a colorimetric biosensor on cotton swabs using AuNPs modified with ACE2 (Fig. 43a).[373] The biosensor enables the colorimetric detection of SARS-CoV-2 within 5 min, with the color change resulting from the cross-linking of AuNP-ACE2 conjugates by virion particles. The biosensor detected very low viral particle loads (limit of detection: 0.154 pg mL^{-1} of SARS-CoV-2 spike protein), and the color intensity was positively correlated with the cycle threshold values obtained by PCR.

6.6.3 Fungi. Fungi reproduce *via* spores, which can be transmitted through contact or inhalation. Fungal diseases, like aspergillosis, cryptococcosis, mucormycosis, and *Candida albicans* infections, can affect different body parts, such as the urinary tract, stomach, mouth, and vagina.[375] Colorimetric methods for fungal detection are less common, but they utilize biomarkers like galactomannan, mannan, β-(1,3)-D-glucan, and cryptococcal capsular polysaccharide. Fungitell is a commercially available assay kit that employs a colorimetric approach to detect and quantify β-(1–3)-D-glucan in serum and cerebrospinal fluid. Although it is generally considered a sensitive, non-specific test for various fungal infections, some fungal groups like Cryptococcus spp. produce lower levels of (1–3)-β-D-glucan.[376] Detection of elevated β-glucan levels is often observed in *Pneumocystis jirovecii* infection.[377] Alternatively, Chung *et al.* established a colorimetric technique using a specific binding peptide obtained through phage display screening to detect *Aspergillus niger* spores by leveraging the interactions between fungal spores and the peptide-AuNPs.[374] The binding peptides exhibited the capability to detect 50 spores within a 10-min timeframe (Fig. 43b).

6.7 Pet care accessories

Colorimetric pet care accessories employ a variety of color agents targeting multiple analytes to offer rapid and visual health evaluations for pets (Table 9). For instance, the commercially available PrettyLitter employs porous silica particles coated with several dye or nanoparticle colorants.[378] These include bromothymol blue for pH detection, diisopropylbenzene dihydroperoxide for blood detection, tetrabromophenol blue for protein detection, glucose oxidase for glucose detection, and gold nanoparticle-relaxin antibodies for pregnancy detection. When the colored silica crystals interact with feline urine or feces, they become activated and impart distinct colors

Table 9 Representative commercial colorimetric kit based on activatable systems

Product name	Application	Target analytes
Easytest 7	Pool, spa, or fish water test	Bromine, chlorine, total hardness, and cyanuric acid
Kirkland signature diaper	Wetness indicator	Protons in urine
Siemens Multistix 10 Sg reagent strips	Urinalysis testing for medical diagnosis	Glucose, bilirubin, ketone, specific gravity, blood, pH, protein, urobilinogen, nitrite, and leucocytes
Dextrostix reagant strips	Blood glucose self-monitoring diabetes mellitus	Glucose
NIK-A test kit	Drug of abuse	Fentanyl
Ecotest COVID-19 rapid test devices	Infectious disease test	IgG/IgM
Phadebas® amylase tablets	Forensic detection	Amylase and saliva
Pregnancy test kit	Pregnancy test	Human chorionic gonadotropin
PrettyLitter	Pet medical health monitoring	pH, blood, protein, glucose, and pregnancy hormone

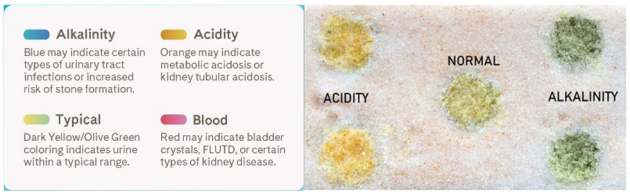

Fig. 44 PrettyLitter color changes indicate the feline medical conditions. Photo credit to PrettyLitter.

to clear silica crystals. These colors include yellow/olive green (normal), blue (alkalinity or urinary tract infections), orange (acidity or metabolic acidosis), or red (kidney diseases), thereby assisting in identifying potential health issues and call for medication care (Fig. 44).

7. Challenges and strategic considerations

The urgent need in various public healthcare scenarios ranging from infectious foodborne outbreaks to the growing awareness of individual healthcare status such as pregnancy and diabetes have sparked substantial interest in POC colorimetric sensing systems. The preceding COVID-19 case also underscores the need for a straightforward and effective diagnostic platform. The POC devices highlight the importance of early and simple identification, effective prevention, and control measures. In this section, we outline and discuss the barriers that prevent translating the sensing systems into clinics. We also furnish prospective solutions and strategic considerations to be incorporated into the design of next-generation sensing systems, thus contributing to the continuous refinement and optimization of the sensor performance.

7.1 Multiplexing

Multiplexing is the practice of recognizing numerous biomarkers in one diagnostic test to statistically improve detection accuracy. One example is the detection of *p*-tau and *t*-tau for clinically accurate diagnosis of Alzheimer's disease.[379] However, the development of clinically useful multiplexed sensors is challenging due to the limited color patterns and cross-reactivity. Strategies targeting the severe spectral/color crosstalk can be categorized into spatial multiplexing, time division multiplexing, frequency division multiplexing and others.[380] For example, the μPADs (Section 4), microarrays, or chemical noses (Section 5) within a single test strip is an example of spatial multiplexing, where combinational colors encode different analytes in multiple detection spots, addressing the need for comprehensive diagnostic testing.[381] The utilization of advanced nanoparticle-based colorimetric systems that offer a broader range of distinct colors could further improve the multiplexing strategy.[382] To address cross-contamination from related analytes, stringent sample regent dosing and specific recognition elements could be adapted. In addition, advancements in signal processing and image analysis techniques can further aid in deciphering the complex colorimetric patterns generated by multiplexed sensors, enhancing their overall capabilities and results readout.

7.2 Matrix effect and interference

Matrix effects pose a formidable challenge in colorimetric assays, primarily due to the inherent complexity of samples utilized in analysis, encompassing blood, urine, saliva, and environmental samples. These complexities have hindered the transition of many benchtop colorimetric assays to the realm of translational point-of-care devices. These matrices introduce interference that affects the accuracy of the sensor response. One source of interference is the uncontrollable nature of nanoparticle aggregation and self-aggregation in complex samples, leading to high background signals and false-positive results. Additionally, the formation of protein corona on nanoparticles can result in false-negative signals in NP-aggregation-based colorimetric sensors.[16] Some matrices also contain natural inhibitors that hinder the bioactivity of target analytes. For instance, lower matrix metalloproteinase activity in serum solutions can be attributed to the presence of α-2-macroglobulin proteins, known as broad-spectrum protease inhibitors.[383] In some cases, the target analyte complexes with high-molecular-weight components in these matrices interfere with its capture and/or detection. To overcome these challenges, various strategies can be employed: (i) Sample pre-treatment methods such as filtration (*e.g.*, sample pad in LFAs), enzymatic pretreatment,[384] dilution,[118] or extraction can be applied to minimize matrix interference and enhance the reliability of colorimetric measurements. However, it is important to strike a balance, as excessive or harsh pretreatment may lead to analyte deactivation in the samples.

(ii) Another approach involves the use of masking agents in the assay to neutralize interfering substances, effectively mitigating their impact on the colorimetric reaction. Nevertheless, these pretreatments compromise the advantage—simplicity. Consequently, recent proposals involve various surface functionalization of nanoparticles and dissociation systems. For example, optimizing complexation interactions, such as employing aromatic interactions, proves advantageous in high ionic media like saliva, where interference is reduced.[342] Furthermore, the dissociation approach, where the disassembly of gold clusters is based on their interaction with target analytes, is less affected by the protein corona phenomenon and other challenging conditions.[108,345]

7.3 Specificity

Cross-reactivity from analyte analogues could lead to false positive or false negative results, especially if the system exhibits low affinity between the binding site and the target analyte. Current strategy uses specific binding biological molecules such as antibodies, receptors, substrates, aptamers, or molecularly imprinted polymers to enhance the sensor's specificity for the target analyte. The process of validating biomarkers and identifying affinity reagents such as experimental substrate profiling, phage display, or aptamer selection *via* systematic evolution of ligands by exponential enrichment is effective but can be labor-intensive, expensive in a lab, and challenging. This makes the creation of a new assay difficult. Alternative approaches could rely on online data banks or other computational tools such as AlphaFold and molecular docking simulations. In terms of protease substrate design, an effective strategy could involve the protease database (*e.g.*, MEROPS database[385]) and the affinity calculation webserver (*e.g.*, PepSite 2[386]) as an initial assessment to identify the high affinity sequences.[361] Furthermore, enhancing specificity can be achieved by incorporating unnatural amino acids and fine-tuning the substrate design, thereby minimizing the occurrence of undesired off-site cleavage.[16] In practice, it is essential to test and report the specificity of the sensor towards other related analytes or background biomolecules for every colorimetric sensor. For example, testing should include all other metal ions in an ion detection system, and testing should encompass all other relevant enzymes for a protease test, to ensure comprehensive characterization and specificity assessment.

7.4 Sensitivity

The detection limit of colorimetric sensors is reported *via* two assessments including spectrometer measurement or visual observation. Low limit detection is challenging due to limited reaction kinetics, poor color responses, or low signal-to-noise ratios. The balance between sensitivity and working window (dynamic range)/readout time is a trade-off: high sensitivity is typically coupled with a narrow working window and a long readout time. The straightforward strategies to improve sensitivity are by enhancing the signal and reducing background. (i) These include incorporating amplification strategies such as enzyme-linked reactions in ELISA or signal enhancement techniques like plasmonic nanoparticles with large molar absorptivity. For instance, nanoparticles with SPR at 500 nm with minimal spectral shift could exhibit remarkable visual color changes, resulting in a 6-fold increase in sensitivity.[51] (ii) In nanoparticle-based colorimetric assays, optimizing surface chemistry for nanoparticles and leveraging multivalent interactions with target analytes could significantly enhance assay sensitivity, with improvements ranging from 2- to 10-fold.[118]

Background components, such as proteins, small molecules, and ions can interfere with the colorimetric signal. Implement strategies for background reduction could include sample pretreatment, recognition moieties of high affinity, baseline correction, and the use of blocking or inhibition agents that bind to and neutralize interfering substances. In practice, the detection limit should be reported together with the readout time, and assay conditions such as matrix and temperature. When determining the detection limits through visual examination, employing blind tests can offer a more scientifically rigorous approach with minimized subjective interpretations.[51]

7.5 User friendly

Advancing the colorimetric mechanisms could introduce additional complexities, posing difficulties for end-users in utilizing the technology, while also raising concerns about cost-effectiveness. Certain biosensing systems require multi-step operations, invasive sampling, or complicated pattern interpretation, which overshadow the benefits of point-of-care device performance. For example, nasal swab sampling necessitates the selection of an appropriate sampling site and good collection timing to ensure detection results. The training process entails additional time and labor costs, which may be unattainable in resource-limited settings. Blood testing could be invasive and unfriendly, especially to children and others. Microarray assays generate numerous signal patterns, and the readout could be challenging. Improvements were made by smartphones for simplifying results interpretation and providing image capture, data analysis, and longitudinal result records. The primary goal for developers is to fabricate biosensing systems with streamlined workflows and user-friendly operation, ensuring simplicity and accessibility.

7.6 Safety

Ensuring the biosafety of a diagnostic platform is of paramount importance in POC biosensing for molecular diagnosis. While the primary goal is to eliminate the reliance on traditional biological laboratories, biosafety considerations must not be overlooked. Proper management and disposal of surplus reaction samples and reagents are essential to minimize potential hazards. The entire process, spanning sample preparation, specific reactions, and result reporting, should be meticulously executed to avoid abnormal cross-reactions, variations, or any unforeseen complications. Moreover, the choice of materials and color agents used in the diagnostic platform significantly impacts biosafety. It is imperative to prioritize the use of non-toxic substances that have received regulatory approvals, such as those sanctioned by the FDA. Special attention should be paid to avoiding the inclusion of heavy metals and other non-compliant materials that pose potential health risks. Additionally, the

platform should exhibit robust stability against fluctuations in temperature and pressure to ensure the elimination of any potential biological hazards.

Data security is a crucial aspect that must be considered throughout all the steps involved in biosensing, including data collection, transmission, and storage. Particularly in colorimetric diagnosis testing, which deals with the most private information of the human body, ensuring the security of data becomes paramount. The introduction of smartphones and automated data processing procedures has made the entire process more efficient. However, the use of cloud communication systems and the involvement of large-scale data, often with the aid of artificial intelligence techniques, necessitate reliable proof of data security in biosensing for molecular diagnosis.[387] In the specific scenario of COVID, a solution to ensure data safety is to establish a clear and transparent communication process regarding the release of COVID detection results. While maintaining the confidentiality and protection of data to prevent unauthorized access or leaks, users can be encouraged to provide positive results to their healthcare providers and local health departments. This helps in controlling the spread of the virus without compromising personal identifying information. Implementing a well-defined consent mechanism allows users to make an explicit decision about sharing their data. This can be facilitated through informed consent forms or digital platforms that provide users with the option to grant permission for the release of their detection results. Furthermore, robust data protection measures must be put in place to safeguard the privacy and security of user data. This includes employing encryption techniques, implementing strict access controls, and adhering to data protection regulations and guidelines. By incorporating these measures, users can have control over the release of their COVID detection results, ensuring that their privacy is respected while maintaining strict precautions to prevent data leaks and unauthorized access. Ultimately, this fosters trust in the biosensing process and promotes data security in molecular diagnosis.

8. Outlook

Colorimetric sensing and translational POC applications have shown great promise in biomedical applications especially for non-invasive and selective diagnosis. Recent developments in novel colorant materials, miniaturization, micro-computerization, and testing procedures have advanced the production of multifunctional, compact, and portable POC biosensing devices.

8.1 Biomimetic colorants

Biomimetic structurally colored biomaterials including butterfly wings,[388] insect cuticles,[389] cephalopod skins,[390] biomimetic virus,[391] and avian skins/feathers[392] offer alternative insights into the development of colorimetric sensors. These bio-inspired materials display brilliant colors arising from their hierarchically organized structures while also maintaining strong resistance to photobleaching.[393]

The structural colors in these biomaterials are typically produced through interference effects with light. Their micro- or nano-structures scatter or reflect light at certain frequencies.[393] Their unique structural color can be further engineered to respond to various stimuli, such as temperature,[394] humidity,[395,396] pH,[397] magnetic field,[398,399] and the presence of specific analytes.[400] For example, Schenning *et al.* demonstrated that cholesteric liquid-crystalline (CLC) polymer particles respond to their transition temperature.[394] CLC polymer particles showed a red-shift of the reflected color at T = 100 °C, and the reflection is significantly reduced above isotropic T at 120 °C due to its liquid-crystalline disorder (Fig. 45a). Zi *et al.* successfully created silk-fibroin-based inverse opals capable of bi-structural color reflection.[395] They also achieved facile tunability of the reflection peak of inverse opal by using colloidal spheres with different sizes. These silk fibroin inverse opals exhibit changes in their reflection peaks in response to different humidity levels due to the shrinkage or swelling of their opal's diameter, resulting in a color shift from yellow to reddish-like beetles (Fig. 45b). Recently, Tang *et al.* demonstrated a novel method for synthesizing polypeptide-based structural color films that is color responsive toward pH.[397] These films, structured as inverse opals, rely on the periodic arrangement of pores. Variations in pH induce volume changes within these pores caused by the ionization of carboxyl groups in polypeptides. This ionization of carboxyl groups increases electrostatic repulsion at higher pH level (Fig. 45c). Thus, the polypeptide-based color film exhibits pH-dependent photonic behavior, shifting its color from green to red as pH level increases (Fig. 45d). Overall, researchers can develop materials that undergo color change in response to specific stimuli by incorporating these structural features into sensors. This concept of using structural color for colorimetric sensing holds significance across various fields including environmental monitoring, biomedical diagnostics, and chemical analysis.

8.2 Injectable, implantable, or wearable systems

Diagnosis based on injectable, drinkable, or wearable systems holds immense promise in clinical management of diseases ranging from early detection to surveillance monitoring. Injected nanoparticles,[401,402] DNA barcodes,[403] or molecules[178] adapted on wearable device may interact with biomarkers through diverse proteolytic pathways that provide diagnostic information *via* biofluids including human urine, tear and sweat.[404,405] Stevens *et al.* demonstrated that gold clusters coupled with neutravidin were functionalized with proteolytic peptide to detect colorectal cancer by color changes in urine.[401] The secreted target enzyme (*i.e.*, MMP9) cleaved the peptides, leading to disassembly of gold clusters from neutravidin *in vivo*. The catalytic activity of dissociated gold clusters was monitored using the oxidation of peroxidase substrate by H_2O_2 in the collected urine, increasing a 13-fold higher colorimetric signal (Fig. 46a). CRISPR-enabled diagnostic platform has been shown high potential in early detection of diverse cancer models. Bhatia *et al.* unveiled that an eight-arm PEG nanocarrier functionalized with protease-responsive short peptides with oligonucleotides releases DNA barcodes for urinary-based early diagnosis of cancer biomarkers

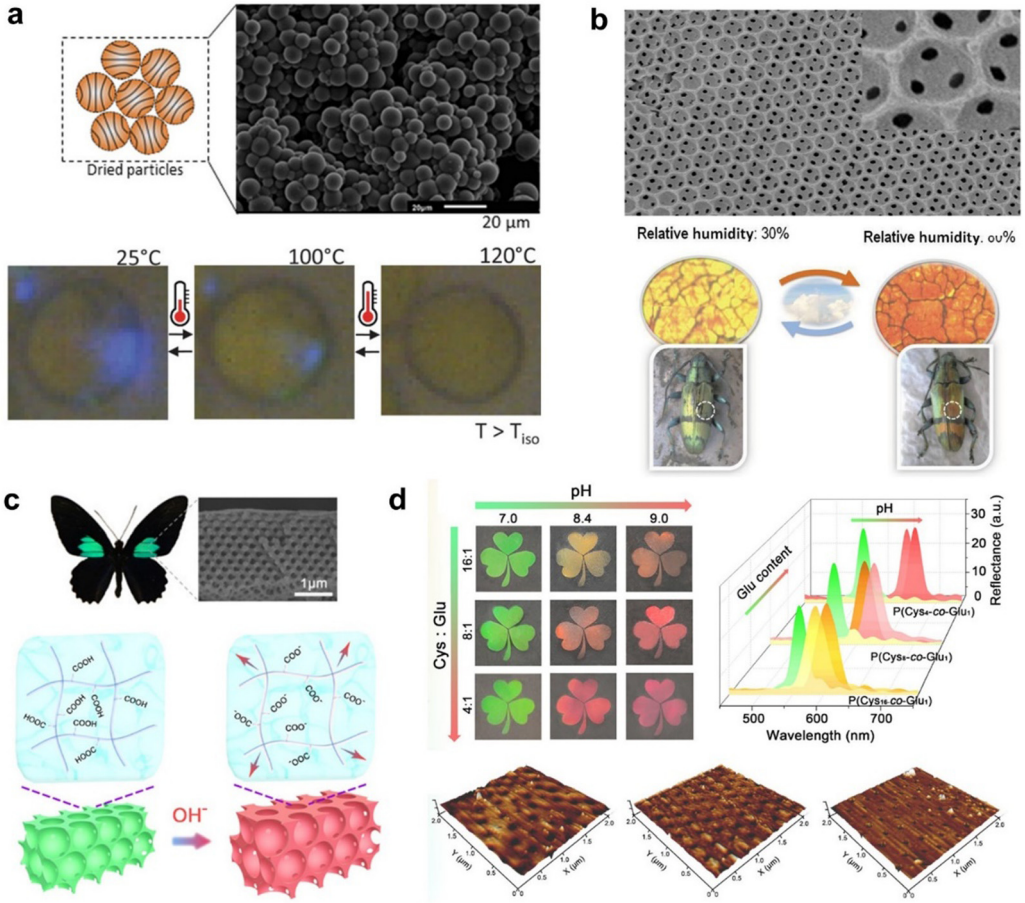

Fig. 45 Stimuli-responsive structural colors. (a) SEM image of cholesteric liquid-crystalline (CLC) polymer particles, and its temperature-responsiveness.[394] (b) SEM image of silk-fibroin inverse ovals capable of color changes in response to different humidity levels like beetles.[395] (c) SEM image of inverse opals made of polypeptides, and its schematic of volume changes in response to pH. (d) Higher pH induces red-shift of reflection peak.[397] (a) Reproduced from ref. 394 in accordance with CC BY-NC-ND 4.0. Copyright 2020 Wiley. (b) Reproduced with permission from ref. 395. Copyright 2013 Wiley. (c) and (d) Reproduced with permission from ref. 397. Copyright 2022 American Chemical Society.

(Fig. 46b).[403,406] The dissociated DNA barcodes upon specific proteolysis activate CRISPR-Cas nucleases in urine, where this activation further cleaves fluorescein (FAM)-biotin paired reporter and releases the FAM molecules. The FAM molecules then provide colorimetric response through POC diagnostic paper based on lateral-flow assay while the uncleaved reporters are trapped on the control band *via* biotin–streptavidin binding (Fig. 46c). Synthetic biomarkers based on enzymatic activity or cell responsiveness have been developed for early detection of cancer. These injectable and multiplexable sensors may hold value in future diagnostic platforms. Not only urine, but human sweat is also a valuable resource for wearable colorimetric sensing due to its richness in biomarkers: electrolytes, metabolites, and neuropeptides. Sweat sensors offer real-time, continuous, and non-invasive monitoring capacities. Recently, Wang *et al.* developed a wearable epidermal sweat sensor capable of monitoring sodium chloride, pH, lactate, and glucose in the sweat with high accuracy, selectivity (Fig. 46d).[405] The detection of target analytes such as glucose or lactate relies on enzymatic activity in which 1,4-naphthoquione-mediated glucose or lactase oxidase induces the oxidation of the target analyte, leading to the reduction of the working electrode. Sweat-based wearable biosensors hold significant potential in healthcare monitoring, personal wellness management, and sport science.

8.3 Smart device and digital technology

Recent advancements in wireless (lab-in-palm) and wearable (lab-on-wrist) technology, incorporating new mechanical, electrical, and optical features, have propelled the development of biosensing systems. The integration of wearable bio- and colorimetric-sensor with digital technology, such as smartphone apps,[408] QR codes,[409] or wearable sensing devices,[405] holds the promise of enabling continuous, real-time, and quantitative analysis of the test results, facilitating remote healthcare monitoring. Artificial intelligence and machine learning further enhance colorimetric sensing by enabling automated analysis of subtle color variations, image patterns, and complex datasets, improving the accuracy and efficiency of color-based measurements.[410,411] For example, a facemask was equipped with sensors for SARS-CoV-2 detection in exhaled aerosol for personal health-monitoring. Collins *et al.* demonstrated a smart mask for diagnosing personal respiratory

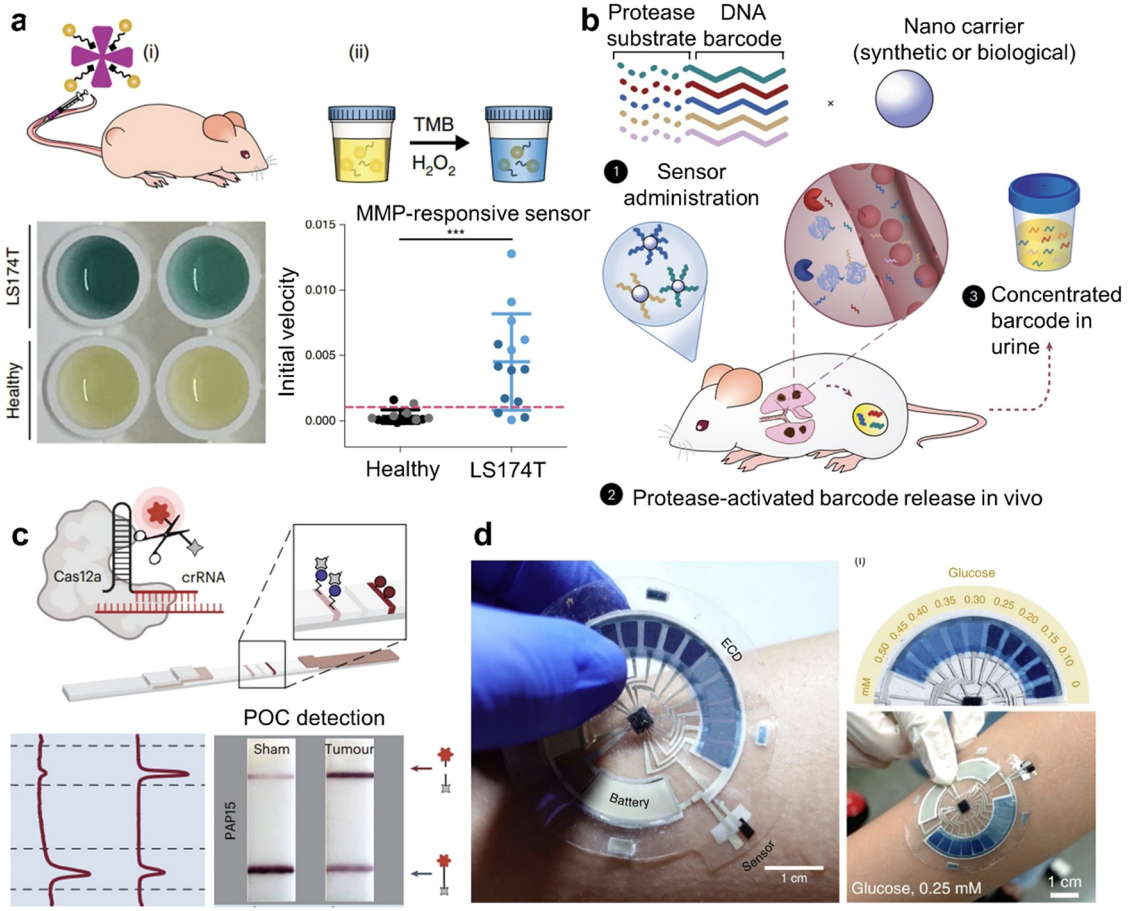

Fig. 46 Injectable/wearable system for simple, non-invasive, and accurate diagnosis. (a) Schematic illustration of injectable gold cluster-neutravidin complex for colorectal cancer (LS174T) diagnosis. The photograph shows that the target enzyme cleaves the complex and dissociates gold clusters which in turn changes color in urine based on their catalytic activity.[401] (b) CRISPR-Case-enabled DNA barcode detection in urinary sample. Injected polymeric nanoparticles functionalized with protease-responsive peptide with DNA barcodes interact with biomarkers, releasing the barcodes which are used for point-of-care diagnostic paper (c). The photograph in (c) shows that the cleaved DNA barcodes activate the FAM molecules for color change.[407] (d) Photograph of a wearable sweat sensor that can monitor various types of analytes including pH, sodium chloride, lactate, and glucose.[405] (a) Reproduced with permission from ref. 401. Copyright 2019 Nature. (b,c) Reproduced from ref. 407 in accordance with CC BY 4.0. Copyright 2023 Nature. (d) Reproduced with permission from ref. 405. Copyright 2022 Nature.

conditions.[306] The facemask is designed to capture and accumulate viruses on the inside of masks during coughing or breathing. When SARS-CoV-2 RNAs are present, they trigger the cleavage of FAM-Biotin polynucleotide probes through serial reaction cascades (Fig. 47a). Ultimately, the cleaved probes activate a colorimetric visual readout based on an integrated lateral flow assay. This smart mask can provide alerts to prevent the spread of nosocomial infection and simultaneously serves as personal protective and diagnostic equipment.[306]

In addition, Mahshid *et al.* introduced a microfluidic device capable of detecting SAR-CoV-2 virus in saliva. This device incorporates plasmonic nano-surface, where light irradiation can lead to plasmonic oscillation of free electrons, catalyzing electron-driven nucleic acid amplification (Fig. 47b).[412] During the amplification process, protons prompt a rapid color change of phenol red. Further incorporating a machine learning algorithm data analysis and training, the final device demonstrates the ability to differentiate target variants and subvariant variants of SARS-CoV-2. It provides a clinical relevant sensitivity and specificity with 95% accuracy.

Smartphone-based sweat sensing has seen significant development for non-invasive, real-time, and continuous health monitoring. Recent development in wearable devices powered by a perovskite solar cell eliminate the need for batter support, improving portability (Fig. 47c).[408] Rodgers *et al.* developed a soft and wearable microfluidic device that could quantitatively monitor various analytes, including glucose, lactate, chloride, pH, and creatine from sweat collected during exercise (Fig. 47c). Only 5 to 10 μL of sweat sample is required to induce color change, and the colorimetric response occurs within 1 min. Detecting target analytes is based on enzymatic reaction with corresponding dyes. For example, glucose oxidase produces hydrogen peroxide which oxidizes iodide for color. More importantly, smartphone cameras were used to analyze colorimetric responses. The obtained RGB value from wearable sensor was

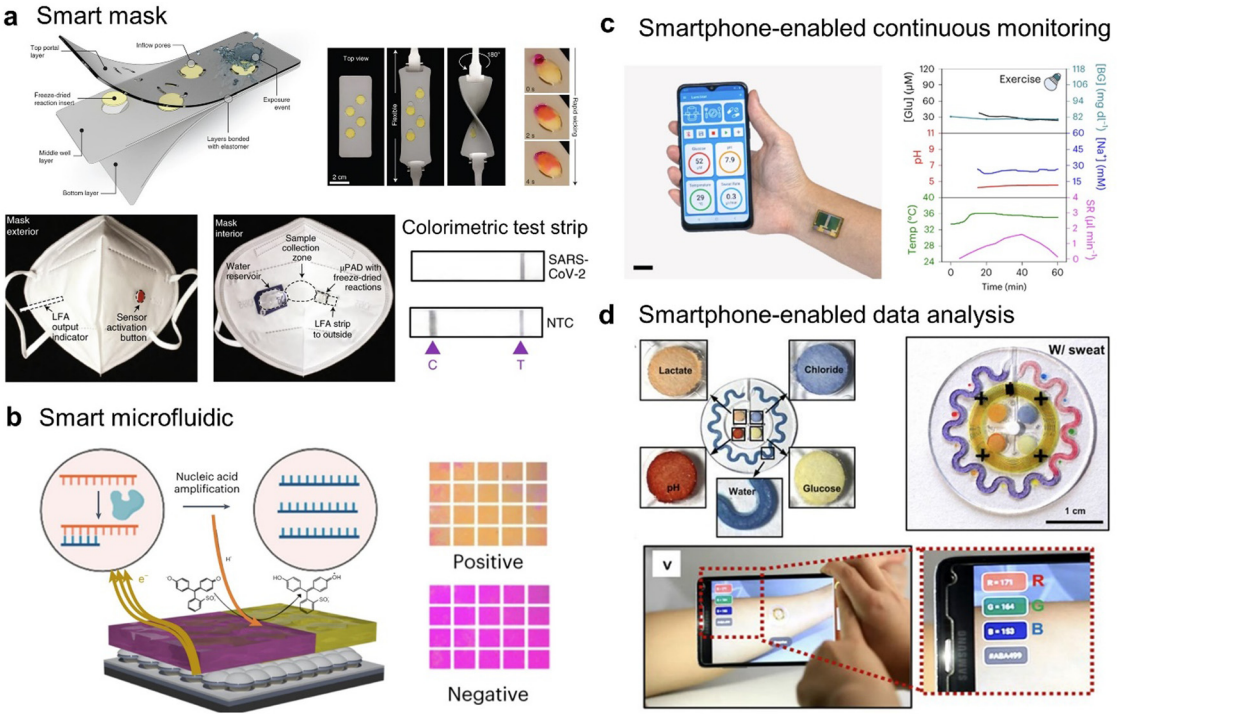

Fig. 47 Smart diagnostic platform combined with digital technology. (a) A facemask was integrated with a colorimetric strip test sensor for SARS-CoV-19 detection. The photograph shows the integrated strip sensor with respirator. The collected virus induces the cleavage of FAM-biotin DNA links which in turn activate colorimetric signals.[306] (b) Plasmonic nano-surface was integrated on the microfluidic device for accurate and rapid colorimetric detection of SARS-CoV-19.[412] (c) Smartphone-assisted sweat sensor can provide non-invasive, real-time, and continuous monitoring of health conditions.[408] (d) The smartphone camera could be utilized to quantify the activated colorimetric signals based on the RGB value.[413] (a) Reproduced with permission from ref. 306. Copyright 2021 Nature. (b) Reproduced with permission from ref. 412. Copyright 2023 Nature. (c) Reproduced with permission from ref. 408. Copyright 2023 Nature. (d) Reproduced with permission from ref. 413. Copyright 2016 American Association for the Advancement of Science.

used to quantify the concentrations of target analytes, indicating that smart digital technology not only provides continuous monitoring but also performs quantitative data analysis (Fig. 47d). Further development of colorimetric chemistries for enzymatic reactions and enzyme-mimetic nanomaterials could improve the limit of detection for wearable colorimetric sensor.[175,178]

9. Concluding Remarks

In this review, we covered the basic components for designing colorimetric sensing systems, typical examples of POC devices, recent exciting sensing techniques based on combinational and activatable systems up to 2023, and challenges and future perspectives. Two colorants were presented, including plasmonic NPs as the major portion for discussion and organic dyes. Plasmonic NPs offer cost-effective production, high molar absorption coefficients, photo bleach resistance, and multifunctionality. As described above, plasmonic NPs for colorimetric sensing contain AuNPs, AgNPs, and Au/Ag alloy NPs. The signaling mechanisms by NPs typically involve aggregation, redispersion, etching, dissolution, formation, and re-shaping in the presence or activity of target analytes. Organic chromophores possess high design flexibility, exceptional sensitivity, biocompatibility, and a wide range of colors. These chromophores are typically categorized into Brønsted acidic or basic dyes, Lewis acid/base dyes, redox dyes, and chromogenic aggregative dyes. The colorimetric mechanisms by organic chromophores typically involve changing the separation distance, structural resonance, complexation state, energy levels, conformational rigidity, and modifications to its electronic structure or bonding in the presence of analytes. The large library of colorimetric reagents, color changing mechanisms, and recognizing interactions have generated emerging techniques and commercial POC devices. For example, the rational design and translational applications of LFA, μPAD, and wearable sensors were presented. A particularly important aspect of LFA is the ability to detect viral spike protein and antibodies, a challenge that has received a lot of attention for infectious disease prevention. In terms of colorimetric format, we highlighted the combinational and activatable sensing systems based on sensor-array and lock-key mechanisms, respectively. Sensor arrays test the selective binding of an analyte to a cross-reactive array of receptors, leading to a color pattern for detection. Sensor arrays show great capabilities in detecting unknown analytes and dealing with analogue interference and complex sample compositions. The activatable sensing systems incorporate specific interacting components that recognize the analyte *via* a lock-key mechanism. The recognition component ensures high selectivity, substantial contrast, easy readout, and

are quantifiable through ratiometric analysis. Analyte sensing based on the above two systems was discussed, including ions, small molecules, biological macromolecules, enzymes, pathogens, among others. Finally, numerous colorimetric sensing systems and POC devices encounter limitations in multiplexing capabilities, susceptibility to interference from matrices and analogues, constraints in testing size capacity, and safety concerns regarding data sharing. With growing awareness of health and public concerns, many researchers are actively engaged in this promising field. As a result, the development of advanced and versatile colorimetric sensors for translational applications holds significant potential for making a substantial impact on environmental monitoring, food safety testing, and biomedical diagnostics.

Conflicts of interest

There are no conflicts to declare.

Acknowledgements

This work was supported through the National Institutes of Health (R01 DE031114; R21 AG065776-S1; R21 AI157957) and National Science Foundation (CBET-2335597; DMR-2242375).

Notes and references

1 H. Chen, S. Cai, J. Luo, X. Liu, L. Ou, Q. Zhang, B. Liedberg and Y. Wang, *TrAC, Trends Anal. Chem.*, 2024, **173**, 117654.
2 B. Kaur, N. Kaur and S. Kumar, *Coord. Chem. Rev.*, 2018, **358**, 13–69.
3 V. S. Ajay Piriya, P. Joseph, S. C. G. Kiruba Daniel, S. Lakshmanan, T. Kinoshita and S. Muthusamy, *Mater. Sci. Eng., C*, 2017, **78**, 1231–1245.
4 J. Zhou, Y. Liu, X. Du, Y. Gui, J. He, F. Xie and J. Cai, *ACS Omega*, 2023, **8**, 46346–46361.
5 C. Wang, M. Liu, Z. Wang, S. Li, Y. Deng and N. He, *Nano Today*, 2021, **37**, 101092.
6 Y. Wu, J. Feng, G. Hu, E. Zhang and H.-H. Yu, *Sensors*, 2023, **23**, 2749.
7 B. Liu, J. Zhuang and G. Wei, *Environ. Sci.: Nano*, 2020, **7**, 2195–2213.
8 R. Umapathi, S. Sonwal, M. J. Lee, G. Mohana Rani, E.-S. Lee, T.-J. Jeon, S.-M. Kang, M.-H. Oh and Y. S. Huh, *Coord. Chem. Rev.*, 2021, **446**, 214061.
9 M. Ham, S. Kim, W. Lee and H. Lee, *Biosensors*, 2023, **13**, 18.
10 J. R. Askim and K. S. Suslick, *Anal. Chem.*, 2015, **87**, 7810–7816.
11 Biosensors Market Size, Share, Industry Growth Analysis Report by Type, Product, Technology, Application, **https://www.marketsandmarkets.com/Market-Reports/biosensors-market-798.html** (accessed 05-07-2024).
12 L. Roy, P. Buragohain and V. Borse, *Biosens. Bioelectron.: X*, 2022, **10**, 100098.
13 Z. Li, J. R. Askim and K. S. Suslick, *Chem. Rev.*, 2019, **119**, 231–292.
14 K. Saha, S. S. Agasti, C. Kim, X. Li and V. M. Rotello, *Chem. Rev.*, 2012, **112**, 2739–2779.
15 Y. Hang, A. Wang and N. Wu, *Chem. Soc. Rev.*, 2024, **53**, 2932–2971.
16 Z. Jin, Y. Mantri, M. Retout, Y. Cheng, J. Zhou, A. Jorns, P. Fajtova, W. Yim, C. Moore, M. Xu, M. N. Creyer, R. M. Borum, J. Zhou, Z. Wu, T. He, W. F. Penny, A. J. O'Donoghue and J. V. Jokerst, *Angew. Chem., Int. Ed.*, 2022, **61**, e202112995.
17 C.-S. Tsai, T.-B. Yu and C.-T. Chen, *Chem. Commun.*, 2005, 4273–4275, DOI: **10.1039/B507237A**.
18 M. M. Singh and J. Satija, *Anal. Biochem.*, 2022, **654**, 114820.
19 S. Unser, I. Campbell, D. Jana and L. Sagle, *Analyst*, 2015, **140**, 590–599.
20 M. Retout, Y. Mantri, Z. Jin, J. Zhou, G. Noël, B. Donovan, W. Yim and J. V. Jokerst, *ACS Nano*, 2022, **16**, 6165–6175.
21 H. S. Jung, X. Chen, J. S. Kim and J. Yoon, *Chem. Soc. Rev.*, 2013, **42**, 6019–6031.
22 W. Zhou, X. Gao, D. Liu and X. Chen, *Chem. Rev.*, 2015, **115**, 10575–10636.
23 Y.-F. Ou, T.-B. Ren, L. Yuan and X.-B. Zhang, *Chem. Biomed. Imaging*, 2023, **1**, 220–233.
24 Y. Chen, H. Jiang, T. Hao, N. Zhang, M. Li, X. Wang, X. Wang, W. Wei and J. Zhao, *Chem. Biomed. Imaging*, 2023, **1**, 590–619.
25 W. Cheng, H. Chen, C. Liu, C. Ji, G. Ma and M. Yin, *VIEW*, 2020, **1**, 20200055.
26 S. Lakshmanan and M. A. El-Sayed, *Annu. Rev. Phys. Chem.*, 2003, **54**, 331–366.
27 L. M. Liz-Marzán, *Mater. Today*, 2004, **7**, 26–31.
28 L. Yu, Z. Song, J. Peng, M. Yang, H. Zhi and H. He, *TrAC, Trends Anal. Chem.*, 2020, **127**, 115880.
29 J. Turkevich, P. C. Stevenson and J. Hillier, *Discuss. Faraday Soc.*, 1951, **11**, 55–75.
30 S. Liu, G. Chen, P. N. Prasad and M. T. Swihart, *Chem. Mater.*, 2011, **23**, 4098–4101.
31 N. G. Bastús, J. Comenge and V. Puntes, *Langmuir*, 2011, **27**, 11098–11105.
32 K. R. Brown and M. J. Natan, *Langmuir*, 1998, **14**, 726–728.
33 M. Yang, P. Moroz, Z. Jin, D. S. Budkina, N. Sundrani, D. Porotnikov, J. Cassidy, Y. Sugiyama, A. N. Tarnovsky, H. Mattoussi and M. Zamkov, *J. Am. Chem. Soc.*, 2019, **141**, 11286–11297.
34 E. Oh, K. Susumu, R. Goswami and H. Mattoussi, *Langmuir*, 2010, **26**, 7604–7613.
35 S. Barbosa, A. Agrawal, L. Rodríguez-Lorenzo, I. Pastoriza-Santos, R. A. Alvarez-Puebla, A. Kornowski, H. Weller and L. M. Liz-Marzán, *Langmuir*, 2010, **26**, 14943–14950.
36 N. R. Jana, L. Gearheart and C. J. Murphy, *Adv. Mater.*, 2001, **13**, 1389–1393.
37 N. R. Jana, L. Gearheart and C. J. Murphy, *J. Phys. Chem. B*, 2001, **105**, 4065–4067.
38 B. Nikoobakht and M. A. El-Sayed, *Chem. Mater.*, 2003, **15**, 1957–1962.
39 W. Yim, R. M. Borum, J. Zhou, Y. Mantri, Z. Wu, J. Zhou, Z. Jin, M. Creyer and J. V. Jokerst, *Nanotheranostics*, 2022, **6**, 79–90.

40 Z. Jin, Y. Sugiyama, C. Zhang, G. Palui, Y. Xin, L. Du, S. Wang, N. Dridi and H. Mattoussi, *Chem. Mater.*, 2020, **32**, 7469–7483.
41 Y. Zhao, *Quantum dots and doped nanocrystals: synthesis, optical properties and bio-applications*, PhD thesis, Utrecht University, 2013, DOI: 10.13140/RG.2.2.32338.15047.
42 S. Xu, W. Ouyang, P. Xie, Y. Lin, B. Qiu, Z. Lin, G. Chen and L. Guo, *Anal. Chem.*, 2017, **89**, 1617–1623.
43 Y. C. Wang, É. Rhéaume, F. Lesage and A. Kakkar, *Molecules*, 2018, **23**, 2851.
44 L. Tong, L. Wu, Y. Zai, Y. Zhang, E. Su and N. Gu, *Biosens. Bioelectron.*, 2023, **219**, 114787.
45 Y. Mantri, B. Davidi, J. E. Lemaster, A. Hariri and J. V. Jokerst, *Nanoscale*, 2020, **12**, 10511–10520.
46 Z. Gao, S. Shao, W. Gao, D. Tang, D. Tang, S. Zou, M. J. Kim and X. Xia, *ACS Nano*, 2021, **15**, 2428–2438.
47 H. D. Beyene, A. A. Werkneh, H. K. Bezabh and T. G. Ambaye, *Sustainable Mater. Technol.*, 2017, **13**, 18–23.
48 D. Paramelle, A. Sadovoy, S. Gorelik, P. Free, J. Hobley and D. G. Fernig, *Analyst*, 2014, **139**, 4855–4861.
49 Y. Qing, L. Cheng, R. Li, G. Liu, Y. Zhang, X. Tang, J. Wang, H. Liu and Y. Qin, *Int. J. Nanomed.*, 2018, **13**, 3311–3327.
50 D. Aherne, D. M. Ledwith, M. Gara and J. M. Kelly, *Adv. Funct. Mater.*, 2008, **18**, 2005–2016.
51 P. Chen, X. Liu, G. Goyal, N. T. Tran, J. C. Shing Ho, Y. Wang, D. Aili and B. Liedberg, *Anal. Chem.*, 2018, **90**, 4916–4924.
52 P. Chen, Z. Yin, X. Huang, S. Wu, B. Liedberg and H. Zhang, *J. Phys. Chem. C*, 2011, **115**, 24080–24084.
53 J. J. Vos, *Color Res. Appl.*, 1978, **3**, 125–128.
54 J. Wang, C.-Y. Lin, C. Moore, A. Jhunjhunwala and J. V. Jokerst, *Langmuir*, 2018, **34**, 359–365.
55 C. Moore, R. M. Borum, Y. Mantri, M. Xu, P. Fajtová, A. J. O'Donoghue and J. V. Jokerst, *ACS Sens.*, 2021, **6**, 2356–2365.
56 Z. Jin, A. Kapur, W. Wang, J. D. Hernandez, M. Thakur and H. Mattoussi, *J. Chem. Phys.*, 2019, **151**, 164703.
57 Y. Ding, W.-H. Zhu and Y. Xie, *Chem. Rev.*, 2017, **117**, 2203–2256.
58 A. Colom, E. Derivery, S. Soleimanpour, C. Tomba, M. D. Molin, N. Sakai, M. González-Gaitán, S. Matile and A. Roux, *Nat. Chem.*, 2018, **10**, 1118–1125.
59 Z. M. Soilis, T. H. Choi, J. Brennan, R. R. Frontiera, J. K. Johnson and N. L. Rosi, *Chem. Mater.*, 2023, **35**, 7741–7749.
60 L. S. Foster and I. J. Gruntfest, *J. Chem. Educ.*, 1937, **14**, 274.
61 M. C. Janzen, J. B. Ponder, D. P. Bailey, C. K. Ingison and K. S. Suslick, *Anal. Chem.*, 2006, **78**, 3591–3600.
62 C. U. Lenora, R. J. Staples and M. J. Allen, *Inorg. Chem.*, 2020, **59**, 86–93.
63 L. Wu, Y. Sun, K. Sugimoto, Z. Luo, Y. Ishigaki, K. Pu, T. Suzuki, H.-Y. Chen and D. Ye, *J. Am. Chem. Soc.*, 2018, **140**, 16340–16352.
64 A. S. Jeevarathinam, J. E. Lemaster, F. Chen, E. Zhao and J. V. Jokerst, *Angew. Chem., Int. Ed.*, 2020, **59**, 4678–4683.
65 Y. Zhang, Y. Dou, Z. Ye, W. Xue, F. Liu, M. Yan, W. Wang and Y. Yin, *Small*, 2023, 2310962, DOI: 10.1002/smll.202310962.
66 H. Gao, X. Zhao and S. Chen, *Molecules*, 2018, **23**, 419.
67 F. Ye, Y. Liu, J. Chen, S. H. Liu, W. Zhao and J. Yin, *Org. Lett.*, 2019, **21**, 7213–7217.
68 B. Garg, T. Bisht and S. M. S. Chauhan, *New J. Chem.*, 2010, **34**, 1251–1254.
69 X. Liu, D. Huang, C. Lai, G. Zeng, L. Qin, H. Wang, H. Yi, B. Li, S. Liu and M. Zhang, *Chem. Soc. Rev.*, 2019, **48**, 5266–5302.
70 C. Ji, Y. Zhou, R. M. Leblanc and Z. Peng, *ACS Sens.*, 2020, **5**, 2724–2741.
71 H. Imai, N. Tochimoto, Y. Nishino, Y. Takezawa and Y. Oaki, *Cryst. Growth Des.*, 2012, **12**, 876–882.
72 B. Zargar and A. Hatamie, *Anal. Methods*, 2014, **6**, 5951–5956.
73 Z. Jin, Y. Su and Y. Duan, *Sens. Actuators, B*, 2000, **71**, 118–122.
74 W. Yim, J. Zhou, L. Sasi, J. Zhao, J. Yeung, Y. Cheng, Z. Jin, W. Johnson, M. Xu, J. Palma-Chavez, L. Fu, B. Qi, M. Retout, N. J. Shah, J. Bae and J. V. Jokerst, *Adv. Mater.*, 2023, **35**, 2206385.
75 Y.-S. Lim, J. S. Kim, J. H. Choi, J. M. Kim and T. S. Shim, *Colloid Interface Sci. Commun.*, 2022, **48**, 100624.
76 W. Yim, K. Takemura, J. Zhou, J. Zhou, Z. Jin, R. M. Borum, M. Xu, Y. Cheng, T. He and W. Penny, *ACS Nano*, 2021, **16**, 683–693.
77 L. Ascherl, E. W. Evans, M. Hennemann, D. Di Nuzzo, A. G. Hufnagel, M. Beetz, R. H. Friend, T. Clark, T. Bein and F. Auras, *Nat. Commun.*, 2018, **9**, 3802.
78 S. Jhulki, A. M. Evans, X. L. Hao, M. W. Cooper, C. H. Feriante, J. Leisen, H. Li, D. Lam, M. C. Hersam, S. Barlow, J. L. Bredas, W. R. Dichtel and S. R. Marder, *J. Am. Chem. Soc.*, 2020, **142**, 783–791.
79 J. Xiu, C. Li and G. Wang, *J. Mol. Struct.*, 2023, **1276**, 134779.
80 E. R. Tobik, L. B. Kitfield-Vernon, R. J. Thomas, S. A. Steel, S. H. Tan, O. M. Allicock, B. L. Choate, S. Akbarzada and A. L. Wyllie, *Expert Rev. Mol. Diagn.*, 2022, **22**, 519–535.
81 D. Kakoli and N. Rosalin, *Advances in Colorimetry*, IntechOpen, Rijeka, 2023, p. 6, DOI: 10.5772/intechopen.112099.
82 V. I. Adamchuk, J. W. Hummel, M. T. Morgan and S. K. Upadhyaya, *Comput. Electron. Agric.*, 2004, **44**, 71–91.
83 T. J. Free, R. W. Tucker, K. M. Simonson, S. A. Smith, C. M. Lindgren, W. G. Pitt and B. C. Bundy, *Biosensors*, 2023, **13**, 104.
84 P. D'Orazio, *Clin. Chim. Acta*, 2011, **412**, 1749–1761.
85 J. Yu, D. Wang, V. V. Tipparaju, F. Tsow and X. Xian, *ACS Sens.*, 2021, **6**, 303–320.
86 J. A. Simerville, W. C. Maxted and J. J. Pahira, *Am. Fam. Physician*, 2005, **71**, 1153–1162.
87 J. D. Cohen, L. Li, Y. Wang, C. Thoburn, B. Afsari, L. Danilova, C. Douville, A. A. Javed, F. Wong and A. Mattox, *Science*, 2018, **359**, 926–930.
88 M. Ouyang, D. Tu, L. Tong, M. Sarwar, A. Bhimaraj, C. Li, G. L. Coté and D. Di Carlo, *Biosens. Bioelectron.*, 2021, **171**, 112621.
89 G. L. Salvagno, F. Sanchis-Gomar, A. Picanza and G. Lippi, *Crit. Rev. Clin. Lab. Sci.*, 2015, **52**, 86–105.
90 C.-Z. Zhang, X.-Q. Cheng, J.-Y. Li, P. Zhang, P. Yi, X. Xu and X.-D. Zhou, *Int. J. Oral Sci.*, 2016, **8**, 133–137.

91 M. A. G. Wallace and J. D. Pleil, *Anal. Chim. Acta*, 2018, **1024**, 18–38.
92 J. Hunt, *Immunol. Allergy Clin. North Am.*, 2007, **27**, 587–596.
93 F. Bachhuber, A. Huss, M. Senel and H. Tumani, *Sci. Rep.*, 2021, **11**, 10064.
94 W. Gao, S. Emaminejad, H. Y. Y. Nyein, S. Challa, K. Chen, A. Peck, H. M. Fahad, H. Ota, H. Shiraki and D. Kiriya, *Nature*, 2016, **529**, 509–514.
95 J. Chiou, A. H. H. Leung, H. W. Lee and W.-T. Wong, *J. Integr. Agric.*, 2015, **14**, 2243–2264.
96 R. S. Andre, L. A. Mercante, M. H. Facure, R. C. Sanfelice, L. Fugikawa-Santos, T. M. Swager and D. S. Correa, *ACS Sens.*, 2022, **7**, 2104–2131.
97 M. Brusseau, M. Ramirez-Andreotta, I. Pepper and J. Maximillian, *Environmental and pollution science*, Elsevier, 2019, pp. 477–499.
98 D. Gunjan and B. Gargi, *Int. Res. J. Environ. Sci.*, 2015, **4**, 87–90.
99 F. Karagulian, M. Barbiere, A. Kotsev, L. Spinelle, M. Gerboles, F. Lagler, N. Redon, S. Crunaire and A. Borowiak, *Atmosphere*, 2019, **10**, 506.
100 M. Schloter, O. Dilly and J. Munch, *Agric., Ecosyst. Environ.*, 2003, **98**, 255–262.
101 W. Yim, D. Cheng, S. H. Patel, R. Kou, Y. S. Meng and J. V. Jokerst, *ACS Appl. Mater. Interfaces*, 2020, **12**, 54473–54480.
102 T. W. Pittman, D. B. Decsi, C. Punyadeera and C. S. Henry, *Theranostics*, 2023, **13**, 1091.
103 J. A. Jahnke, *Continuous emission monitoring*, John Wiley & Sons, 2022.
104 J. C. Loftis and R. C. Ward, *Environ. Manage.*, 1980, **4**, 521–526.
105 J. Zhou, W. Yim, J. Zhou, Z. Jin, M. Xu, Y. Mantri, T. He, Y. Cheng, L. Fu and Z. Wu, *Biosens. Bioelectron.*, 2022, **196**, 113692.
106 H. K. Walker, W. D. Hall and J. W. Hurst, *Clinical Methods: The History, Physical, and Laboratory Examinations*, Butterworths, Boston, 1990, p. 21250045.
107 M. Grzelczak, L. M. Liz-Marzán and R. Klajn, *Chem. Soc. Rev.*, 2019, **48**, 1342–1361.
108 W. Yim, M. Retout, A. A. Chen, C. Ling, L. Amer, Z. Jin, Y. C. Chang, S. Chavez, K. Barrios, B. Lam, Z. Li, J. Zhou, L. Shi, T. A. Pascal and J. V. Jokerst, *ACS Appl. Mater. Interfaces*, 2023, **15**, 42293–42303.
109 Y.-C. Chang, Z. Jin, K. Li, J. Zhou, W. Yim, J. Yeung, Y. Cheng, M. Retout, M. N. Creyer, P. Fajtová, T. He, X. Chen, A. J. O'Donoghue and J. V. Jokerst, *Chem. Sci.*, 2023, **14**, 2659–2668.
110 T. Bian, A. Gardin, J. Gemen, L. Houben, C. Perego, B. Lee, N. Elad, Z. Chu, G. M. Pavan and R. Klajn, *Nat. Chem.*, 2021, **13**, 940–949.
111 D. Wang, B. Kowalczyk, I. Lagzi and B. A. Grzybowski, *J. Phys. Chem. Lett.*, 2010, **1**, 1459–1462.
112 Y. Liu, X. Han, L. He and Y. Yin, *Angew. Chem., Int. Ed.*, 2012, **51**, 6373–6377.
113 J. Zhou, C. Wang, P. Wang, P. B. Messersmith and H. Duan, *Chem. Mater.*, 2015, **27**, 3071–3076.
114 H. Han, J. Y. Lee and X. Lu, *Chem. Commun.*, 2013, **49**, 6122–6124.
115 A. Rahikkala, V. Aseyev, H. Tenhu, E. I. Kauppinen and J. Raula, *Biomacromolecules*, 2015, **16**, 2750–2756.
116 N. Kaur and S. Kumar, *Tetrahedron*, 2011, **67**, 9233–9264.
117 Y. Li, Y. Wang, G. Huang and J. Gao, *Chem. Rev.*, 2018, **118**, 5359–5391.
118 Z. Jin, J. Yeung, J. Zhou, M. Retout, W. Yim, P. Fajtová, B. Gosselin, I. Jabin, G. Bruylants, H. Mattoussi, A. J. O'Donoghue and J. V. Jokerst, *ACS Appl. Mater. Interfaces*, 2023, **15**, 20483–20494.
119 K. L. Gurunatha, A. C. Fournier, A. Urvoas, M. Valerio-Lepiniec, V. Marchi, P. Minard and E. Dujardin, *ACS Nano*, 2016, **10**, 3176–3185.
120 D. Wu, J. Zhou, M. N. Creyer, W. Yim, Z. Chen, P. B. Messersmith and J. V. Jokerst, *Chem. Soc. Rev.*, 2021, **50**, 4432–4483.
121 W. Yim, J. Zhou, Y. Mantri, M. N. Creyer, C. A. Moore and J. V. Jokerst, *ACS Appl. Mater. Interfaces*, 2021, **13**, 14974–14984.
122 N. M. Green, *Methods in enzymology*, Elsevier, 1990, vol. 184, pp. 51–67.
123 V. S. Ajay Piriya, P. Joseph, S. C. G. Kiruba Daniel, S. Lakshmanan, T. Kinoshita and S. Muthusamy, *Mater. Sci. Eng., C*, 2017, **78**, 1231–1245.
124 A. Jain and K. Cheng, *J. Controlled Release*, 2017, **245**, 27–40.
125 S. Sharma, H. Byrne and R. J. O'Kennedy, *Essays Biochem.*, 2016, **60**, 9–18.
126 R. Elghanian, J. J. Storhoff, R. C. Mucic, R. L. Letsinger and C. A. Mirkin, *Science*, 1997, **277**, 1078–1081.
127 O. P. Ajsuvakova, A. A. Tinkov, M. Aschner, J. B. T. Rocha, B. Michalke, M. G. Skalnaya, A. V. Skalny, M. Butnariu, M. Dadar, I. Sarac, J. Aaseth and G. Bjørklund, *Coord. Chem. Rev.*, 2020, **417**, 213343.
128 S. Ruan, W. Xiao, C. Hu, H. Zhang, J. Rao, S. Wang, X. Wang, Q. He and H. Gao, *ACS Appl. Mater. Interfaces*, 2017, **9**, 20348–20360.
129 A. F. De Fazio, A. H. El-Sagheer, J. S. Kahn, I. Nandhakumar, M. R. Burton, T. Brown, O. L. Muskens, O. Gang and A. G. Kanaras, *ACS Nano*, 2019, **13**, 5771–5777.
130 S. Borsley and E. R. Kay, *Chem. Commun.*, 2016, **52**, 9117–9120.
131 Z. Jin, J. Yeung, J. Zhou, Y. Cheng, Y. Li, Y. Mantri, T. He, W. Yim, M. Xu, Z. Wu, P. Fajtova, M. N. Creyer, C. Moore, L. Fu, W. F. Penny, A. J. O'Donoghue and J. V. Jokerst, *Chem. Mater.*, 2022, **34**, 1259–1268.
132 T. Alawsi, G. P. Mattia, Z. Al-Bawi and R. Beraldi, *Sens. Bio-Sens. Res.*, 2021, **32**, 100404.
133 H. Li, X. Wang, X. Li and H.-Z. Yu, *Anal. Chem.*, 2021, **93**, 15452–15458.
134 J. Yeung, Z. Jin, C. Ling, M. Retout, E. Barbosa da Silva, M. Damani, Y.-C. Chang, W. Yim, A. J. O'Donoghue and J. V. Jokerst, *Analyst*, 2023, **148**, 4504–4512.
135 D. A. Armbruster and T. Pry, *Clin. Biochem. Rev.*, 2008, **29**(Suppl 1), S49–S52.
136 Wearable Sensors Market Size Worth USD 5.68 Billion by 2030 at 15.20% CAGR–Report by Market Research Future

(MRFR), https://www.globenewswire.com/en/news-release/2022/12/01/2566091/0/en/Wearable-Sensors-Market-Size-Worth-USD-5-68-Billion-by-2030-at-15-20-CAGR-Report-by-Market-Research-Future-MRFR.html (accessed 05-07-2024).
137 C. Parolo, A. Sena-Torralba, J. F. Bergua, E. Calucho, C. Fuentes-Chust, L. Hu, L. Rivas, R. alvarez-Diduk, E. P. Nguyen, S. Cinti, D. Quesada-Gonzalez and A. Merkoci, *Nat. Protoc.*, 2020, **15**, 3788–3816.
138 A. V. Ivanov, I. V. Safenkova, A. V. Zherdev and B. B. Dzantiev, *Anal. Chem.*, 2021, **93**, 13641–13650.
139 B. G. Andryukov, *AIMS Microbiol.*, 2020, 280–304, DOI: 10.3934/microbiol.2020018.
140 R. L. Higgins, S. A. Rawlings, J. Case, F. Y. Lee, C. W. Chan, B. Barrick, Z. C. Burger, K.-T. J. Yeo and D. Marrinucci, *PLoS One*, 2021, **16**, e0247797.
141 nanoComposix Webinar: Lateral Flow Diagnostics and the Upcoming Revolution., https://www.fortislife.com/lateral-flow-assay-products-services (accessed 05-07-2024).
142 C. Gondhalekar, E. Biela, B. Rajwa, E. Bae, V. Patsekin, J. Sturgis, C. Reynolds, I.-J. Doh, P. Diwakar, L. Stanker, V. Zorba, X. Mao, R. Russo and J. P. Robinson, *Anal. Bioanal. Chem.*, 2020, **412**, 1291–1301.
143 J. Sivakumar, J. H. Yang, M. S. Kelly, A. Koh and D. Won, *Expert Syst. Appl.*, 2022, **210**, 118471.
144 X. Gao, J. Boryczka, P. Zheng, S. Kasani, F. Yang, E. B. Engler-Chiurazzi, J. W. Simpkins, J. G. Wigginton and N. Wu, *Biosens. Bioelectron.*, 2021, **177**, 112967.
145 R. C. Castro, M. L. M. F. S. Saraiva, J. L. M. Santos and D. S. M. Ribeiro, *Coord. Chem. Rev.*, 2021, **448**, 214181.
146 S. Yan, C. Liu, S. Fang, J. Ma, J. Qiu, D. Xu, L. Li, J. Yu, D. Li and Q. Liu, *Anal. Bioanal. Chem.*, 2020, **412**, 7881–7890.
147 I. M. Lobato and C. K. O'Sullivan, *TrAC*, 2018, **98**, 19–35.
148 H.-b Liu, X.-j Du, Y.-X. Zang, P. Li and S. Wang, *J. Agric. Food Chem.*, 2017, **65**, 10290–10299.
149 Y. Joung, K. Kim, S. Lee, B.-S. Chun, S. Lee, J. Hwang, S. Choi, T. Kang, M.-K. Lee, L. Chen and J. Choo, *ACS Sens.*, 2022, **7**, 3470–3480.
150 V. K. Singh, *Laser Induced Breakdown Spectroscopy (LIBS): concepts, instrumentation, data analysis and applications*, John Wiley & Sons, Hoboken, NJ, 2023.
151 K. Misawa, T. Yamamoto, Y. Hiruta, H. Yamazaki and D. Citterio, *ACS Sens.*, 2020, **5**, 2076–2085.
152 G. G. Morbioli, T. Mazzu-Nascimento, A. M. Stockton and E. Carrilho, *Anal. Chim. Acta*, 2017, **970**, 1–22.
153 F. Li, X. Wang, J. Liu, Y. Hu and J. He, *Sens. Actuators, B*, 2019, **288**, 266–273.
154 S. Boobphahom, M. N. Ly, V. Soum, N. Pyun, O. S. Kwon, N. Rodthongkum and K. Shin, *Molecules*, 2020, **25**, 2970.
155 A. W. Martinez, S. T. Phillips, M. J. Butte and G. M. Whitesides, *Angew. Chem., Int. Ed.*, 2007, **46**, 1318–1320.
156 X. Fu, H. Lin, J. Qi, F. Li, Y. Chen, B. Li and L. Chen, *Sens. Actuators, B*, 2022, **362**, 131830.
157 M. Andersson and C. P. Braegger, *Endocr. Rev.*, 2022, **43**, 469–506.
158 J. Yi and Y. Xianyu, *Adv. Mater. Technol.*, 2023, **8**, 2300058.
159 P. Teengam, W. Siangproh, A. Tuantranont, T. Vilaivan, O. Chailapakul and C. S. Henry, *Anal. Chem.*, 2017, **89**, 5428–5435.
160 K. E. Boehle, C. S. Carrell, J. Caraway and C. S. Henry, *ACS Sens.*, 2018, **3**, 1299–1307.
161 T. Pomili, P. Donati and P. P. Pompa, *Biosensors*, 2021, **11**, 443.
162 A. W. Martinez, S. T. Phillips, G. M. Whitesides and E. Carrilho, *Anal. Chem.*, 2010, **82**, 3–10.
163 Y.-L. T. Ngo, P. L. Nguyen, J. Jana, W. M. Choi, J. S. Chung and S. H. Hur, *Anal. Chim. Acta*, 2021, **1147**, 187–198.
164 S. Ohta, R. Hiraoka, Y. Hiruta and D. Citterio, *Lab Chip*, 2022, **22**, 717–726.
165 K. Khachornsakkul, F. J. Rybicki and S. Sonkusale, *Talanta*, 2023, 124538.
166 C. Park, H.-R. Kim, S.-K. Kim, I.-K. Jeong, J.-C. Pyun and S. Park, *ACS Appl. Mater. Interfaces*, 2019, **11**, 36428–36434.
167 S. Nishat, A. T. Jafry, A. W. Martinez and F. R. Awan, *Sens. Actuators, B*, 2021, **336**, 129681.
168 R. Ghaffari, D. S. Yang, J. Kim, A. Mansour, J. A. Wright Jr., J. B. Model, D. E. Wright, J. A. Rogers and T. R. Ray, *ACS Sens.*, 2021, **6**, 2787–2801.
169 G. Chen, X. Xiao, X. Zhao, T. Tat, M. Bick and J. Chen, *Chem. Rev.*, 2022, **122**, 3259–3291.
170 W. Wang, C. Wu, K. Zhu, F. Chen, J. Zhou, Y. Shi, C. Zhang, R. Li, M. Wu, S. Zhuo, H. Zhang and P. Wang, *ACS Appl. Polym. Mater.*, 2021, **3**, 1747–1755.
171 J. Chen, H. Wen, G. Zhang, F. Lei, Q. Feng, Y. Liu, X. Cao and H. Dong, *ACS Appl. Mater. Interfaces*, 2020, **12**, 7565–7574.
172 H. Liu, L. Yu, B. Zhao, Y. Ni, P. Gu, H. Qiu, W. Zhang and K. Chen, *J. Mater. Chem. C*, 2023, **11**, 285–298.
173 Z. Wei, Z. K. Zhou, Q. Li, J. Xue, A. Di Falco, Z. Yang, J. Zhou and X. Wang, *Small*, 2017, **13**, 1700109.
174 X. Shi, Z. Deng, P. Zhang, Y. Wang, G. Zhou and L. T. Haan, *Adv. Funct. Mater.*, 2021, **31**, 2104641.
175 J. Choi, A. J. Bandodkar, J. T. Reeder, T. R. Ray, A. Turnquist, S. B. Kim, N. Nyberg, A. Hourlier-Fargette, J. B. Model, A. J. Aranyosi, S. Xu, R. Ghaffari and J. A. Rogers, *ACS Sens.*, 2019, **4**, 379–388.
176 T. R. Ray, M. Ivanovic, P. M. Curtis, D. Franklin, K. Guventurk, W. J. Jeang, J. Chafetz, H. Gaertner, G. Young, S. Rebollo, J. B. Model, S. P. Lee, J. Ciraldo, J. T. Reeder, A. Hourlier-Fargette, A. J. Bandodkar, J. Choi, A. J. Aranyosi, R. Ghaffari, S. A. McColley, S. Haymond and J. A. Rogers, *Sci. Transl. Med.*, 2021, **13**, 1946–6234.
177 Y. Liu, H. Li, Q. Feng, H. Su, D. Li, Y. Shang, H. Chen, B. Li and H. Dong, *ACS Omega*, 2022, **7**, 9834–9845.
178 N. Mishra, N. T. Garland, K. A. Hewett, M. Shamsi, M. D. Dickey and A. J. Bandodkar, *ACS Sens.*, 2022, **7**, 3169–3180.
179 J. Leanpolchareanchai and N. Nuchtavorn, *Talanta Open*, 2023, **8**, 100247.
180 H. Chang, M. Zheng, X. Yu, A. Than, R. Z. Seeni, R. Kang, J. Tian, D. P. Khanh, L. Liu, P. Chen and C. Xu, *Adv. Mater.*, 2017, **29**, 1702243.
181 R. He, H. Liu, T. Fang, Y. Niu, H. Zhang, F. Han, B. Gao, F. Li and F. Xu, *Adv. Sci.*, 2021, **8**, 2103030.

182 P. Zhang, X. Wu, H. Xue, Y. Wang, X. Luo and L. Wang, *Anal. Chim. Acta*, 2022, **1212**, 339911.
183 Z. Jin, A. Jorns, W. Yim, R. Wing, Y. Mantri, J. Zhou, J. Zhou, Z. Wu, C. Moore, W. F. Penny and J. V. Jokerst, *Anal. Chem.*, 2021, **93**, 11025–11032.
184 X. He, Q. Pei, T. Xu and X. Zhang, *Sens. Actuators, B*, 2020, **304**, 127415.
185 F. Han, T. Wang, G. Liu, H. Liu, X. Xie, Z. Wei, J. Li, C. Jiang, Y. He and F. Xu, *Adv. Mater.*, 2022, **34**, e2109055.
186 M. E. Germain and M. J. Knapp, *Chem. Soc. Rev.*, 2009, **38**, 2543–2555.
187 W. J. Peveler, A. Roldan, N. Hollingsworth, M. J. Porter and I. P. Parkin, *ACS Nano*, 2016, **10**, 1139–1146.
188 K. L. Diehl and E. V. Anslyn, *Chem. Soc. Rev.*, 2013, **42**, 8596–8611.
189 S. H. Lim, L. Feng, J. W. Kemling, C. J. Musto and K. S. Suslick, *Nat. Chem.*, 2009, **1**, 562–567.
190 Z. Zhang, D. S. Kim, C.-Y. Lin, H. Zhang, A. D. Lammer, V. M. Lynch, I. Popov, O. Š. Miljanić, E. V. Anslyn and J. L. Sessler, *J. Am. Chem. Soc.*, 2015, **137**, 7769–7774.
191 X. Zhong, D. Huo, H. Fa, X. Luo, Y. Wang, Y. Zhao and C. Hou, *Sens. Actuators, B*, 2018, **274**, 464–471.
192 A. Hannon, Y. Lu, J. Li and M. Meyyappan, *Sensors*, 2016, **16**, 1163.
193 F. Li, C. Stewart, S. Yang, F. Shi, W. Cui, S. Zhang, H. Wang, H. Huang, M. Chen and J. Han, *Front. Chem.*, 2022, **10**, 874864.
194 Y. Jin, N. Du, Y. Huang, W. Shen, Y. Tan, Y. Z. Chen, W.-T. Dou, X.-P. He, Z. Yang, N. Xu and C. Tan, *ACS Sens.*, 2022, **7**, 1524–1532.
195 Z. Lu, N. Lu, Y. Xiao, Y. Zhang, Z. Tang and M. Zhang, *ACS Appl. Mater. Interfaces*, 2022, **14**, 11156–11166.
196 B. Li, X. Li, Y. Dong, B. Wang, D. Li, Y. Shi and Y. Wu, *Anal. Chem.*, 2017, **89**, 10639–10643.
197 W. He, L. Luo, Q. Liu and Z. Chen, *Anal. Chem.*, 2018, **90**, 4770–4775.
198 H. Lin and K. S. Suslick, *J. Am. Chem. Soc.*, 2010, **132**, 15519–15521.
199 K. S. Suslick, *MRS Bull.*, 2004, **29**, 720–725.
200 Y. Liu, T. Minami, R. Nishiyabu, Z. Wang and P. Anzenbacher, Jr., *J. Am. Chem. Soc.*, 2013, **135**, 7705–7712.
201 J. Jia, S. Zhang, L. Ma, L. Zheng, S. Yu, C. Shen, H. Fu, S. Wang and Y. She, *Sci. Rep.*, 2022, **12**, 18596.
202 N. T. Greene and K. D. Shimizu, *J. Am. Chem. Soc.*, 2005, **127**, 5695–5700.
203 A. Bajaj, O. R. Miranda, I.-B. Kim, R. L. Phillips, D. J. Jerry, U. H. F. Bunz and V. M. Rotello, *Proc. Natl. Acad. Sci. U. S. A.*, 2009, **106**, 10912–10916.
204 Y. Lu, Y. Liu, S. Zhang, S. Wang, S. Zhang and X. Zhang, *Anal. Chem.*, 2013, **85**, 6571–6574.
205 H. Xi, W. He, Q. Liu and Z. Chen, *ACS Sustainable Chem. Eng.*, 2018, **6**, 10751–10757.
206 Y. Si, L. Xu, N. Wang, J. Zheng, R. Yang and J. Li, *Anal. Chem.*, 2020, **92**, 2649–2655.
207 R. Tullius, G. W. Platt, L. Khosravi Khorashad, N. Gadegaard, A. J. Lapthorn, V. M. Rotello, G. Cooke, L. D. Barron, A. O. Govorov, A. S. Karimullah and M. Kadodwala, *ACS Nano*, 2017, **11**, 12049–12056.
208 M. J. Baker, J. Trevisan, P. Bassan, R. Bhargava, H. J. Butler, K. M. Dorling, P. R. Fielden, S. W. Fogarty, N. J. Fullwood, K. A. Heys, C. Hughes, P. Lasch, P. L. Martin-Hirsch, B. Obinaju, G. D. Sockalingum, J. Sulé-Suso, R. J. Strong, M. J. Walsh, B. R. Wood, P. Gardner and F. L. Martin, *Nat. Protoc.*, 2014, **9**, 1771–1791.
209 B. Wolfrum, E. Kätelhön, A. Yakushenko, K. J. Krause, N. Adly, M. Hüske and P. Rinklin, *Acc. Chem. Res.*, 2016, **49**, 2031–2040.
210 M. Retout, H. Valkenier, E. Triffaux, T. Doneux, K. Bartik and G. Bruylants, *ACS Sens.*, 2016, **1**, 929–933.
211 S. Karamizadeh, S. M. Abdullah, A. A. Manaf, M. Zamani and A. Hooman, *J. Signal Process. Syst.*, 2013, **4**, 173.
212 A. Izenman, G. Casella, S. Fienberg and I. Olkin, *Modern Multivariate Statistical Techniques*, 2008, pp. 107–190.
213 Y. Geng, J. Hardie, R. F. Landis, J. A. Mas-Rosario, A. N. Chattopadhyay, P. Keshri, J. Sun, E. M. Rizzo, S. Gopalakrishnan, M. E. Farkas and V. M. Rotello, *Chem. Sci.*, 2020, **11**, 8231–8239.
214 G. Sener, L. Uzun and A. Denizli, *ACS Appl. Mater. Interfaces*, 2014, **6**, 18395–18400.
215 C. K. Dixit, S. K. Vashist, F. T. O'Neill, B. O'Reilly, B. D. MacCraith and R. O'Kennedy, *Anal. Chem.*, 2010, **82**, 7049–7052.
216 A. Bajaj, S. Rana, O. R. Miranda, J. C. Yawe, D. J. Jerry, U. H. F. Bunz and V. M. Rotello, *Chem. Sci.*, 2010, **1**, 134–138.
217 M. Al-Hajj, M. S. Wicha, A. Benito-Hernandez, S. J. Morrison and M. F. Clarke, *Proc. Natl. Acad. Sci. U. S. A.*, 2003, **100**, 3983–3988.
218 X. Yang, J. Li, H. Pei, Y. Zhao, X. Zuo, C. Fan and Q. Huang, *Anal. Chem.*, 2014, **86**, 3227–3231.
219 M. Jiang, A. N. Chattopadhyay, Y. Geng and V. M. Rotello, *Chem. Commun.*, 2022, **58**, 2890–2893.
220 D. Li, Y. Dong, B. Li, Y. Wu, K. Wang and S. Zhang, *Analyst*, 2015, **140**, 7672–7677.
221 X. Gao, M. Li, M. Zhao, X. Wang, S. Wang and Y. Liu, *Anal. Chem.*, 2022, **94**, 6957–6966.
222 P. J. Mazzone, J. Hammel, R. Dweik, J. Na, C. Czich, D. Laskowski and T. Mekhail, *Thorax*, 2007, **62**, 565–568.
223 P. J. Mazzone, X.-F. Wang, Y. Xu, T. Mekhail, M. C. Beukemann, J. Na, J. W. Kemling, K. S. Suslick and M. Sasidhar, *J. Thorac. Oncol.*, 2012, **7**, 137–142.
224 M. M. Bordbar, H. Samadinia, A. Hajian, A. Sheini, E. Safaei, J. Aboonajmi, F. Arduini, H. Sharghi, P. Hashemi, H. Khoshsafar, M. Ghanei and H. Bagheri, *Sens. Actuators, B*, 2022, **369**, 132379.
225 G. Şener and A. Denizli, in *Biomimetic Sensing: Methods and Protocols*, ed. J. E. Fitzgerald and H. Fenniri, Springer, New York, New York, NY, 2019, pp. 75–80, DOI: **10.1007/978-1-4939-9616-2_6**.
226 J. R. Carey, K. S. Suslick, K. I. Hulkower, J. A. Imlay, K. R. C. Imlay, C. K. Ingison, J. B. Ponder, A. Sen and A. E. Wittrig, *J. Am. Chem. Soc.*, 2011, **133**, 7571–7576.

227 Y. Zhang, S. He, W. Chen, Y. Liu, X. Zhang, Q. Miao and K. Pu, *Angew. Chem., Int. Ed.*, 2021, **60**, 5921–5927.
228 X. Sun, S. D. Dahlhauser and E. V. Anslyn, *J. Am. Chem. Soc.*, 2017, **139**, 4635–4638.
229 Acid-base indicator chart, **https://theory.labster.com/acid-base-indicator-chart/** (accessed 05-07-2024).
230 L. Cruz, N. Basílio, N. Mateus, V. de Freitas and F. Pina, *Chem. Rev.*, 2022, **122**, 1416–1481.
231 J. Oliveira, N. Mateus and V. de Freitas, *Tetrahedron Lett.*, 2013, **54**, 5106–5110.
232 A. Alejo-Armijo, J. Mendoza, A. J. Parola and F. Pina, *Phytochemistry*, 2020, **174**, 112339.
233 F. Le Guern, V. Mussard, A. Gaucher, M. Rottman and D. Prim, *Int. J. Mol. Sci.*, 2020, **21**, 9217.
234 J. Han and K. Burgess, *Chem. Rev.*, 2010, **110**, 2709–2728.
235 J. Nam, N. Won, H. Jin, H. Chung and S. Kim, *J. Am. Chem. Soc.*, 2009, **131**, 13639–13645.
236 S. K. Kim, K. M. K. Swamy, S.-Y. Chung, H. N. Kim, M. J. Kim, Y. Jeong and J. Yoon, *Tetrahedron Lett.*, 2010, **51**, 3286–3289.
237 R. G. Pearson, *J. Am. Chem. Soc.*, 1963, **85**, 3533–3539.
238 E. Kim, S. Seo, M. L. Seo and J. H. Jung, *Analyst*, 2010, **135**, 149–156.
239 X. Cheng, Q. Li, C. Li, J. Qin and Z. Li, *Chem. – Eur. J.*, 2011, **17**, 7276–7281.
240 B.-W. Liu, Y. Chen, B.-E. Song and Y. Liu, *Chem. Commun.*, 2011, **47**, 4418–4420.
241 D. Liu, W. Qu, W. Chen, W. Zhang, Z. Wang and X. Jiang, *Anal. Chem.*, 2010, **82**, 9606–9610.
242 J.-S. Lee, M. S. Han and C. A. Mirkin, *Angew. Chem., Int. Ed.*, 2007, **46**, 4093–4096.
243 G.-H. Chen, W.-Y. Chen, Y.-C. Yen, C.-W. Wang, H.-T. Chang and C.-F. Chen, *Anal. Chem.*, 2014, **86**, 6843–6849.
244 M. G. Coulthard, *Pediatr. Nephrol.*, 2019, **34**, 1283–1288.
245 V. S. Siu, M. Lu, K. Y. Hsieh, K. Raines, Y. A. Asaad, K. Patel, A. Afzali-Ardakani, B. Wen and R. Budd, *ACS Omega*, 2022, **7**, 11126–11134.
246 W. L. Daniel, M. S. Han, J.-S. Lee and C. A. Mirkin, *J. Am. Chem. Soc.*, 2009, **131**, 6362–6363.
247 Y. Ye, Y. Guo, Y. Yue and Y. Zhang, *Anal. Methods*, 2015, **7**, 4090–4096.
248 Cyanide and drinking water fact sheet, **https://www.health.nsw.gov.au/environment/water/Pages/cyanide.aspx#** (accessed 05-07-2024).
249 M. Tomasulo and F. M. Raymo, *Org. Lett.*, 2005, **7**, 4633–4636.
250 X. Lv, J. Liu, Y. Liu, Y. Zhao, M. Chen, P. Wang and W. Guo, *Sens. Actuators, B*, 2011, **158**, 405–410.
251 X. Cheng, Y. Zhou, J. Qin and Z. Li, *ACS Appl. Mater. Interfaces*, 2012, **4**, 2133–2138.
252 J.-B. Zeng, Y.-Y. Cao, J.-J. Chen, X.-D. Wang, J.-F. Yu, B.-B. Yu, Z.-F. Yan and X. Chen, *Nanoscale*, 2014, **6**, 9939–9943.
253 R. Rajamanikandan, K. Shanmugaraj, M. Ilanchelian and H. Ju, *Chemosphere*, 2023, **316**, 137836.
254 B. Zhu, Y. Xu, W. Liu, C. Shao, H. Wu, H. Jiang, B. Du and X. Zhang, *Sens. Actuators, B*, 2014, **191**, 473–478.
255 T. Kim, Q. Zhang, J. Li, L. Zhang and J. V. Jokerst, *ACS Nano*, 2018, **12**, 5615–5625.
256 X. Chen, Y. Zhou, X. Peng and J. Yoon, *Chem. Soc. Rev.*, 2010, **39**, 2120–2135.
257 Z. Fu, S. Li, S. Han, C. Shi and Y. Zhang, *Signal Transduction Targeted Ther.*, 2022, **7**, 93.
258 D. Mishra, S. Wang, S. Michel, G. Palui, N. Zhan, W. Perng, Z. Jin and H. Mattoussi, *Phys. Chem. Chem. Phys.*, 2018, **20**, 3895–3902.
259 F.-J. Huo, Y.-Q. Sun, J. Su, J.-B. Chao, H.-J. Zhi and C.-X. Yin, *Org. Lett.*, 2009, **11**, 4918–4921.
260 Y. Shiraishi, K. Yamamoto, S. Sumiya and T. Hirai, *Phys. Chem. Chem. Phys.*, 2014, **16**, 12137–12142.
261 W. Wang, O. Rusin, X. Xu, K. K. Kim, J. O. Escobedo, S. O. Fakayode, K. A. Fletcher, M. Lowry, C. M. Schowalter, C. M. Lawrence, F. R. Fronczek, I. M. Warner and R. M. Strongin, *J. Am. Chem. Soc.*, 2005, **127**, 15949–15958.
262 Y. Hua, Z. Zou, P. Alessandro, T. R. Ward, M. Mayor and V. Köhler, *ChemRxiv*, 2023, preprint, DOI: **10.26434/chemrxiv-22023-26483gph**.
263 J.-S. Lee, P. A. Ulmann, M. S. Han and C. A. Mirkin, *Nano Lett.*, 2008, **8**, 529–533.
264 A. Kapur, F. Aldeek, X. Ji, M. Safi, W. Wang, A. Del Cid, O. Steinbock and H. Mattoussi, *Bioconjugate Chem.*, 2017, **28**, 678–687.
265 Z.-J. Li, X.-J. Zheng, L. Zhang, R.-P. Liang, Z.-M. Li and J.-D. Qiu, *Biosens. Bioelectron.*, 2015, **68**, 668–674.
266 J. Matsui, K. Akamatsu, S. Nishiguchi, D. Miyoshi, H. Nawafune, K. Tamaki and N. Sugimoto, *Anal. Chem.*, 2004, **76**, 1310–1315.
267 Z. Chen, Y. Hu, Q. Yang, C. Wan, Y. Tan and H. Ma, *Sens. Actuators, B*, 2015, **207**, 277–280.
268 N. Saraf, A. Bosak, A. Willenberg, S. Das, B. J. Willenberg and S. Seal, *RSC Adv.*, 2017, **7**, 49133–49143.
269 Ö. Kap, V. Kılıç, J. G. Hardy and N. Horzum, *Analyst*, 2021, **146**, 2784–2806.
270 B. Kovatchev, *Trends Endocrinol. Metab.*, 2019, **30**, 432–444.
271 K. Tonyushkina and J. H. Nichols, *J. Diabetes Sci. Technol.*, 2009, **3**, 971–980.
272 J. Dai, H. Zhang, C. Huang, Z. Chen and A. Han, *Anal. Chem.*, 2020, **92**, 16122–16129.
273 A. K. Yetisen, R. Moreddu, S. Seifi, N. Jiang, K. Vega, X. Dong, J. Dong, H. Butt, M. Jakobi, M. Elsner and A. W. Koch, *Angew. Chem., Int. Ed.*, 2019, **58**, 10506–10513.
274 T. Pinheiro, A. C. Marques, P. Carvalho, R. Martins and E. Fortunato, *ACS Appl. Mater. Interfaces*, 2021, **13**, 3576–3590.
275 B. Kong, A. Zhu, Y. Luo, Y. Tian, Y. Yu and G. Shi, *Angew. Chem., Int. Ed.*, 2011, **50**, 1837–1840.
276 T. D. Tran, P. T. Nguyen, T. N. Le and M. I. Kim, *Biosens. Bioelectron.*, 2021, **182**, 113187.
277 L. Zhang, Y. Jin, H. Mao, L. Zheng, J. Zhao, Y. Peng, S. Du and Z. Zhang, *Biosens. Bioelectron.*, 2014, **58**, 165–171.
278 V. D. Chavada, N. M. Bhatt, M. Sanyal and P. S. Shrivastav, *Spectrochim. Acta, Part A*, 2017, **170**, 97–103.
279 M. A. Abedalwafa, Y. Li, C. Ni and L. Wang, *Anal. Methods*, 2019, **11**, 2836–2854.

280 Q. H. Nguyen and M. I. Kim, *BioChip J.*, 2021, **15**, 123–134.
281 D. Wang, X. Ai, Y. Duan, N. Xian, R. H. Fang, W. Gao and L. Zhang, *ACS Nano*, 2022, **16**, 19145–19154.
282 Y. Huang, A. Xu, Y. Xu, H. Wu, M. Sun, L. Madushika, R. Wang, S. Wang and S. Ling, *Front. Bioeng. Biotechnol.*, 2023, **11**, 698.
283 C. L. O'Neal, D. J. Crouch and A. A. Fatah, *Forensic Sci. Int.*, 2000, **109**, 189–201.
284 National Institute of Justice, Office of Science and Technology, 2000, NIJ Standard 0604.01.
285 CopQuest, NIK Presumptive Test Kits Test Descriptions and Summaries, **https://www.copquest.com/copquest_nik_summary.pdf** (accessed 05-07-2024).
286 M. J. Kangas, *Org. Med. Chem. Int. J.*, 2017, **4**, 555645.
287 M. Hu, Q. Han and B. Xing, *ChemBiochem*, 2020, **21**, 2512–2517.
288 R. Neijzen, P. v Ardenne, M. Sikma, A. Egas, T. Ververs and E. v Maarseveen, *Eur. J. Pharm. Sci.*, 2012, **47**, 801–803.
289 N. L. Rosi and C. A. Mirkin, *Chem. Rev.*, 2005, **105**, 1547–1562.
290 C. A. Mirkin, R. L. Letsinger, R. C. Mucic and J. J. Storhoff, *Nature*, 1996, **382**, 607–609.
291 R. Elghanian, J. J. Storhoff, R. C. Mucic, R. L. Letsinger and C. A. Mirkin, *Science*, 1997, **277**, 1078–1081.
292 L. Guo, Y. Xu, A. R. Ferhan, G. Chen and D.-H. Kim, *J. Am. Chem. Soc.*, 2013, **135**, 12338–12345.
293 M. S. Han, A. K. R. Lytton-Jean and C. A. Mirkin, *J. Am. Chem. Soc.*, 2006, **128**, 4954–4955.
294 R. Cao, B. Li, Y. Zhang and Z. Zhang, *Chem. Commun.*, 2011, **47**, 12301–12303.
295 H. Li and L. Rothberg, *Proc. Natl. Acad. Sci. U. S. A.*, 2004, **101**, 14036–14039.
296 F. Xia, X. Zuo, R. Yang, Y. Xiao, D. Kang, A. Vallée-Bélisle, X. Gong, J. D. Yuen, B. B. Y. Hsu, A. J. Heeger and K. W. Plaxco, *Proc. Natl. Acad. Sci. U. S. A.*, 2010, **107**, 10837–10841.
297 W. Zhou, K. Hu, S. Kwee, L. Tang, Z. Wang, J. Xia and X. Li, *Anal. Chem.*, 2020, **92**, 2739–2747.
298 P. Liu, X. Yang, S. Sun, Q. Wang, K. Wang, J. Huang, J. Liu and L. He, *Anal. Chem.*, 2013, **85**, 7689–7695.
299 M. Larguinho, R. Canto, M. Cordeiro, P. Pedrosa, A. Fortuna, R. Vinhas and P. V. Baptista, *Expert Rev. Mol. Diagn.*, 2015, **15**, 1355–1368.
300 S. Hu, P.-J. J. Huang, J. Wang and J. Liu, *Anal. Chem.*, 2020, **92**, 13354–13360.
301 G. Wang, Y. Akiyama, S. Shiraishi, N. Kanayama, T. Takarada and M. Maeda, *Bioconjugate Chem.*, 2017, **28**, 270–277.
302 K. Dighe, P. Moitra, M. Alafeef, N. Gunaseelan and D. Pan, *Biosens. Bioelectron.*, 2022, **200**, 113900.
303 C. Zhang, T. Zheng, H. Wang, W. Chen, X. Huang, J. Liang, L. Qiu, D. Han and W. Tan, *Anal. Chem.*, 2021, **93**, 3325–3330.
304 E. Xiong, L. Jiang, T. Tian, M. Hu, H. Yue, M. Huang, W. Lin, Y. Jiang, D. Zhu and X. Zhou, *Angew. Chem., Int. Ed.*, 2021, **60**, 5307–5315.
305 M. Alafeef, P. Moitra, K. Dighe and D. Pan, *Nat. Protoc.*, 2021, **16**, 3141–3162.
306 P. Q. Nguyen, L. R. Soenksen, N. M. Donghia, N. M. Angenent-Mari, H. de Puig, A. Huang, R. Lee, S. Slomovic, T. Galbersanini, G. Lansberry, H. M. Sallum, E. M. Zhao, J. B. Niemi and J. J. Collins, *Nat. Biotechnol.*, 2021, **39**, 1366–1374.
307 T. Zhang, R. Deng, Y. Wang, C. Wu, K. Zhang, C. Wang, N. Gong, R. Ledesma-Amaro, X. Teng, C. Yang, T. Xue, Y. Zhang, Y. Hu, Q. He, W. Li and J. Li, *Nat. Biomed. Eng.*, 2022, **6**, 957–967.
308 A. Levin, T. A. Hakala, L. Schnaider, G. J. L. Bernardes, E. Gazit and T. P. J. Knowles, *Nat. Rev. Chem.*, 2020, **4**, 615–634.
309 G. Ashraf, M. McGuinness, M. A. Khan, C. Obtinalla, X. Hadoux and P. van Wijngaarden, *Alzheimer's Dement.: Diagn. Assess. Dis. Monit.*, 2023, **15**, e12421.
310 Y. Li, J. Yang, H. Liu, J. Yang, L. Du, H. Feng, Y. Tian, J. Cao and C. Ran, *Chem. Sci.*, 2017, **8**, 7710–7717.
311 G. P. Morris, I. A. Clark and B. Vissel, *Acta Neuropathol.*, 2018, **136**, 663–689.
312 X. Zhang, Y. Tian, Z. Li, X. Tian, H. Sun, H. Liu, A. Moore and C. Ran, *J. Am. Chem. Soc.*, 2013, **135**, 16397–16409.
313 Y. Zhou, H. Dong, L. Liu and M. Xu, *Small*, 2015, **11**, 2144–2149.
314 F. Ghasemi, M. R. Hormozi-Nezhad and M. Mahmoudi, *Nanoscale*, 2018, **10**, 6361–6368.
315 I. Choi and L. P. Lee, *ACS Nano*, 2013, **7**, 6268–6277.
316 L. C. Brazaca, J. R. Moreto, A. Martín, F. Tehrani, J. Wang and V. Zucolotto, *ACS Nano*, 2019, **13**, 13325–13332.
317 G. Osikowicz, M. Beggs, P. Brookhart, D. Caplan, S. Ching, P. Eck, J. Gordon, R. Richerson, S. Sampedro and D. Stimpson, *et al.*, *Clin. Chem.*, 1990, **36**, 1586.
318 A. Rubio-Monterde, D. Quesada-González and A. Merkoçi, *Anal. Chem.*, 2023, **95**, 468–489.
319 R. Tanaka, T. Yuhi, N. Nagatani, T. Endo, K. Kerman, Y. Takamura and E. Tamiya, *Anal. Bioanal. Chem.*, 2006, **385**, 1414–1420.
320 E. Vargas, P. Nandhakumar, S. Ding, T. Saha and J. Wang, *Nat. Rev. Endocrinol.*, 2023, **19**, 487–495.
321 D. W. Jekarl, H. Choi, E. S. Kim, S. Lee, H.-I. Park, M. Kim and Y. Kim, *Scand. J. Clin. Lab. Invest.*, 2019, **79**, 347–353.
322 H.-Y. Kim, J.-H. Lee, M. J. Kim, S. C. Park, M. Choi, W. Lee, K. B. Ku, B. T. Kim, E. Changkyun Park, H. G. Kim and S. I. Kim, *Biosens. Bioelectron.*, 2021, **175**, 112868.
323 F. Ghorbanizamani, H. Moulahoum, F. Zihnioglu, S. Evran, C. Cicek, R. Sertoz, B. Arda, T. Goksel, K. Turhan and S. Timur, *Biosens. Bioelectron.*, 2021, **192**, 113484.
324 Q. Zhu and X. Zhou, *J. Hazard. Mater.*, 2022, **425**, 127923.
325 Y. Zhang, Y. Chai, Z. Hu, Z. Xu, M. Li, X. Chen, C. Yang and J. Liu, *Front. Bioeng. Biotechnol.*, 2022, **10**, 866368.
326 Z. Li, Y. Yi, X. Luo, N. Xiong, Y. Liu, S. Li, R. Sun, Y. Wang, B. Hu, W. Chen, Y. Zhang, J. Wang, B. Huang, Y. Lin, J. Yang, W. Cai, X. Wang, J. Cheng, Z. Chen, K. Sun, W. Pan, Z. Zhan, L. Chen and F. Ye, *J. Med. Virol.*, 2020, **92**, 1518–1524.
327 D. Jacofsky, E. M. Jacofsky and M. Jacofsky, *J. Arthroplasty*, 2020, **35**, S74–S81.

328 T. R. Mercer and M. Salit, *Nat. Rev. Genet.*, 2021, **22**, 415–426.
329 Z. Jin, X. Du, Y. Xu, Y. Deng, M. Liu, Y. Zhao, B. Zhang, X. Li, L. Zhang and H. Yang, *Nature*, 2020, **582**, 289–293.
330 R. E. Vandenbroucke and C. Libert, *Nat. Rev. Drug Discovery*, 2014, **13**, 904.
331 A. G. Porter and R. U. Jänicke, *Cell Death Differ.*, 1999, **6**, 99–104.
332 S. A. Castro, R. Collighan, P. A. Lambert, I. H. K. Dias, P. Chauhan, C. E. Bland, I. Milic, M. R. Milward, P. R. Cooper and A. Devitt, *Cell Death Dis.*, 2017, **8**, e2644–e2644.
333 D. Chowdhury and J. Lieberman, *Annu. Rev. Immunol.*, 2008, **26**, 389–420.
334 R. Sheyi, B. G. de la Torre and F. Albericio, *Pharmaceutics*, 2022, **14**, 396.
335 C. Guarise, L. Pasquato, V. De Filippis and P. Scrimin, *Proc. Natl. Acad. Sci. U. S. A.*, 2006, **103**, 3978–3982.
336 M. N. Creyer, Z. Jin, M. Retout, W. Yim, J. Zhou and J. V. Jokerst, *Langmuir*, 2022, **38**, 14200–14207.
337 G. B. Kim, K. H. Kim, Y. H. Park, S. Ko and Y.-P. Kim, *Biosens. Bioelectron.*, 2013, **41**, 833–839.
338 M. N. Holme, S. Rana, H. M. G. Barriga, U. Kauscher, N. J. Brooks and M. M. Stevens, *ACS Nano*, 2018, **12**, 8197–8207.
339 W. Zhao, W. Chiuman, J. C. F. Lam, M. A. Brook and Y. Li, *Chem. Commun.*, 2007, 3729–3731, DOI: **10.1039/B705335E**.
340 Y. Choi, N.-H. Ho and C.-H. Tung, *Angew. Chem., Int. Ed.*, 2007, **46**, 707–709.
341 R. H. Huang, N. Nayeem, Y. He, J. Morales, D. Graham, R. Klajn, M. Contel, S. O'Brien and R. V. Ulijn, *Adv. Mater.*, 2022, **34**, 2104962.
342 Z. Jin, Y. Li, K. Li, J. Zhou, J. Yeung, C. Ling, W. Yim, T. He, Y. Cheng, M. Xu, M. N. Creyer, Y.-C. Chang, P. Fajtová, M. Retout, B. Qi, S. Li, A. J. O'Donoghue and J. V. Jokerst, *Angew. Chem., Int. Ed.*, 2023, **135**, e202214394.
343 W. Xue, G. Zhang and D. Zhang, *Analyst*, 2011, **136**, 3136–3141.
344 A. Laromaine, L. Koh, M. Murugesan, R. V. Ulijn and M. M. Stevens, *J. Am. Chem. Soc.*, 2007, **129**, 4156–4157.
345 M. Retout, Z. Jin, J. Tsujimoto, Y. Mantri, R. Borum, M. N. Creyer, W. Yim, T. He, Y.-C. Chang and J. V. Jokerst, *ACS Appl. Mater. Interfaces*, 2022, **14**, 52553–52565.
346 M. Retout, L. Amer, W. Yim, M. N. Creyer, B. Lam, D. F. Trujillo, J. Potempa, A. J. O'Donoghue, C. Chen and J. V. Jokerst, *ACS Nano*, 2023, **17**, 17308–17319.
347 T. Serizawa, Y. Hirai and M. Aizawa, *Mol. BioSyst.*, 2010, **6**, 1565–1568.
348 M. N. Creyer, Z. Jin, C. Moore, W. Yim, J. Zhou and J. V. Jokerst, *ACS Appl. Mater. Interfaces*, 2021, **13**, 45236–45243.
349 D. J. Wornes, S. J. Speers and J. A. Murakami, *Forensic Sci. Int.*, 2018, **288**, 81–88.
350 P. D. Josephy, T. Eling and R. P. Mason, *J. Biol. Chem.*, 1982, **257**, 3669–3675.
351 D. Ye, A. J. Shuhendler, L. Cui, L. Tong, S. S. Tee, G. Tikhomirov, D. W. Felsher and J. Rao, *Nat. Chem.*, 2014, **6**, 519–526.
352 C. Ling, Z. Jin, J. Yeung, E. B. da Silva, Y.-C. Chang, T. He, W. Yim, A. J. O'Donoghue and J. V. Jokerst, *Chem. Commun.*, 2023, **59**, 12459–12462.
353 Q. Li, Z. Armstrong, A. MacRae, M. Lenertz, L. Feng and Z. Yang, *Chem. Phys. Rev.*, 2023, **4**, 041302.
354 D. Su and D. Zhang, *Front. Pharmacol.*, 2021, **12**, 687926.
355 C. E. Callmann, M. P. Thompson and N. C. Gianneschi, *Acc. Chem. Res.*, 2020, **53**, 400–413.
356 X. Li, M. Li, L. Tang, D. Shi, E. Lam and J. Bae, *Mater. Chem. Front.*, 2023, **7**, 5989–6034.
357 Z. Jin, C. Ling, W. Yim, Y.-C. Chang, T. He, K. Li, J. Zhou, Y. Cheng, Y. Li, J. Yeung, R. Wang, P. Fajtová, L. Amer, H. Mattoussi, A. J. O'Donoghue and J. V. Jokerst, *ACS Nano*, 2023, **17**, 16980–16992.
358 R. W. Tibble, A. Depaix, J. Kowalska, J. Jemielity and J. D. Gross, *Nat. Chem. Biol.*, 2021, **17**, 615–623.
359 L. Jiang, Y. Zeng, H. Li, Z. Lin, H. Liu, J. J. Richardson, Z. Gao, D. Wu, L. Liu, F. Caruso and J. Zhou, *J. Am. Chem. Soc.*, 2023, **145**, 24108–24115.
360 K. Yang, Y. Liu, Y. Wang, Q. Ren, H. Guo, J. B. Matson, X. Chen and Z. Nie, *Biomaterials*, 2019, **223**, 119460.
361 Z. Jin, C. Ling, Y. Li, J. Zhou, K. Li, W. Yim, J. Yeung, Y.-C. Chang, T. He, Y. Cheng, P. Fajtová, M. Retout, A. J. O'Donoghue and J. V. Jokerst, *Nano Lett.*, 2022, **22**, 8932–8940.
362 Z. Jin, N. Dridi, G. Palui, V. Palomo, J. V. Jokerst, P. E. Dawson, Q.-X. Amy Sang and H. Mattoussi, *J. Am. Chem. Soc.*, 2023, **145**, 4570–4582.
363 Z. Jin, N. Dridi, G. Palui, V. Palomo, J. V. Jokerst, P. E. Dawson, Q.-X. A. Sang and H. Mattoussi, *Anal. Chem.*, 2023, **95**, 2713–2722.
364 M. S. Verma, J. L. Rogowski, L. Jones and F. X. Gu, *Biotechnol. Adv.*, 2015, **33**, 666–680.
365 C. R. Quijia, R. C. Alves, G. Hanck-Silva, R. C. Galvão Frem, G. Arroyos and M. Chorilli, *Crit. Rev. Microbiol.*, 2022, **48**, 161–196.
366 Y. Sun, C. Zhao, J. Niu, J. Ren and X. Qu, *ACS Cent. Sci.*, 2020, **6**, 207–212.
367 J. Chen, A. A. Jackson, V. M. Rotello and S. R. Nugen, *Small*, 2016, **12**, 2469–2475.
368 H. Peng, R. E. Borg, A. B. N. Nguyen and I. A. Chen, *ACS Sens.*, 2020, **5**, 1491–1499.
369 A. Lesniewski, M. Los, M. Jonsson-Niedziółka, A. Krajewska, K. Szot, J. M. Los and J. Niedziolka-Jonsson, *Bioconjugate Chem.*, 2014, **25**, 644–648.
370 B. D. Ventura, M. Cennamo, A. Minopoli, R. Campanile, S. B. Censi, D. Terracciano, G. Portella and R. Velotta, *ACS Sens.*, 2020, **5**, 3043–3048.
371 E. M. Materón, F. R. Gómez, M. B. Almeida, F. M. Shimizu, A. Wong, K. B. R. Teodoro, F. S. R. Silva, M. J. A. Lima, M. K. S. C. Angelim, M. E. Melendez, N. Porras, P. M. Vieira, D. S. Correa, E. Carrilho, O. N. Oliveira, Jr., R. B. Azevedo and D. Goncalves, *ACS Appl. Mater. Interfaces*, 2022, **14**, 54527–54538.
372 P. Weerathunge, R. Ramanathan, V. A. Torok, K. Hodgson, Y. Xu, R. Goodacre, B. K. Behera and V. Bansal, *Anal. Chem.*, 2019, **91**, 3270–3276.
373 A. L. Ferreira, L. F. de Lima, M. D. T. Torres, W. R. de Araujo and C. de la Fuente-Nunez, *ACS Nano*, 2021, **15**, 17453–17462.

374 J. I. Lee, S. C. Jang, J. Chung, W.-K. Choi, C. Hong, G. R. Ahn, S. H. Kim, B. Y. Lee and W.-J. Chung, *Sens. Actuators, B*, 2021, **327**, 128894.
375 M. S. Lionakis, R. A. Drummond and T. M. Hohl, *Nat. Rev. Immunol.*, 2023, **23**, 433–452.
376 Z. Odabasi, V. L. Paetznick, J. R. Rodriguez, E. Chen, M. R. McGinnis and L. Ostrosky-Zeichner, *Med. Mycol.*, 2006, **44**, 267–272.
377 S. Morjaria, J. Frame, A. Franco-Garcia, A. Geyer, M. Kamboj and N. E. Babady, *Clin. Infect. Dis.*, 2018, **69**, 1303–1309.
378 D. J. Rotman, US10660301B1, Pretty Litter, Inc., United States, 2020.
379 K. Kim, M.-J. Kim, D. W. Kim, S. Y. Kim, S. Park and C. B. Park, *Nat. Commun.*, 2020, **11**, 119.
380 B. Gil Rosa, O. E. Akingbade, X. Guo, L. Gonzalez-Macia, M. A. Crone, L. P. Cameron, P. Freemont, K.-L. Choy, F. Güder, E. Yeatman, D. J. Sharp and B. Li, *Biosens. Bioelectron.*, 2022, **203**, 114050.
381 Y. Geng, W. J. Peveler and V. M. Rotello, *Angew. Chem., Int. Ed.*, 2019, **58**, 5190–5200.
382 Y. Zhou, X. Huang, C. Liu, R. Zhang, X. Gu, G. Guan, C. Jiang, L. Zhang, S. Du, B. Liu, M.-Y. Han and Z. Zhang, *Anal. Chem.*, 2016, **88**, 6105–6109.
383 J. Vandooren and Y. Itoh, *Front. Immunol.*, 2021, **12**, 803244.
384 E. Clarke, R. Robinson, L. B. Laurentius and M. D. Porter, *Anal. Chem.*, 2023, **95**, 9191–9198.
385 N. D. Rawlings and A. Bateman, *Protein Sci.*, 2021, **30**, 83–92.
386 L. G. Trabuco, S. Lise, E. Petsalaki and R. B. Russell, *Nucleic Acids Res.*, 2012, **40**, W423–427.
387 H. Chu, C. Liu, J. Liu, J. Yang, Y. Li and X. Zhang, *Sens. Actuators, B*, 2021, **348**, 130708.
388 V. Narasimhan, R. H. Siddique, J. O. Lee, S. Kumar, B. Ndjamen, J. Du, N. Hong, D. Sretavan and H. Choo, *Nat. Nanotechnol.*, 2018, **13**, 512–519.
389 A. Scarangella, V. Soldan and M. Mitov, *Nat. Commun.*, 2020, **11**, 4108.
390 Y. Wang, X. Cao, J. Cheng, B. Yao, Y. Zhao, S. Wu, B. Ju, S. Zhang, X. He and W. Niu, *ACS Nano*, 2021, **15**, 3509–3521.
391 J.-W. Oh, W.-J. Chung, K. Heo, H.-E. Jin, B. Y. Lee, E. Wang, C. Zueger, W. Wong, J. Meyer, C. Kim, S.-Y. Lee, W.-G. Kim, M. Zemla, M. Auer, A. Hexemer and S.-W. Lee, *Nat. Commun.*, 2014, **5**, 3043.
392 H. Noh, S. F. Liew, V. Saranathan, S. G. Mochrie, R. O. Prum, E. R. Dufresne and H. Cao, *Adv. Mater.*, 2010, **22**, 2871–2880.
393 P. Vukusic and J. R. Sambles, *Nature*, 2003, **424**, 852–855.
394 A. Belmonte, Y. Y. Ussembayev, T. Bus, I. Nys, K. Neyts and A. P. H. J. Schenning, *Small*, 2020, **16**, 1905219.
395 Y. Y. Diao, X. Y. Liu, G. W. Toh, L. Shi and J. Zi, *Adv. Funct. Mater.*, 2013, **23**, 5373–5380.
396 Z.-H. Zuo, Z.-W. Feng, Y.-Y. Peng, Y. Su, Z.-Q. Liu, G. Li, Y. Yin and Y. Chen, *ACS Nano*, 2024, **18**, 4456–4466.
397 F. Meng, B. Ju, Z. Wang, R. Han, Y. Zhang, S. Zhang, P. Wu and B. Tang, *J. Am. Chem. Soc.*, 2022, **144**, 7610–7615.
398 Z. Li, Q. Fan, Z. Ye, C. Wu, Z. Wang and Y. Yin, *Science*, 2023, **380**, 1384–1390.
399 H. Kim, J. Ge, J. Kim, S.-E. Choi, H. Lee, H. Lee, W. Park, Y. Yin and S. Kwon, *Nat. Photon.*, 2009, **3**, 534–540.
400 Y. Zhao, Z. Xie, H. Gu, C. Zhu and Z. Gu, *Chem. Soc. Rev.*, 2012, **41**, 3297–3317.
401 C. N. Loynachan, A. P. Soleimany, J. S. Dudani, Y. Lin, A. Najer, A. Bekdemir, Q. Chen, S. N. Bhatia and M. M. Stevens, *Nat. Nanotechnol.*, 2019, **14**, 883–890.
402 Y. Ye, Y. Ge, Q. Zhang, M. Yuan, Y. Cai, K. Li, Y. Li, R. Xie, C. Xu and D. Jiang, *Adv. Sci.*, 2022, **9**, 2104738.
403 L. Hao, R. T. Zhao, N. L. Welch, E. K. W. Tan, Q. Zhong, N. S. Harzallah, C. Ngambenjawong, H. Ko, H. E. Fleming and P. C. Sabeti, *Nat. Nanotechnol.*, 2023, 1–10.
404 J. Huang, X. Chen, Y. Jiang, C. Zhang, S. He, H. Wang and K. Pu, *Nat. Mater.*, 2022, **21**, 598–607.
405 L. Yin, M. Cao, K. N. Kim, M. Lin, J.-M. Moon, J. R. Sempionatto, J. Yu, R. Liu, C. Wicker, A. Trifonov, F. Zhang, H. Hu, J. R. Moreto, J. Go, S. Xu and J. Wang, *Nat. Electron.*, 2022, **5**, 694–705.
406 G. A. Kwong, S. Ghosh, L. Gamboa, C. Patriotis, S. Srivastava and S. N. Bhatia, *Nat. Rev. Cancer*, 2021, **21**, 655–668.
407 L. Hao, R. T. Zhao, N. L. Welch, E. K. W. Tan, Q. Zhong, N. S. Harzallah, C. Ngambenjawong, H. Ko, H. E. Fleming, P. C. Sabeti and S. N. Bhatia, *Nat. Nanotechnol.*, 2023, **18**, 798–807.
408 J. Min, S. Demchyshyn, J. R. Sempionatto, Y. Song, B. Hailegnaw, C. Xu, Y. Yang, S. Solomon, C. Putz, L. E. Lehner, J. F. Schwarz, C. Schwarzinger, M. C. Scharber, E. Shirzaei Sani, M. Kaltenbrunner and W. Gao, *Nat. Electron.*, 2023, **6**, 630–641.
409 A. Katoh, K. Maejima, Y. Hiruta and D. Citterio, *Analyst*, 2020, **145**, 6071–6078.
410 B. Khanal, P. Pokhrel, B. Khanal and B. Giri, *ACS Omega*, 2021, **6**, 33837–33845.
411 F. Feng, Z. Ou, F. Zhang, J. Chen, J. Huang, J. Wang, H. Zuo and J. Zeng, *Nano Res.*, 2023, **16**, 12084–12091.
412 T. AbdElFatah, M. Jalali, S. G. Yedire, I. I. Hosseini, C. del Real Mata, H. Khan, S. V. Hamidi, O. Jeanne, R. Siavash Moakhar, M. McLean, D. Patel, Z. Wang, G. McKay, M. Yousefi, D. Nguyen, S. M. Vidal, C. Liang and S. Mahshid, *Nat. Nanotechnol.*, 2023, **18**, 922–932.
413 A. Koh, D. Kang, Y. Xue, S. Lee, R. M. Pielak, J. Kim, T. Hwang, S. Min, A. Banks, P. Bastien, M. C. Manco, L. Wang, K. R. Ammann, K.-I. Jang, P. Won, S. Han, R. Ghaffari, U. Paik, M. J. Slepian, G. Balooch, Y. Huang and J. A. Rogers, *Sci. Transl. Med.*, 2016, **8**, 366ra165.